UNIVERSITÉ CATHOLIQUE DE LOUVAIN
Ecole Polytechnique de Louvain
Institute of Condensed Matter and Nanosciences

Molecular dynamics study of the sputtering of nanostructured metal-organic surfaces

Dissertation présentée en vue de l'obtention du grade de
Docteur en Sciences de l'Ingénieur
par

Oscar Antonio Restrepo Gutiérrez

Membres du jury:

Prof. Arnaud Delcorte, Promoteur
Prof. Sophie Demoustier, Président
Prof. Xavier Gonze , Secrétaire
Prof. Patrick Bertrand
Prof. Zbigniew Postawa
Prof. Annemie Bogaerts

Abstract

Using molecular dynamics simulations, the present research has been focused in the elucidation of the mechanism of sputtering of hybrid metal-organic surfaces. This study takes place in the context of surface analysis by secondary ion mass spectrometry, a method in which kiloelectromvolt (keV) projectiles are used to bombard the samples and the ions emitted by the surface are mass-analyzed. The central question here was to understand the beneficial effect of the presence of gold nanoparticles (NPs) in the organic surfaces for molecular and fragment ion emission enhancement, experimentally observed when atomic projectiles were used, and why a different behavior occurred upon polyatomic projectile bombardment. jIn the process of answering this question, some of the most fundamental aspects involved in the keV bombardment, by monoatomic and polyatomic projectiles (Ga, C_{60}, Au_n and Ar_n), of a polymeric solid covered by gold NPs as well as of the interface between a gold crystal and polymer, have been unveiled. Special attention was given to the influence of the metal in the energy deposition process and in the formation of the sputtered organic species.

The main results of this research, revealed by the variation of the initial conditions and parameters (e.g. impact point, nature and energy of the projectile, atomic mass ratio of the projectile and target), might be that the sputter yield is proportional to the quantity of energy deposited in the extreme surface of the polymer, which depends directly on the stopping power and inversely on the range of the projectile. This is true for both atoms and clusters so that, in some cases, the energy density in the surface is increased by the presence of the Au-NPs (Ga, Au_3, Au_{400} projectiles), while in other cases, it is decreased (C_{60} projectile). Another important result is that, for cluster projectiles in the considered energy range, the sputtering maximizes when the atomic masses of the projectile and target match, i.e. when the energy transfer and angular dispersion in the diatomic collisions are maximum. In addition, the detailed analysis of the simulations provides abundant information concerning, e.g., the projectile implantation, damage produced in the target,

induced pressured waves, crater sizes, and mass, energy and origin of the emitted fragments as a function of the initial conditions, which should be useful for experimentalist. The methodology, results and perspectives of this study, are reported in this manuscript.

Acknowledgements

I want to express my thankfulness to all those persons who directly or in some way help me to finish this doctoral program.

Firstly to my family for their unconditional moral support, without them this project could not be possible. To my mother, brothers and sister, and my wife Natalia, thanks for giving me the strength during those four years in which I could finish this doctoral program.

Also I want to acknowledge to my supervisor Arnaud Delcorte for giving me the opportunity of doing my thesis with him, for his critical and unconditional support during the whole process of this work, for giving me the freedom, but at the same time keeping me in the right way. For him my most sincere gratitude.

I want to give my thanks to all the members of the ancient PCPM; I already miss the fraternal group that I meet four years ago. Thanks to the members of the secretary, in special to Brigitte and Sadia. Also thanks to Alain, Sami, Taoufiq, Guilhem and Claude for their unconditional help.

Thanks to the French community of Belgium for their financial support (ARC NANHYMO: Convention 07/12-003). Thanks to this program my stage in Louvain-la-Neuve has been a pleasant experience.

I would like to thank to all the other members of the jury: Sophie Demoustier, Xavier Gonze, Patrick Bertrand, Zbigniew Postawa, Annemie Bogaerts, for the critical and kindly evaluation of this work.

I express my sincere gratitude to everyone who help me to do possible this project of my life. In special, those who help me with the corrections of this thesis: Guillermo, Aneesh, Bartlomiej, Victor, Loïk, and Sandeep. Also to all the people with whom I have shared all those years at Louvain-la-Neuve.

I finally wish to express my most sincere gratitude to my ancient supervisor Manuel Páez, his help has been a constant during all the process formation of my career as a physicist. Without him this project could be only a utopia.

¡Gracias a todos!

0.1 Acronyms

SIMS Secondary Ion Mass Spectrometry

TOF Time of Flight (Mass Analyzer)

TOF-SIMS Time of Flight Secondary Ion Mass Spectrometry

ME-SIMS Matrix Enhancement Secondary Ion Mass Spectrometry

MetA-SIMS Metal Assisted Secondary Ion Mass Spectrometry

MD Molecular Dynamics

CEM Corrected Effective Medium (theory)

MD/MC-CEM Molecular Dynamics Montecarlo CEM

LJ Lennard Jones (potential)

PE Polyethylene

CG Coarse Grain (approximation)

PES Potential Energy Surface

VdW Van der Waals

UFF Universal Force Field (potential)

EAM Embedded Atom Method (potential)

REBO Reactive Bond Order (potential)

AIREBO Adaptive Intermolecular REBO (potential)

ZBL Ziegler, Biersack and Littmark (repulsive potentials)

NP Nano Particle

SEM Scanning Electron Microscopy

TEM Transmission Electron Microscopy

AFM Atomic Force Microscopy

MALDI Matrix-Assisted Laser Desorption/Ionization

DFT Density Functional Theory

TD-DFT Time Depending Density Functional Theory

Contents

0.1 Acronyms v

1 Introduction **1**
1.1 Fundamentals of SIMS 3
1.2 Importance of SIMS 4
1.3 Where does SIMS need to be improved? 5
1.4 Metal assisted SIMS and Metal-organic surfaces 6

2 Fundamentals **9**
2.1 Collision cascade 9
2.1.1 Binary collision approximation 10
2.1.2 Linear cascades, thermal spikes and chanelling . . 10
2.2 Ranges and stopping power 11
2.2.1 Stopping power 11
2.2.2 Range of monoatomic projectiles 12
2.2.3 Range of cluster projectiles 12
2.3 Sputtering 16
2.4 Overview of molecular dynamics 18
2.4.1 Why molecular dynamics? 18
2.4.2 Equations of motion in MD 21
2.4.3 Integration Methods: Verlet and Gear's predictor-corrector algorithms 22
2.4.4 Langevin dynamics 25
2.4.5 Projectile threshold energies in MD: adiabatic approximation 26
2.5 Potential energy surface (PES) and interatomic forces . . 27
2.5.1 What does interatomic potential means? 27
2.5.2 Classification of potentials 28
2.5.3 Difference between interatomic and intermolecular potentials 28
2.5.4 Simple potentials 28
2.5.5 Sophisticated potentials 31

2.5.6 Repulsive interatomic potentials 35
2.6 The SPUT code 37
2.7 How to handle ionization in simulations 39

3 Metal organic models **41**
3.1 Organic sample model: polyethylene 41
3.1.1 Experimental parameters of the polyethylene . . . 41
3.2 Coarse grain approximation 43
3.2.1 Geometry and physical parameters of PE in the coarse grain approach 44
3.2.2 Advantages and drawbacks of the coarse grain approach 45
3.3 Metal-organic systems 48
3.3.1 Random deposition algorithm 49
3.3.2 Results of the relaxation: NP formation 50
3.3.3 Additional MD studies of the gold deposition over PE 52
3.4 Conclusions 53

4 Monoatomic vs small cluster projectiles **55**
4.1 Study of the gold coated surfaces 55
4.1.1 Details of the simulations 56
4.1.2 Sputtering yields 57
4.1.3 Analysis of the mass spectra 62
4.1.4 Origin of the fragments and emission depth 66
4.1.5 Fragments size: impacts on PE vs impacts on Au-NP 68
4.1.6 Mechanistic analysis of impacts on the Au-NP . . 68
4.1.7 Comparison to results obtained on gold coated amorphous PE 70
4.2 Study of the metal-organic interface 71
4.2.1 Sputtering yield of the metal-organic interface . . . 72
4.2.2 Mechanism of ejection of sample B 74
4.2.3 Additional comparison of the two samples bombarded with Ga and $C_{\mathbf{60}}$ projectiles 76
4.3 Note on the mechanism of crater formation in different materials 77
4.4 Conclusions 80

5 From small to massive cluster projectiles **81**
5.1 Comparison of $C_{\mathbf{60}}$, $Au_{\mathbf{3}}$ and $Au_{\mathbf{400}}$ impacts 81
5.1.1 Analysis of the sputtered mass 82
5.1.2 Microscopic view 84

5.1.3 Comparison with Au_{400} bombardment on gold coated amorphous PE . . . 87
5.2 Influence of the projectile energy upon Au_{400} bombardment 88
5.2.1 Energy dependence of the sputtering . . . 89
5.2.2 Ranges and energy deposition in the surface . . . 92
5.2.3 Cluster-cluster interaction . . . 98
5.3 Argon clusters . . . 101
5.3.1 Emission produced by different argon clusters . . . 102
5.3.2 Low energy impacts with the heavy Ar_{2000} projectile 107
5.4 Conclusions . . . 109

6 Effects of atomic mass in cluster-induced sputtering 111
6.1 Role of the atomic mass in cluster-target collisions . . . 111
6.1.1 Choosing the artificial atomic mass values . . . 112
6.1.2 Changing the atomic mass of the NPs . . . 113
6.1.3 Changing the atomic mass of C_{60} . . . 116
6.2 Conclusions . . . 119

7 Conclusions and perspectives 123

A Relationship between atomic mass and cohesive energy 127

B Some additional comments on sputtering yield and energies 129

List of Figures 133

List of Tables 141

Chapter 1

Introduction

In a world that is moving toward new technologies based on the engineering of matter at the nanometer scale, the development and improvement of existing techniques are of fundamental importance. Among the various existing technologies, the Secondary Ion Mass Spectrometry (SIMS) is a technique for the study and characterization of surfaces. In particular, SIMS uses energetic ions to bombard the surface and collect the "secondary ions" emitted from the surface for the purpose of characterization. One of the main issues existing in this field concerns the case of organic materials, in which the secondary number of ions emitted from the surface is very low, which reduces the efficiency and hence sensitivity of the technique. Recently, hybrid metal-organic nanosystems received much attention after the introduction of Metal-Assisted Secondary Ion Mass Spectrometry (MetA SIMS), in order to improve the efficiency of organic SIMS. In this technique, a thin layer of metal is deposited on the surface of the organic material. In addition, these hybrid metal-organic systems have importance in many areas such as potential barriers in electronic devices, biosensor construction etc. Therefore, this thesis involves the "theoretical study of the sputtering of nanostructured hybrid metal-organic surfaces", using classical molecular dynamics. More specifically, the objectives of this thesis are:

- To unveil what happens in a metal coated system as well as in the interface of a metal-organic bulk sample when they are bombarded by different keV projectiles, monoatomic and polyatomic ones.
- To understand how nanoparticles (NPs) behave under bombardment and how to characterize them.
- To gain more insight in the effects of changing the atomic masses of the NPs as well as of the projectile, and how they affect the

signal and damage in the metal organic surfaces.

The aims of this theoretical study are inspired by several facts:

Firstly, since the discovery of the ultrathin metal coatings, as obtained by sample metallization (MetA-SIMS), it is known that it helps to increase the detected secondary ion yields of organic samples by up to two orders of magnitude when used with monoatomic projectiles. [1, 2, 3, 4] However, it was found that such an enhancement is generally not observed with cluster projectiles, like C_{60} and even Bi_n. Instead, a reduction or a stagnation of the yield, appeared to be the rule upon such cluster bombardment. [5]

Secondly, since the last decade, clusters constitute the projectile of choice for the analysis of organic materials in SIMS. Perhaps with C_{60}, Ar_n, Au_n and Bi_n being some of the most representatives/populars. They have offered a nonlinear increase in the sputtered yield, which have made possible the depth profiling and the 3D analysis of organic molecules. [6] However, a universal projectile that works well for analysis and depth profiling of all organic samples, is still a utopia. For instance, in depth profiling, C_{60} has been proved to fail in the analysis of crosslinked polymers, [7] and organic electronic devices. This is due to the accumulation of the damage caused by C_{60} impacts. This results in the formation of a carbon rich surface, which damps the signal. [8] In contrast, argon clusters are said to be practical in these situations in which C_{60} fails [6], but still, the right size, initial energy ranges, angle of impact, and materials in which they have their maximum performance must be better defined. On the other hand, a Au_{400} cluster ion source was successfully used to produce molecular ions from organic materials, with seemingly excellent surface sensitivity and large molecular ion yields. [9, 10]

Thirdly, nanoparticles (NPs) may be present on a surface either as an impurity, or as intentionally added (salts, metals etc), and they can change the surface properties. When an organic surface has these NPs and it is bombarded by keV projectiles, its fragmentation and posterior desorption does not depend only on the projectile characteristics, but also on the fragmentation and efficient transfer of the energy of the targeted-NPs that are in the projectile trajectory. Direct impacts on NPs may create fragments that can redistribute the energy and produce breaking of bonds in many different ways. In some cases, they can stop the projectiles producing an unwanted effect. [11]

The characterization of these NPs and their environment have gained importance with the advent of nanotechnologies. Nanostructures significantly change the surface properties compared to their flat or bulk coun-

terparts. While their morphology can be studied by various techniques such as SEM, TEM or AFM, their full physical and chemical characterization remains difficult. For instance, recently, SIMS studies in the event-by-event bombardment mode, using Au_{400} as a projectile, have provided morphological and chemical information with a resolution of 10 nm. [12, 13] These measurements also lead to the determination of the surface coverage. For these specific studies, our molecular dynamics (MD) simulations can also provide a more physical background for the interpretation of the experimental results.

1.1 Fundamentals of SIMS

SIMS is a surface sensitive analytical technique which uses ion beams to interrogate the surface. The ion beams are composed either of monoatomic or polyatomic projectiles, which are called "primary projectiles". When the ions impact the surface, a complex process of energy transfer from the projectiles to the atoms or molecules on the target surface starts, eventually it generates a collision cascade. The atoms or molecules will be desorbed from the surface if the recoil energy is sufficient to break the bonds. The ejected atoms or molecules contain ionized as well as neutral species. The ionized species, which are called "secondary ions", are then accelerated and allowed to pass through a mass spectrometer where they are separated according to their mass to charge ratio. These ions are then recorded with a detector to form a mass spectrum.

From this simple, but destructive SIMS technique, chemical and molecular information are obtained. It also offers precise information on the location of the compounds on the sample material, which is used for chemical imaging, bio-imaging, e.g., tissues and single cells. [14] SIMS is a surface analysis technique with trace element sensitivity, capable of sub-micrometer lateral resolution and a depth resolution of $\sim$2 nm. This high resolution is limited first, by the technical problems or capacity to focus the ion source; and second, by the physical limitation of the size of the crater which is related to type of the projectile used. The latter represents the final physical limit on high resolution.

This unique combination of chemical information, lateral resolution, and surface sensitivity, makes SIMS a unique tool with virtually no competition among the others. It can be applied to all kinds of material in the real world, metals, oxides, polymers or complex biomolecules. These are the properties which are the origin of the success of SIMS.

Since its beginnings, SIMS has experienced many successful achievements. First, the introduction of static SIMS allowed the analysis of

complex structures by reducing the current density operation by several orders of magnitude, in contrast to the dynamic SIMS mode in which the samples were destroyed due to the high primary ion current density in a fraction of second. As a consequence any kind of surface analysis became possible. [15] Second, the development of higher mass range analyzers introduced with the time of flight secondary ion mass spectrometry (ToF-SIMS), opened a new field in which for example, oligomer and biomolecular samples could be analyzed, opening the door for a proper characterization of organic materials. Third, in the last decade additional enhancements came with the introduction of the polyatomic projectiles. They allowed for enhanced high-mass ion yields, and low damage cross sections which left the researchers thinking about new applications that may lead to new discoveries in biology and material science. [16]

From the technical point of view there are four different analyses that can be done with SIMS, which are:

1. To obtain *mass spectra*, which provide information about the nature of the sample, i.e., in mass spectra can be observed the chemical and molecular information.

2. *Depth profiling*, which is the study of the distribution of the chemical species or fragments as a function of their depth below surface.

3. *Chemical image* of the surface can be obtained to visualize with high lateral resolution the chemical distribution of the different species or fragments across the surface.

4. *Three dimensional chemical reconstruction* of the sample can also be done by the combination of the information given by depth profiling and chemical imaging.

1.2 Importance of SIMS

Since the pioneering work of Benninghoven in the 60's until now, SIMS has become one the most important techniques for chemical and molecular analysis of complex materials. Nowadays it is not only used for academic purposes, but for example, it has an important role in the semiconductor industry in which it has been used by over three decades. [17, 18, 19] For instance, one of its main industrial applications is in the process control, and nano-technology manufacturing, e.g., to identify and analyze the distribution of the different chemical compounds in the manufacturing process of chips, hard disks, organic electronic and

biosensing devices, compact disk coatings etc. In those cases SIMS helps in the process development, monitoring and troubleshooting. [17]

But it has been in the last ten years that SIMS has become an indispensable tool in the chemical analysis of organic material surfaces. [20, 21] Now, it is used to obtain information of amino acid layers and proteins, frozen cells and tissues. [22] Even more, it is used in the industry of pharmacology and many other areas where chemical and biological identification of complex structures are needed. SIMS as a surface technique for organic compounds goes above all other techniques due to its capacity to identify all elements and isotopes in the periodic table as well as complex molecules. It also gives molecular information of the sample, contrary to other surfaces techniques as for example X-ray photoelectron spectroscopy (XPS) and Auger electron spectroscopy (AES), which are limited to identifying bonding types; or scanning electron microscopy (SEM) and transmission electron microscopy (TEM), which provide morphological information of the surfaces and are not suitable for the analysis of organic or insulator materials.

1.3 Where does SIMS need to be improved?

Among the limitations of SIMS, low ionization is one of the most challenging. Secondary ion formation depends on many different factors, and, the number of sputtered fragments which are ionized remains too small. In most of the cases, the ion yield is barely one percent of the total sputtered material. [16] Even with the introduction of polyatomic ion sources, the relative ionization yields of organic molecules and fragments, that are useful for chemical identification and localization on the surface, remain very low. [11] For instance, recent studies with molecular dynamics simulations and experimental results show that a single C_{60} fullerene projectile can desorb about 10^2 molecules, [11] but, the actually measured ion yield is rather of the order of 10^{-4} to 10^{-2}, which means in the best condition, only one ion is obtained for each 100 impacts. [11] This large gap shows the extent of the signal that might be gained if molecular ionization could be enhanced.

To increase the ionization many approaches have been proposed. For example, by using a more efficient projectile source; by post-ionization, i.e., the neutral species that are emitted after primary bombardment can be post-ionized, for example interacting with a plasma, a laser beam, or an electron beam. Another category of methods is called matrix enhance SIMS (ME-SIMS). It is based on improving the sample preparation protocols by the addition of ionizing compounds with the analyte. ME-SIMS

can be done e.g., by providing the addition of molecules, salts, or even metal NPs to the sample. [1, 11] Those sample preparations can induce ionization enhancement in many different ways: proton transfer, cationization by metal ions, or even lowering of the molecular ionization potential.

1.4 Metal assisted SIMS and Metal-organic surfaces

Among the techniques mentioned in the last paragraph of the previous section, the use of metals to cover the surface offers many advantages. [23, 24] The characterization of the molecular organic materials as well as the improvements of sample image formation can be highly improved by covering the surface with noble metals like gold, silver or platinum, using physical vapor deposition (PVD). Their use can induce first, an improved ionization of the molecules and fragments, which can reach, in quantitative terms, about one order of magnitude for the characteristic fragments and often more for the parent molecules. Second, the organic molecular information is not too much altered. Third, there is production of cationized molecules of the form $(M + Au)^+$ (i.e. a molecule binds with a Au^+ cations), that are useful for identification. Metallization or metal assisted SIMS is conceptually simple and does not require solvents, avoiding the associated issues of sample dissolution, segregation and migration. It makes the technique more universal because it can be applied to any kind of sample surfaces: polymers, biological ones, etc.

Despite the benefits mentioned above, the organic ion yield is still strongly dependent on the projectile used. That fact has been shown by experiments, [5] and explained by computational results (see Chapter 4). For instance, this is the case of C_{60}, with its light atomic mass, which shows poor results when it is used to bombard metal coated surfaces (see Figure 1.1). [25, 26] If the impacts are on gold NPs, the projectile is reflected by the heavy gold, and the energy is not efficiently transferred to the polymer. On the contrary, monoatomic projectiles like Ga or Au fragment the NPs, and produce a large emission yield with the corresponding benefits mentioned above.

In addition to the implementation of MetA-SIMS for the ionization enhancement, metalization of polymers is essential in many other applications such as microelectronic and photonic devices, and medical implants. Some experimental and computational MD results of gold-NP coatings on PE have been found. [27, 28, 29] The techniques for deposition of metals are explained in these references. Finally, among the

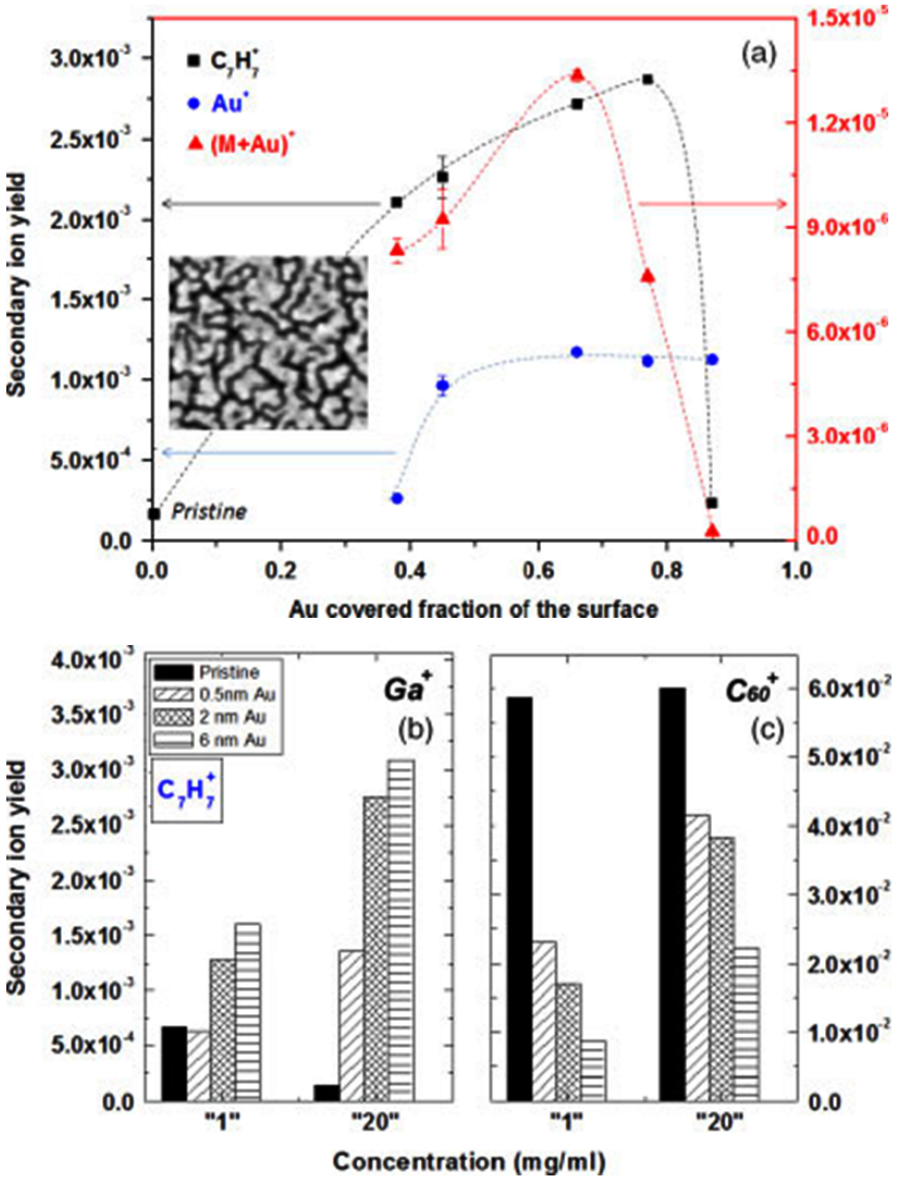

Figure 1.1: (a) Experimental yields of Au^+, $C_7H_7^+$ and Au-cationized PS oligomers measured upon 12 keV Ga^+ bombardment of a thick PS coating, as a function of the fraction of the surface covered by gold. The inset shows the SEM micrograph of the sample surface (200-nm width). (b) and (c) Experimental yields of $C_7H_7^+$ sputtered under 12 keV Ga^+ and C_{60}^+ bombardment of pristine and metal-covered PS coatings (1 and 20 mg/ml PS solution concentrations, and 0.5, 2, 6 nm Au equivalent thicknesses). Figures from ref [25].

known coating methods, vacuum evaporation and sputtering are some of the most important physical ones, while one of chemical techniques is electrodeless plating of polymers in solutions of metallic salts. The metalization, which is affected by the polymer surface topography, can be studied by various techniques e.g. AFM and SEM. [11, 30]

Although a large quantity of work has been done, in the field of MetA-SIMS - and in general of the sputtering process of metal organic systems - a satisfactory model that could help the experimentalists is still needed. In order to tackle this issue, in *chapter* 2 the fundamental theoretical bases are given. Next, in *chapter* 3 the construction of model of metal organic samples is explained, also the coarse grain approach is discussed. It is in *chapter* 4 that a first detailed analysis of the sputtering produced by different projectiles (monoatomic and polyatomic ones) is done. In *chapter* 5, a detailed comparison of the sputtering as a function of the impact energy on the polymer and over the NPs is performed for large and heavy projectiles. The *chapter* 6 discusses the fundamental parameters that are relevant to explain the sputtering mechanisms on metal-coated systems. The general conclusions and perspectives are given at the end of this work, in *chapter* 7.

Chapter 2

Fundamentals

In this chapter the necessary theoretical basis required to achieve the aims proposed in this thesis are laid. The most important theories and definitions of the sputtering process produced by kilo-electron-Volt (keV) projectiles, collision cascades, ranges and stopping power, molecular dynamics, potentials definitions and their respective implementation are given here. This chapter provides the necessary and minimal tools required for the comprehension of the sputtering in both analytical and computational point of views. These items will be discussed one by one in the next sections.

2.1 Collision cascade

When an atom or set of atoms collides with a surface, a series of subsequent collisions nearby impact point start in the solid. Now, depending on whether the energies of the colliding atoms are higher than the displacement energy of the atoms in the solid (which is of the order of 10 eV), a permanent damage can be produced. In this complex process the energetic atoms transfer their energy to their neighbors, and from these to others, creating a series of collisions that will stop when the energy becomes below the displacement energy.

In this context, the sputtering can be considered as a consequence of the collision cascades reaching the surface with enough momentum and energy to permit the atoms (or molecules) to leave the surface.

These collisions in which the momentum and energy of the translational motion is conserved are called “elastic collisions”. On the other hand, those other collisions in which the energy is used to create or destroy bonds (electronic excitations) are called “inelastic collisions”. In the latter situation, there is a strong coupling between the translational

movement of the nuclei and electronic energy transfer, that makes the collision cascade to be neither elastic nor a linear theory. [31] Different approximations can be considered to explain the physics involved in the collision cascades, the classical binary collision approximation, linear cascades, thermal spikes, being some of the most representatives. On the other hand, MD is one method which can be used to understand collision cascades.

2.1.1 Binary collision approximation

In a close collision, it may occur that the ion and a target particle approach each other so closely that the distance of the other target particles is much greater, and their influence can be neglected. In this approach, the collision can be considered only between these two particles and the interatomic force can be considered as entirely repulsive. [32] This is called the binary collision approximation (BCA). The BCA theory consists in considering each collision inside the solid within this approximation. BCA has been successful in describing ranges and implantation at high energies. It is implemented in the popular code SRIM-TRIM. [33] However, since BCA only considers the repulsive part of the interaction potential (which can be represented by a screened Coulombic function, see below the term (2.46)), attractive interactions and chemical reactions cannot be treated.

2.1.2 Linear cascades, thermal spikes and chanelling

A collision cascade can be considered linear as long as in each collision, the primary ion or a primary knock-on particle collides with the particles of target that are at rest. That happens when the density of the target is low and the kinetic energy of the recoil is higher than the cohesive energy of the target, thus in a first approximation, the atoms of the target can be considered as free atoms at rest. [32] This kind of collisions can be treated using the BCA explained above.

On the other hand, “thermal spikes” are defined when the collision cascade happens in dense systems. It is a collision cascade of such high density that every particle in a certain volume is set into motion, therefore, collisions take place with the particles already in motion. [32] In this case, the process becomes a complex process with N-body interactions, which cannot be treated with the BCA theory; however, it can be modeled using classical MD. The heat spike is characterized by the formation of a transient under-dense region in the center of the cascade, and an over-dense region around it. This process is outside of the equilibrium

thermodynamics.

It is also known that the trajectory of a particle through a crystal may be strongly influenced by the crystal structure. In some cases it may happen that the particle may move at small angle to the plane of the crystal having a sequence of weak scattering events and implant deeper. [34] This situation is known as "chanelling". It is unwanted if the desired effect is to give energy into the surface to produce sputtering.

2.2 Ranges and stopping power

When an energetic projectile collides with a surface, it is stopped by the multiple collisions with the atoms of the target. In that process, the slowing down of the projectile is explained first, by the transfer of momentum and energy to the target particles, that is "nuclear stopping", and second, by exciting the electronic system of the target, that is "electronic stopping". The former can be understood as a process in which elastic collisions are dominant and can be studied either by means of MD, or BCA using interatomic repulsive forces. While the latter is a complex inelastic process that requires quantum mechanics. In contrast to nuclear stopping, in the electronic stopping process the kinetic energy is used to modify the atomic internal structure, and electronic excitations are dominant, therefore, the kinetic energy of the particles is not conserved. [35]

Since in the range of keV impact energies the nuclear stopping is the dominant term, [36] the electronic stopping is not considered here.

2.2.1 Stopping power

The *stopping power* can be defined as the average energy loss E of the projectile per unit path length. It represents a quantitative manner to measure the nuclear and electronic stopping, more exactly

$$S(E) = -\frac{dE}{dx} \approx -\frac{\Delta E}{\Delta x} \tag{2.1}$$

where x is the path length. The minus sign makes S positive. One way to calculate the stopping power is to calculate the energy transferred in the collisions. From the classical theory of the elastic collisions it is known that the energy transfer in each collision (and the recoil being at rest before the collision) is given by

$$T = T_{max} \sin^2(\theta/2) \tag{2.2}$$

where θ is the scattering angle measured from the center of mass of the colliding particles with masses m and M. The maximum transfer is

$$T_{max} = E\frac{4Mm}{(m+M)^2}. \tag{2.3}$$

In a binary elastic collision, this energy can be approximated to the energy lost by the projectile, or $T \approx \Delta E$. The interaction potential is introduced through scattering angle θ which depends on the cross section and therefore, of the impact parameter. The total stopping power has linear contributions from the nuclear and electronic parts: $S = Sn + Se$. However, as said above, for impact energies of the order of keV (this is the case of our MD simulations), the collisions can be considered elastic, and hence, only the contribution of the nuclear stopping is considered, or $S \approx Sn$.

On the other hand, the resulting stopping distance measured from the surface determines the projectile *range*, and it is simple to calculate it by using MD or BCA.

2.2.2 Range of monoatomic projectiles

It has been studied both theoretically and experimentally that the range of monoatomic projectiles depends on the projectile-target interaction potential, target cohesive energy, target density, and mass ratio of the projectile-target. [37, 38] An analytical form to calculate the range of a projectile with initial energy E_0 is by using the stopping power definition (2.1) to obtain the mean penetrated *path length* of the projectile, that is

$$R_{ions} \propto \int_{E_0}^{0} \frac{dE}{S(E)}. \tag{2.4}$$

The *penetration depth* is taken as the vertical distance measured from the surface to the end of the projectile's trajectory. Ranges of monoatomic projectiles can be easily calculated using SRIM-TRIM. [33]

2.2.3 Range of cluster projectiles

Ranges of cluster projectiles have been also studied in various targets by mainly using MD. One of the most interesting results comes from the theoretical studies of stopping process of heavy clusters in light or soft materials made by Shulga and Sigmund. [39, 40] They have shown that the range of heavy clusters is increased beyond the range reached by monoatomic projectiles at the same energy per atom and the same atomic mass. To explain this fact, the concept of the "clearing the way" effect

was defined. It says that the front atoms of the cluster transfer enough energy to the target atoms, clearing the way for the following atoms of the cluster. In this manner, the total stopping power of the cluster is reduced. That is clearly observed in Figure 2.1, for Au_{13} and Au_{402} projectiles, where at same energy per atom Au_{402} has larger penetration depth than Au_{13}.

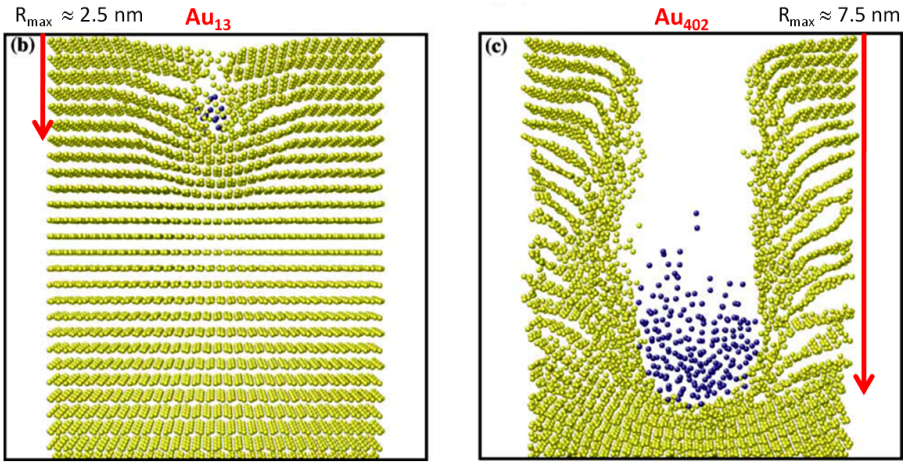

Figure 2.1: Maximum penetration depth R_{max} of Au_{13} and Au_{402} into graphite at same constant energy of 100 eV/atom. The *Clearing the way* effect can be observed. Taken from Ref [41].

In a posterior work made by Carroll *et al.* [42] in which they have computationally investigated the implantation of Ag_n $(n = 20 - 200)$ clusters into graphite substrates, with initial energies ranging from 0.75 to 6 keV, they found that the implantation depth of the center of mass of the cluster could be described by

$$R \propto \frac{E}{n^{2/3}} \qquad \text{or} \qquad R \propto E_0 n^{1/3} \tag{2.5}$$

where $E = nE_0$, and E_0 is the energy per atom. This result clearly shows the global effect of a cluster of atoms when compared individually at the same energy per atom. Additionally, in other posterior works made by Anders and Urbasseck, [41] that study was extended. It was shown that at constant initial energy per atom, ranges follow the power law $R \propto n^{\alpha}$. For that, they used Au_n clusters impinging on graphite at 100 eV per atom. They extended later their work to show the case in which the target cohesive energy U was varied. They found that, first, the range depends on the cohesive energy U as $R \propto U^{-\beta}$, [43] with the exponent depending on the initial energy, and second, for $E_0 > 100$ eV/atom, the range becomes independent of E_0.

Then, from these studies the range of heavy projectiles on soft targets can be expressed by

$$R_{clusters} \propto E_0{}^{\gamma} \frac{n^{\alpha}}{U^{\beta}} \tag{2.6}$$

with α being between 0.3 and 0.4 depending on the target, and β and γ depending on the initial projectile energy, and also depending on the type of range measured, i.e., if it is the range of the center of mass D_{cm} or the maximum range reached by any atom of the projectile D_{max} (see the Figures 2.2a-c). The γ exponent shows a small dependence on cohesive energy, but it strongly depends on the interval of energy chosen.

Not only ranges of heavy projectiles impinging on soft materials have been studied, but also the range behavior of fullerene molecules like C_{60}. [44] In this case the energy dependence of the fullerene range is found to vary as $R \propto E_0^{1/3}$ and $R \propto E^{2/3}$ for impact energies $E < 10$ keV, and $R \propto E$ at higher impact energies, where projectile is fully atomized (here $E = nE_0$). Ranges of C_{60} show a strong dependence on the target material, as it observed in Figure 2.2d. In order to show that,

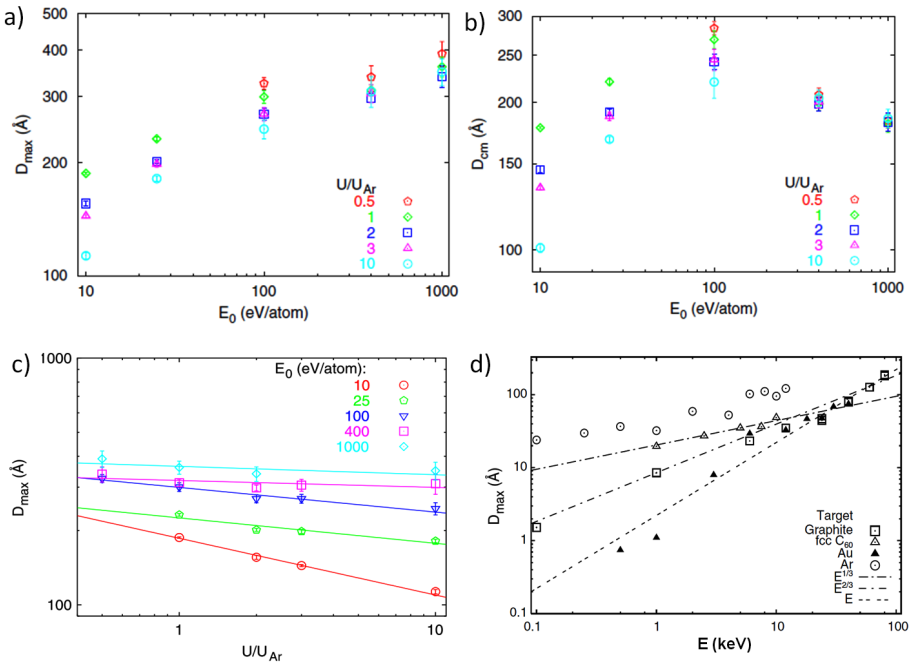

Figure 2.2: Ranges of Au_{402} as a function of impact energy per atom. U/U_{Ar} denotes the cohesive energy divided by the cohesive energy of Ar. In a) maximum range, and in b) range of the center of mass. Bottom: maximum ranges as a function of the cohesive energy of the target in c), and ranges of C_{60} on four different targets d). Taken from refs [42, 41].

four targets were chosen: amorphous Ar, graphite, crystal of fullerite (crystal formed by C_{60}), and Au crystal.

In another article, Seminara *et al*, [45] have shown that there is a linear dependence of the range with the momentum of Ag_n cluster impacts on graphite and at different energies of 1 to 30 keV, or $R \propto E^{1/2}$. Moreover, they proposed that the range can be linearly scaled with the projected momentum, matching in an universal line for all cluster sizes. That is, if the spherical approximation is considered, the volume of the Ag_n cluster can be defined by $n(4/3)\pi r_w^3$, so the cross-sectional area is $\pi n^{2/3} r_w^2$. Then, they have plotted R vs $p/(n^{2/3} r_w^2)$, where p is the momentum of an n-atom cluster, and r_w is the Wigner-Seitz or Voronoi radius of Ag. In other words, they have divided the cluster momentum by the projected surface area of the cluster on the surface. Additionally, in a recent article, this universal behavior is tested again by Popok *et al.* [46] To do that, graphite was rather impacted by clusters of Cobalt Co_n, with an energy up to 200 eV/atom and the results were compared to experimental data with good agreement (see in Figure 2.3).

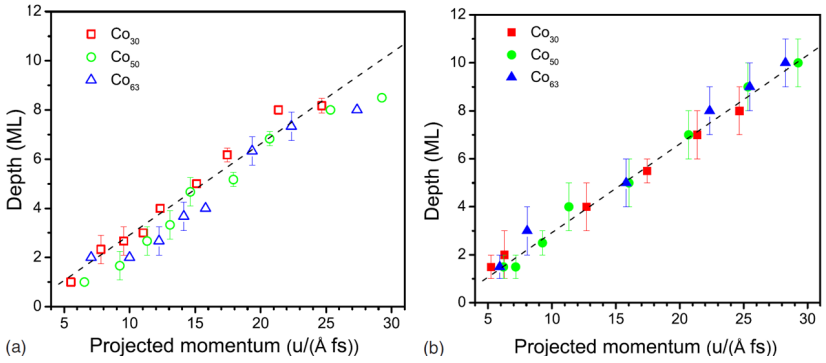

Figure 2.3: In a) MD simulations of the deepest implanted Co atoms vs projected momentum for different clusters sizes, and b) comparison to the corresponding experimental data. Taken from Ref [46].

Finally, in contrast to soft materials such as graphite, a comparison of impacts on carbon diamond structure by a energetic Ar_{961} cluster and a hard sphere at an energy of 100 keV is shown in Figure 2.4. [47] The hard sphere was created with the same density as the cluster of Argon, supposing that the atoms were uniformly distributed into the sphere, and with the same mass of the cluster to guaranty the same momentum. The results show the role of the projectile cohesive energy in the limit that it is infinite (hard sphere). Therefore, the projectile energy is not spent in the internal degrees of freedom of the projectile, and the projectile can go further into the material. Clearly, as the projectile cohesive energy

increases, the range increases.

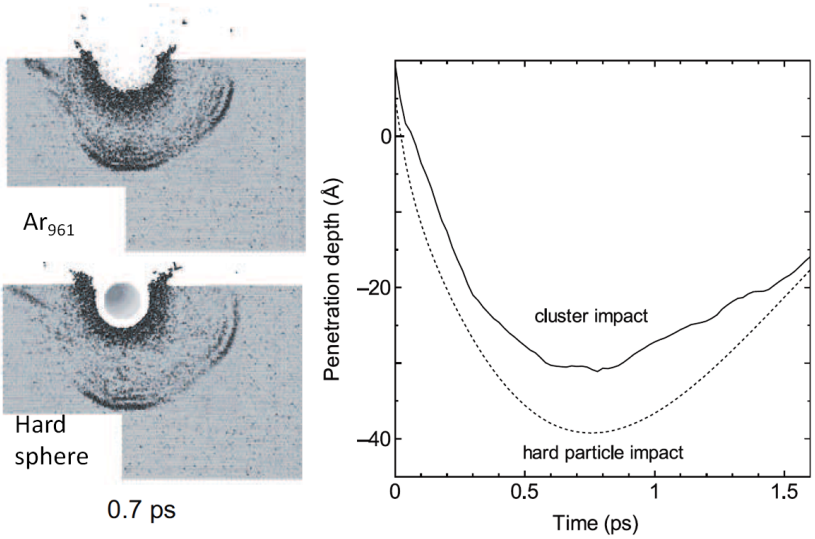

Figure 2.4: Comparison of Ar_{961} cluster impacts with a hard particle impact on carbon diamond structure at an energy E of 100 keV (10 Å cross-section). Taken from Ref [47].

2.3 Sputtering

The sputtering is a process whereby atoms are ejected from a solid target material due to bombardment by energetic particles. The ejected fragments or molecules constitute the sputtering yield (or sputter yield) Y, which is defined by

$$Y = \frac{\text{Number of particles removed}}{\text{Number of incident particles}}. \tag{2.7}$$

This sputtering yield is formed by positive, negative and neutral species. The sputtering yield occurs after certain threshold projectile energy and initially it is an increasing function, which reaches a maximum and then decreases as the energy increases. Both, the threshold and the maximum sputtering will depend on the nature of the projectile and target. [16] Beyond this energy, the yield drops as a consequence of the deeper projectile implantation into the surface. It also depends on other parameters such as the angle of incidence of the primary projectile, mass of the projectile, sublimation and binding energy of the target, etc. In addition to SIMS applications, the sputtering is commonly used

in other areas such as thin-film deposition, etching and other analytical techniques.

A number of approximations has been implemented to predict the sputter yield with monoatomic projectiles, [16, 48] the Sigmund theory being one of the most well-known. [49, 50, 51, 52] From Sigmund theory sputter yield can be calculated quantitatively. In the case of linear cascades, sputtering can be described by linearized equations of the Boltzmann type. In this approximation the sputter yield of a simple target is represented by [48]

$$Y = \Lambda F_D, \tag{2.8}$$

with

$$F_D = \left(\frac{dE}{dx}\right)_n \alpha\left(\frac{M_1}{M_2}, \theta_0, E_0\right), \tag{2.9}$$

and

$$\Lambda = \frac{\Gamma_m}{8(1-2m)} \frac{1}{NC_m U^{1-2m}}. \tag{2.10}$$

F_D is the energy deposited per unit depth at the sputtered surface. In (2.9), the first term is the elastic stopping power, and α is a dimensionless function of the target/ion mass ratio M_1/M_2, the incidence angle θ_0 and the projectile energy E_0. In (2.10), Λ is a material constant containing the planar surface potential U, the number density N, cross section parameters m and C_m and a dimensionless quantity Γ_m dependent on m.

Despite the success of the linear theory, experimentally it was found that these expressions underestimate the sputter yield in the case of very heavy ion bombardment of heavy target materials. In addition, they cannot describe well the yield produced by cluster projectiles in the dense cascades in the spike regimes (high density). The calculation of the sputter yield produced by high energy impacts in linear cascades (low density) is implemented in the program TRIM. [33]

On the other hand, in the case of polyatomic as well as monoatomic projectiles interacting with complex targets, MD simulations has been considered as the most important method to understand the sputtering process. In the area of SIMS, some of the most important results in the last decade, obtained using MD, can be found in the review article [53]. For instance, in Figure 2.5 is shown the yield produced by Ga and C_{60} bombardment of three layers of benzene on Ag crystal using MD simulations. 15 impacts were done in each case.

The total sputter yield can be quantified in MD by calculating the total ejected mass, or volume. In the case of molecules, it is also important to calculate the total number of ejected molecules as well as the

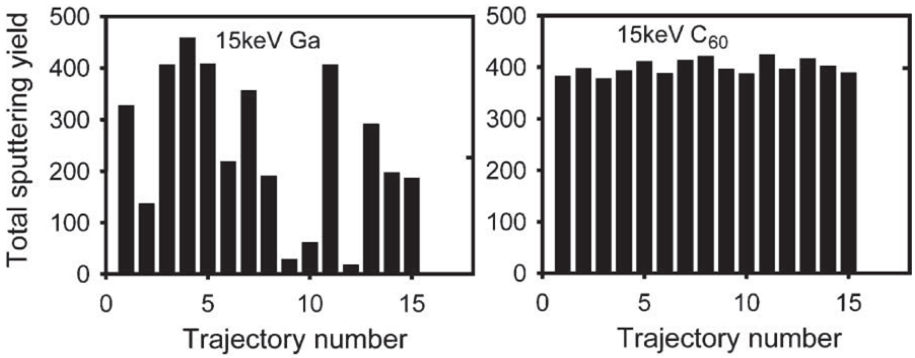

Figure 2.5: Sputtering yield in benzene molecule equivalents vs individual aiming points for 15 keV Ga and C_{60} bombardment. From Ref [53].

number of ejected fragments. A discussion of the implementation of this in MD, is given in Ref [54].

Finally, not only emission of fragments, but also electron emission is observed. Some of the most interesting results in this subfield are presented by Duvenbeck in his doctoral thesis. [55] In Figure 2.6 is shown a MD simulation and experimental comparison of the electron emission. It was theoretically computed in the framework of the Lindhard theory, solving numerically the Boltzmann equation and by using MD to calculate the positions of the atoms. Additional discussion of this model will be given in section 2.7 for the ionization case.

2.4 Overview of molecular dynamics

MD has been considered as one the most powerful theoretical and computational techniques for the understanding of sputtering process, and the predominant method to use. Therefore, it constitutes the fundamental method underlying the work done through this thesis. So, in this chapter, a summarized explanation of the method, how to apply it, its advantages and limitations are given, all in the context of the applications of SIMS and sputtering dynamics process.

2.4.1 Why molecular dynamics?

MD simulations of monatomic and cluster projectiles interactions with surfaces can provide valuable understanding into the complex processes which can occur and are responsible for the wanted and unwanted effects in surface analysis by ion beams and SIMS applications. For instance, MD simulations have shown how cluster impacts can cause

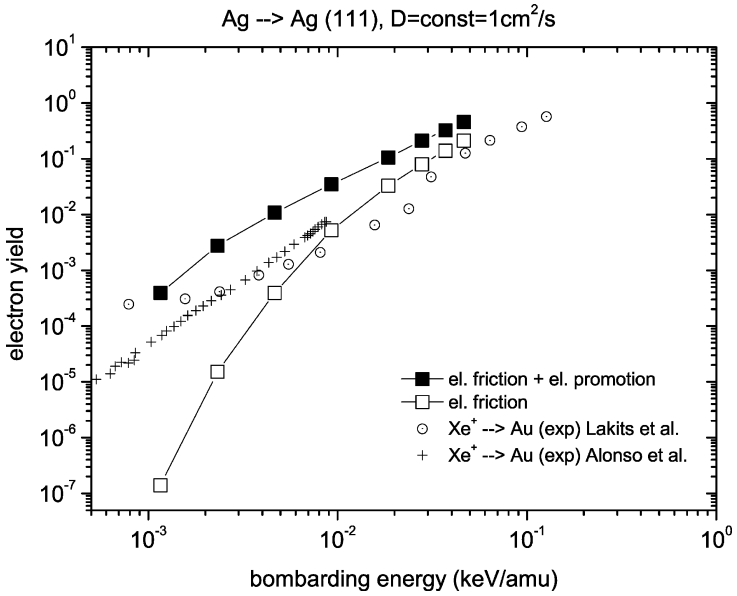

Figure 2.6: Average kinetic electron emission yield as a function of projectile energy for $Ag \rightarrow Ag$ bombardment; model calculations employing both excitation mechanisms (electronic friction + electron promotion, -■-) are compared with the corresponding model calculations that disregard electron promotion processes (-□-); the symbols correspond to experimental data (Lakits *et al.* (⊙), Alonso *et al.* (+)) for $Xe^{+} \rightarrow Au$ bombardment. Figure from Ref [56].

motion and crater formation in the target material, which can result in the gentle desorption of large intact molecules adsorbed on the surface, in contrast to the behavior of single atom impacts, which tend to create discrete motion in the surface often ejecting fragments of adsorbed molecules instead. [57] They can provide useful information on the changes in the target, total sputtering, fragmentation of molecules, etc, which is hard to obtain from experimental measurements alone. As exposed by Roger Webb in the reference [57], with MD simulations it can be verified whether the theoretical assumptions are sufficient to explain the experimental observations. Moreover, with MD it is possible to demonstrate which are the important theoretical assumptions and whether it is possible to remove or change physical assumptions, which is easy to do in simulations, in contrast with the "*real world*". From the insight provided by MD simulations, experimentalists can improve their equipment for new experiments to maximize the desired effects.

But, what is MD? In essence, it is a method in which the initial conditions of the system of study must be given, and by numerical integration of the Newton equations, one can obtain the future evolution of

the system under investigation (at least for some portion of time).

If we start with the assumption that the implemented potentials describe the system properties accurately, then, MD becomes a method capable of treating the many body problem, and its solution constitutes a first approximation to the physics involved in such a complex many body problem. Furthermore, the time involved in the sputtering process is in the range of time that can be treatable by MD. Therefore, it allows following the time evolution of the system, and it is in this fact that the power of MD resides. It allows us to compute information that can be directly compared with experiments, and in this manner reduce experimental cost, by giving directions for new and more asserted experiments. With MD we can calculate: [58]

1. The total sputtered yield, one of the most important quantities, but also, one of the most computationally expensive, not only because it is obtained at the end of the simulation but, because sometimes it involves statistics which can only be obtained by doing a large number of simulations.

2. Mass spectra can be created and compared to experiments, for a better understanding of the molecular fragmentation of the target as a function of external parameters such as the projectile type or initial energy.

3. Crater formation and its morphology after bombardment.

4. Rearrangement of organic molecules and reaction between different molecules.

5. The chemistry of the beam induced cross-linking, if the right potentials are implemented (for example AIREBO).

6. Kinetic as well as angular distributions of the considered fragments can be calculated.

7. Ranges, maximum depth of any atom and maximum depth reached by the center of mass of the projectile are easily obtained in the firsts pico-seconds of integration. Shock-waves produced by the impacts can be visualized in the movies created by MD.

8. It is possible to study equilibrium as well as non-equilibrium thermodynamics properties of the systems.

9. With the new visualization technologies, which permit the manipulation of millions of atom positions it is very easy to see with good

rendering the origin and volume of the desorbed yield as well as other quantities.

However many other important factors for SIMS, are for the moment, out of the scope of MD, ionization being one of the most important ones. Ionization means the introduction of electronic properties, and that means to increase the number of degrees of freedom of the system. The problem becomes complicated and, for huge systems, intractable. MD is in essence a classical theory and the potentials implemented in it are obtained from empirical calculations, in which only geometrical and other parameters that left outside the electronic part, are used.

Even with the classical approximation the system size and therefore the computational time to achieve one simulation can be problematic. Currently MD simulations can be performed on large organic materials employing sophisticated many body potentials for times of many picoseconds and millions of atoms. However, even with the computational resources given nowadays, the MD simulations for large systems for long times are very time consuming (sometimes several months or years). There is approximately a scaling factor of 10^{17} in the time scales between the "*real world*" and the "*wall time*" of large-scale atomistic MD simulations. [57] Nevertheless, MD is still the best theoretical tool to handle the chaotic dynamic of molecular systems during the process of the sputtering.

2.4.2 Equations of motion in MD

Consider a system with N degrees of freedom and represented by a set of variables or generalized coordinates $P : \{p_1, p_2, ..., p_N\}$ and $Q : \{q_1, q_2..., q_N\}$ respectively. The classical evolution of the system can be predicted by the Hamiltonian equations

$$-\dot{p}_i = \frac{\partial \mathcal{H}}{\partial q_i}, \qquad \dot{q}_i = \frac{\partial \mathcal{H}}{\partial p_i}, \tag{2.11}$$

where $\mathcal{H} \equiv \mathcal{H}(P, Q)$ represents the Hamiltonian of the system, which is given by

$$\mathcal{H}(Q, P) = \sum_{i=1}^{N} \frac{\mathbf{p}_i^2}{2m} + \mathcal{V}(Q) \tag{2.12}$$

Now, for a system in Cartesian coordinates, the Hamilton equations are reduced to the Newton ones, in which the forces are obtained from the gradient of the potential function $\mathcal{V}$, or

$$m\mathbf{a}_i = \mathbf{F}_i = -\nabla_i \mathcal{V}(\mathbf{r}_1, \mathbf{r}_2..., \mathbf{r}_N) \tag{2.13}$$

The only requirement to integrate the N equations is to have the initial two conditions $(\mathbf{r}_i(0), \mathbf{p}_i(0))$ for each one of them, i.e. to know the initial values of the positions and velocities. However, the system is governed by a set of N coupled ordinary differential equations which do not have analytical solution. The only form to solve them is by using finite difference methods. The general idea is, if it is given the positions and velocities as well as other dynamic information (to calculate the forces) at one time t, to obtain the positions, velocities, forces and other parameters at a later time $t + \Delta t$. This procedure is iteratively repeated until some condition is met. In the case of sputtering, the numerical integration is usually finished when no more particles can be ejected from the surface. Operationally, the integration terminates either when the most energetic particle in the solid has less than some threshold value of energy, or when the number of ejected particles remains constant. Additionally, the integration can be terminated when a certain number of steps is reached.

2.4.3 Integration Methods: Verlet and Gear's predictor-corrector algorithms

In this part, we deal with the techniques to integrate the equations of motion for a system of N particles. Among the variety of integration methods, two are explored here: Verlet and fifth-order Gear's Predictor-Corrector. The former for simplicity and understanding, and the latter because it is the one implemented to do the calculations. The Verlet algorithm became popular after the publication of the French physicist Loup Verlet in 1967. [59] In his work he considered a simple two-body Lennard-Jones type potential

$$V_{LJ}(r) = 4\epsilon \left[\left(\frac{\sigma}{r}\right)^{12} - \left(\frac{\sigma}{r}\right)^{6} \right] \tag{2.14}$$

with a cutoff distance of $r_c = 2.5\sigma$ and σ being the distance at which the potential is zero. The problem is to integrate the Newton equation (2.13) for the particle i, that in its differential form is written as

$$m\frac{d^2\mathbf{r}_i}{dt^2} = \sum_{i=1, i\neq j}^{N} \mathbf{F}_i(\mathbf{r}_{ij}) \tag{2.15}$$

Thus, the force acting on the particle i in the direction x is given by the expression

$$F_x(\mathbf{r}_{ij}) = \frac{48\epsilon}{\sigma^2}(x_i - x_j) \left[\left(\frac{\sigma}{r_{ij}}\right)^{14} - \frac{1}{2}\left(\frac{\sigma}{r_{ij}}\right)^{8} \right] \tag{2.16}$$

The Verlet algorithm consists in integrating the equation (2.15) with the simple form

$$\mathbf{r}_i(t+\Delta t) = -\mathbf{r}_i(t-\Delta t) + 2\mathbf{r}_i(t) + \frac{\Delta t^2}{m}\sum_{i=1,i\neq j}^{N}\mathbf{F}_i(\mathbf{r}_{ij}) \tag{2.17}$$

the velocities can be calculated using the Taylor expansion around $t+\Delta t$ and $t-\Delta t$ and to take the difference,

$$\mathbf{r_i}(t+\Delta t) = \mathbf{r_i}(t) + \mathbf{v_i}(t)\Delta t + \frac{1}{2}\mathbf{a_i}(t)\Delta t^2 + \frac{1}{6}\mathbf{b_i}(t)\Delta t^3 + O(\Delta t^4)$$

$$\mathbf{r_i}(t-\Delta t) = \mathbf{r_i}(t) - \mathbf{v_i}(t)\Delta t + \frac{1}{2}\mathbf{a_i}(t)\Delta t^2 - \frac{1}{6}\mathbf{b_i}(t)\Delta t^3 + O(\Delta t^4)$$

which conducts to the simple expression

$$\mathbf{v}_i(t) = \frac{\mathbf{r}_i(t+\Delta t) - \mathbf{r}_i(t-\Delta t)}{2\Delta t} \tag{2.18}$$

Something important to realize is that the local error in the integration for the position is of the order of Δt^4, while in the velocities is of the order of Δt^2. That means that global error will be dominated by the biggest one, i.e., Δt^2, and the Verlet integrator is therefore known as a second-order integrator. Additionally, due to the fact that it is properly centered, i.e., $\mathbf{r}_i(t+\Delta t)$ and $\mathbf{r}_i(t-\Delta t)$ are present, the system is time-reversible. This algorithm also conserves the linear momentum and energy properties for long time steps.

On the order hand, differently to Verlet where only the position $\mathbf{r}$ and velocity $\mathbf{v}$ are needed, the Fifth-order Gear's Predictor-Corrector requires to know more information about the system from the higher derivatives. It consists of three steps, predictor, force correction and corrector. The first step is, by means of a Taylor expansion from the positions and their time derivatives up to the 5^{th} order, all known at time t, to "predict" the same quantities at time $t+\Delta t$

$$\begin{aligned}
\mathbf{r_i}^p(t+\Delta t) &= \mathbf{r_i}(t) + \mathbf{v_i}(t)\Delta t + \frac{1}{2}\mathbf{a_i}(t)\Delta t^2 + \frac{1}{6}\mathbf{b_i}(t)\Delta t^3 + \frac{1}{24}\mathbf{c_i}(t)\Delta t^4 \\
\mathbf{v_i}^p(t+\Delta t) &= \mathbf{v_i}(t) + \mathbf{a_i}(t)\Delta t + \frac{1}{2}\mathbf{b_i}(t)\Delta t^2 + \frac{1}{6}\mathbf{c_i}(t)\Delta t^3 + ... \\
\mathbf{a_i}^p(t+\Delta t) &= \mathbf{a_i}(t) + \mathbf{b_i}(t)\Delta t + \frac{1}{2}\mathbf{c_i}(t)\Delta t^2 + ... \\
\mathbf{b_i}^p(t+\Delta t) &= \mathbf{b_i}(t) + \mathbf{c_i}(t)\Delta t + ... \\
\mathbf{c_i}^p(t+\Delta t) &= \mathbf{c_i}(t) + ...
\end{aligned} \tag{2.19}$$

The superscript p represents the predicted values. In a second step, with the last predicted positions, the force is computed taking the gradient of the potential and hence accelerations $\mathbf{a^c}_i = \mathbf{F}_i/m$. However, the resulting acceleration is in general different from the "predicted acceleration". The difference between the two can be considered as an "error signal". More precisely

$$\Delta\mathbf{a_i}(t+\Delta t) = \mathbf{a_i}^c(t+\Delta t) - \mathbf{a_i}^p(t+\Delta t) \tag{2.20}$$

In the third step, with this error signal, we "correct" positions and their derivatives. Each correction is proportional to the error signal, with the coefficient of proportionality being a "magic number" which can be determined to maximize the stability of the algorithm

$$\begin{aligned}
\mathbf{r_i}^c(t+\Delta t) &= \mathbf{r_i}^p(t+\Delta t) + C_0\Delta\mathbf{a_i}(t+\Delta t) \\
\mathbf{v_i}^c(t+\Delta t) &= \mathbf{v_i}^p(t+\Delta t) + C_1\Delta\mathbf{a_i}(t+\Delta t) \\
\mathbf{a_i}^c(t+\Delta t) &= \mathbf{a_i}^p(t+\Delta t) + C_2\Delta\mathbf{a_i}(t+\Delta t) \\
\mathbf{b_i}^c(t+\Delta t) &= \mathbf{b_i}^p(t+\Delta t) + C_3\Delta\mathbf{a_i}(t+\Delta t) \\
\mathbf{c_i}^c(t+\Delta t) &= \mathbf{c_i}^p(t+\Delta t) + C_4\Delta\mathbf{a_i}(t+\Delta t)
\end{aligned} \tag{2.21}$$

The coefficients values $(C_0, C_1, C_2, C_3, C_4)$ will depend on the differential equation to solve. For the case of second-order of the form $\ddot{\mathbf{r}} = f(\mathbf{r})$ they are $(19/120, 3/4, 1, 1/2, 1/12)/2$, and for a second-order of the form $\ddot{\mathbf{r}} = f(\mathbf{r}, \dot{\mathbf{r}})$ in which the first derivatives appear, C_0 should be replaced by $19/90$.

This algorithm, in contrast to the Verlet, keeps the energy fluctuations small, which makes it superior. However, it has problems with the total energy conservation for large time steps, that is, if Δt is too large, the energy diverges from the real value. In addition, Gear's method requires $15N$ words of storage ($\mathbf{r}, \mathbf{v}, \mathbf{a}, \mathbf{b}$ and $\mathbf{c}$), in contrast to Verlet that only requires $9N$ (only $\mathbf{r}, \mathbf{v}, \mathbf{a}$ are needed).

When the code is initialized or restarted after some time, the positions, velocities and forces are taken from the initial input parameters or from the last ones saved in the backup file, respectively. In both cases the high orders derivatives $\mathbf{b}$ and $\mathbf{c}$ are set to zero. Although it is supposed that the values will rapidly converge to the real ones, this fact may introduce some error when the system is restarted, as it can be tested by running the same job two times and one of them stopped and restarted. The sputtered fragments which are calculated at the end of the simulation are particularly sensitive to this fact, and to the truncation error introduced when the code is stopped.

2.4.4 Langevin dynamics

When stochastic forces are needed, for example, to relax the system at some temperature T, or to dissipate some undesired forms of energy as for example energy reflection at the borders, the Langevin equations constitute an appropriated method to do it. The use of stochastic MD also allows us to reduce the number of atoms via replacement of the weakly interacting ones by a suitably chosen heat bath. [60, 61, 62, 63] Differently to the Newton equations (2.13), the Langevin dynamics includes two additional forces, a frictional (local and isotropic) one that is proportional to the velocities, and another one which is of stochastic nature. The Langevin equations are

$$m\mathbf{a}_i = -\nabla_i \mathcal{V}(\mathbf{r}_1, \mathbf{r}_2 ..., \mathbf{r}_N) - m\gamma \mathbf{v}_i + \mathbf{f}_i^R(t) \tag{2.22}$$

$$\gamma = \frac{1}{6}\pi\omega_D \tag{2.23}$$

$$\mathbf{f}_i^R(t) = \sqrt{\left(\frac{2\gamma k_B T m}{\Delta t}\right)}\boldsymbol{\xi}_i. \tag{2.24}$$

In (2.22), the first term is the force calculated through the potential, the second term is the frictional force, with a viscosity coefficient given by γ and which depends on ω_D, the Debye frequency (ω_D ensures that the long-time energy transfer into the bulk system is given correctly). The last term represents the Gaussian white force depending on the temperature, with $\boldsymbol{\xi}_i$ being a vector calculated by Gaussian random numbers. This Gaussian force ensures that the frictional and random forces obey the fluctuation-dissipation theorem, which says that

$$\left\langle \mathbf{f}_i^R(t)\mathbf{f}_i^R(0)\right\rangle = \delta(t)2\gamma m k_B T \tag{2.25}$$

whith k_B being the Boltzmann's constant.

In the code, the implementation of stochastic atoms can be done either by choosing the desired atoms, or choosing a spatial region which is normally defined with respect to a certain distance from the boundaries (the impact region is excluded). For those atoms subject to stochastic forces in that region, a lower integrator method is used, and the corrector coefficients $(C_0, C_1, C_2, C_3, C_4)$ are set to $(0, 1, 1, 0, 0)/2$. Rigid atoms are also implemented, and it is not allowed moving them during the integration. In the case of rigid atoms all coefficients are set to zero. These atoms (stochastic and rigid) can be considered as the "edge atoms", and they are responsible for removing the excess of energy in the borders.

It is important to point out that while the stochastic force (2.24) is used to keep the system at some temperature during the relaxation, in

most bombardment simulations, the temperature is set to zero. Thus, only the frictional force is kept for the edge atoms. The role of the frictional force is to damp the edge atoms, for example when they receive additional energy from the pressure wave produce by the impact. In this manner the excess of energy is removed. This artificial method allows us to reduce the number of atoms needed to simulate the damage produced by the impact, and to avoid the reflection of energy caused by the small size of the system. For the frictional force, finding the right artificial Debye frequency that works well can be a challenge.

When the code is initialized the positions are taken from the desired structure, and velocities can be either set to zero, which is usually the case for bombardment, or set to some values according to the Maxwell distribution. This last case is often implemented when we want to relax the system at some temperature rather than to bombard it; it allows us to reduce the computational time.

2.4.5 Projectile threshold energies in MD: adiabatic approximation

The adiabatic (or Born-Oppenheimer) approximation is based on the fact that the velocities of the nuclei (of the order of 10^5 cm/s) are lower than electronic velocities (of the order of 10^8 cm/s, in the Fermi surface). [64, 65] Because nuclei move slowly in the scale of electronic velocities, at any moment the electrons can be considered to be in their ground state. We can use the electronic velocities to find the threshold energies in which the adiabatic approximation is not longer valid; i.e, the energies at which the projectiles will move at the same velocity of the electrons. They can be calculated by using the simple definition of the kinetic energy. Threshold energies are given in the Table 2.1 for some atoms.

Atom	E_0 (keV/atom)
Ga	360
C	60
Au	1020
Ar	207
H	5

Table 2.1: Threshold energies above which the adiabatic approximation is no longer valid. They are calculated by using the simple kinetic energy definition $E_0 = 1/2mv^2$, where m is the mass of the projectile, and $v = 10^8$ m/s.

For keV bombardment in MD, these limits must be taken in account

when the projectile energies are chosen. When these limits are overcome electronic effects become important and collisions cannot be longer considered as elastic. Once this threshold is overcome the electronic stopping power becomes dominant.

2.5 Potential energy surface (PES) and interatomic forces

The heart of the MD resides in the interatomic potentials used to describe the forces that act between the particles. If a correct description of forces is given, the system will be in better agreement with the reality. Their choice and implementation must be careful, in order to fulfill the approximations and level of precision needed to describe the system under investigation. It is also well known that the major part of the computational time is used in the calculation of forces, which can be more than eighty percent with a simple LJ. Although some potentials may better describe the system under consideration, they could be very computationally expensive. Therefore, the computational time and size of the sample are important at the moment of choosing the right potentials.

So, how can the potentials be chosen? The procedure used to obtain empirical PES is often the same: a convenient functional mathematical form is chosen with some adjustable parameters, which are fitted to some combination of calculated and experimental data. The main problem is that the simplest form rarely describes well all the properties of the system. Then, which functional form should be used? This question is answered in the next subsections.

It is important to point out that the objective in this thesis is not to develop the potentials, we only use them. Nevertheless, a clear understanding of their, capacity, flexibility, accuracy, transferability, computational efficiency and range of validity is required if a good description of the system is desired.

2.5.1 What does interatomic potential means?

Within the Born-Oppenheimer approximation (or adiabatic approximation), [64, 65] we can say that an interatomic potential is the solution of the electronic part of the Schrödinger equation. [58] In that framework nuclei move so slowly, that electrons are always in their ground state. All electronic degrees of freedom and, hence, the electronic effects are implicitly incorporated into the potential, and this potential only depends

on the nuclei positions that are supposed to move classically.

2.5.2 Classification of potentials

There are many different ways to classify interatomic potentials, the most common is as a short or long range interaction potentials. They can also be categorized based on the bonding chemistry, i.e., Van der Waals (VdW) interactions, covalent bonding, ionic bonding, metallic bonding and hybrid bonding. They can also be classified according to the type of material, e.g., silicon, carbon, silica etc. Furthermore, the potentials can be given in form of a look-up table obtained, for example, from DFT, Hartree Fock numerical calculations, etc, or given by analytical formulas such as pair potentials or sophisticated functional forms. Therefore, the correct choice for one specific simulation, will depend on the final goals.

2.5.3 Difference between interatomic and intermolecular potentials

When the considered system is composed by many molecules the treatment of the forces becomes complex. The potential energy $\mathcal{V}_{Mol}$ for an arbitrary geometry of a molecule, can be expressed as a superposition of valence (or bonded) interactions $\mathcal{V}_b$, which are composed of specific connections defined by the internal structure of the molecule, and non-bonded interactions $\mathcal{V}_{nb}$, which only depend on the interatomic distances, and irrespective of the fact that they belong to the same molecule or not, that is

$$\mathcal{V}_{Mol} = \mathcal{V}_b + \mathcal{V}_{nb}. \tag{2.26}$$

Bonding interactions are of the order of eV, and can be treated in a simple or sophisticated manner by using, for example, either a simple Morse potential, or more sophisticated Tersoff potential. On the other hand, nonbonded interactions in neutral molecules are purely VdW, and are of the order of the meV. Now, if two interacting molecules are with an excess of charge, an electrostatic interaction must be added to $\mathcal{V}_{nb}$, and the intermolecular strength will depend on the excess of charge.

2.5.4 Simple potentials

Consider any pair of neutral atoms (or molecules) with some separation between their cores. Although the net charge in the atoms is zero, due to the small separation between the charges and their distribution, a small attractive potential appears between them. This interaction is called dipole-dipole or Van der Walls (VdW) interaction, and it is simple

to show that evolves as Ar^{-6}. [64] Now, as the atoms become close, the electronic levels start to overlap and nuclei start to interact, normally, this interaction is of the form $exp(-\beta r)$. Those two terms represent well the interaction for some simple systems. The LJ potential (2.14) is defined as the sum of these two terms; however, for historical reasons and computational ease, the nuclear term is replaced by a term of the form Br^{-12}. The constants A and B are related to the LJ form 12-6 potential (2.14) by $A = 4\epsilon\sigma^{12}$ and $B = 4\epsilon\sigma^{6}$. The LJ representation used in the SPUT code is written in the less conventional form (see also Figure 2.7)

$$V_{LJ}(r) = \epsilon \left[\left(\frac{r_e}{r} \right)^{12} - 2 \left(\frac{r_e}{r} \right)^{6} \right] \tag{2.27}$$

where r_e is the equilibrium distance and is related to σ by the expression $r_e = 2^{1/6}\sigma$. Then, the total potential energy of the particles can be given

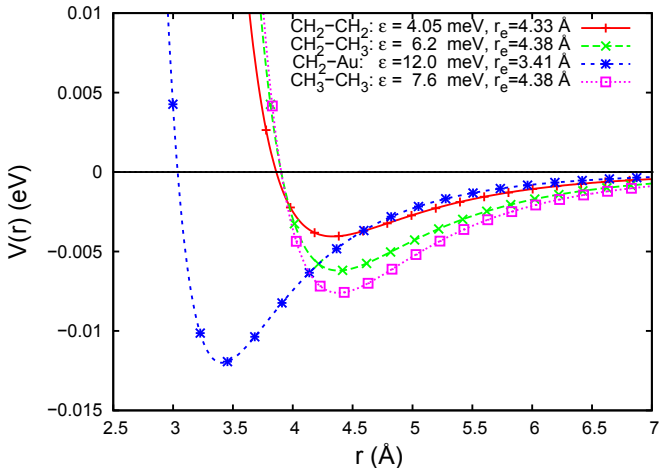

Figure 2.7: Example of LJ potentials for four different interactions as they are described by the Equation (2.27). The parameters will be used later in Chapter 3 for polyethylene and gold interactions.

by the pair potential, which is written as a sum over all pairs

$$\mathcal{V}(\mathcal{R}) \equiv \mathcal{V}(\mathbf{r}_1, \mathbf{r}_2 ..., \mathbf{r}_N) = \sum_{i<j} V_{LJ}(r_{ij}). \tag{2.28}$$

This potential is simple (it is only needed to know two external parameters: ϵ and r_e) and represents well atoms and particles which do not have an excess of charge. It works particularly well for systems where the valence shell is fully occupied, as for example Ar, Ne. For different

atom types, the general values ϵ_{AB} and σ_{AB} can be obtained from the homonuclear parameters using the simple rule

$$\begin{aligned} \epsilon_{AB} &= \sqrt{\epsilon_A \epsilon_B} \\ \sigma_{AB} &= \frac{1}{2}(\sigma_A + \sigma_B). \end{aligned} \tag{2.29}$$

A list of values of ϵ and r_e, for the special case in which LJ is implemented for VdW interactions, for all elements in the periodic table, is given in the paper of Rappé *et al.* [66]

In covalent crystals, however, it is better to use other potentials. The Morse potential, [67] is maybe the best simple representation that can handle the strength created by a bond, but it requires the introduction of a third parameter. Its functional form is given by

$$V_M(r) - D = D\left(e^{-2a(r-r_e)} - 2e^{-a(r-r_e)}\right) \tag{2.30}$$

or

$$V_M(r) = D\left(1 - e^{-a(r-r_e)}\right)^2. \tag{2.31}$$

Here, D is the bond dissociation energy, r_e is the equilibrium bond distance, and a controls the width of the potential. From a Taylor expansion around the equilibrium position, it is easy to show that the potential is harmonic with an elastic constant k_e given by

$$k_e = 2Da^2, \tag{2.32}$$

then, the Morse potential can be replaced by a harmonic approximation, when atoms of molecules or covalent crystals are at low temperature, that is

$$V_M(r) = \frac{k_e}{2}(r - r_e)^2. \tag{2.33}$$

In a general approach, Morse can be used to describe bonds between atoms with computational ease. It works particularly well for diatomic systems, and only the fitting of the bond strength, vibrational frequency and equilibrium distance is needed. The parameters can be also determined by using the lattice parameter, bulk modulus, and cohesive energy. [68] Morse shows almost one-to-one correspondence between parameters and measurable quantities.

On the other hand, the LJ is well suited for noble gases or cases where the interaction energy is of the order of milli-electronvolts, as for example, atom-molecule or molecule-molecule interactions, in which the atoms of any particular molecule are not interested in forming bonds with such atoms, or atoms of the other molecules, i.e., all those systems

where there are no electrons available for bonding and atoms attract each other through for example VdW forces. Examples of the use of LJ are Ar-Ar, benzene-benzene, Au-graphene or PE-Au interactions.

It is also possible to do combinations of the LJ and Morse potentials, the latter for intra-molecular interactions and the former for intermolecular ones (see Equation (2.26)). This last particular representation is implemented for the description of the molecule of PE in the framework of the coarse grain approximation (see Section 3.2 on page 43).

2.5.5 Sophisticated potentials

When a detailed description of certain properties is required, simple potentials are not enough. Contrary to noble gases or stable neutral molecules, for metallic and covalent bonding systems a proper description requires the consideration of the many body effects.

Different approaches have been considered for going beyond pair potentials and to incorporate the additional many body effects. One obvious approach is the addition of higher order interactions. For that purpose, the general expression of a N-body potential in which the coordinates of the nuclei are located at $\mathcal{R} : \{\mathbf{r}_1, \mathbf{r}_2, ..., \mathbf{r}_N\}$ is used

$$\mathcal{V}(\mathcal{R}) = \sum_i V_1(\mathbf{r}_i) + \sum_{i<j} V_2(\mathbf{r}_i, \mathbf{r}_j) + \sum_{i<j<k} V_3(\mathbf{r}_i, \mathbf{r}_j, \mathbf{r}_k) + \dots \qquad (2.34)$$

The first term is related to external forces and it is not considered, the second is the pair interatomic potential, and the third is usually the angular dependence. The addition of higher other terms provides more accuracy, but is computationally costly. Other more successful approaches than Eq. (2.34) are the introduction of functions that depend explicitly on the electronic densities like in metals, or the use of an artificial representation of bond formation between atoms like in covalent systems. These approximations are explained as follows.

The Embedded Atoms Method (EAM) potential. This method was developed by Daw and Baskes as a formalism for describing metals. [69, 70, 71, 72] It is based on the earlier theory of the quasiatom [73] or effective medium (EM). [74] The main idea is that each atom in a solid can be viewed as an impurity embedded in a host composed of all the other nearest neighbors atoms. In this approach, the total cohesive energy is given by

$$\mathcal{V}_{EAM}(\mathcal{R}) = \sum_i F_i(\rho_{h,i}) + \frac{1}{2} \sum_{i,j(i\neq j)} \phi_{ij}(r_{ij}), \qquad (2.35)$$

where ϕ_{ij} is a pair potential function, and F_i is a universal function that depends on the densities of all other atoms different to i. The density in the point $\mathbf{r}_i$ is given by

$$\rho_{h,i} = \sum_{j,(i \neq j)} \rho_j^a(r_{ij}). \tag{2.36}$$

The sum is over the neighbors of the atom i, with ρ_j^a being the contribution of each of them. Angular interaction can be incorporated through the density. This potential is well suited for alloys, e.g, a metal cluster impinging another metal. [72] Although this potential is not used in this thesis, it is useful for making comparisons with the other potentials.

The Molecular Dynamics Monte-Carlo CEM (MD/MC-CEM) potential. One of the best potentials to describe fcc metals is the MD/MC-CEM potential. In essence, it is a simplified and convenient parametrization of the Corrected Effective Medium theory (CEM), which is implemented for monte-carlo (MC) and molecular dynamics (MD). [75, 76] It provides a lower accuracy if it is compared to CEM, but it is several orders of magnitude faster and as fast as other methods like EAM. In addition, it has the advantage that it gives a better description of surface properties than EAM. [77] The essential idea is to adjust the CEM embedding function to include the explicit correction of the kinetic-exchange-correlation energy differences between the real system and the many atom-jellium (where jellium is an infinite homogeneous electron gas with a uniform compensating positive density) implemented as the zeroth-order model. [75] In this model, the interaction energy of the entire system (cohesive energy) represented by a set of atoms $\{A_i, i = 1, ...N\}$ and with coordinates of nuclei located at $\mathcal{R} : \{\mathbf{r}_1, \mathbf{r}_2, ..., \mathbf{r}_N\}$ can be written as

$$\mathcal{V}_{\Delta E}(\mathcal{R}) = \sum \Delta F_J(n(\mathbf{r}_i)) + \frac{1}{2} \sum_i \sum_{j \neq i} V_C(\mathbf{r}_i, \mathbf{r}_j). \tag{2.37}$$

In this equation, the first term is the sum of the embedding energies ΔF_J for each atom A_i in a effective jellium density $n(\mathbf{r}_i)$. The jellium density is defined as a superposition of the unpolarized atomic electron densities obtained from the "Hartree-Fock" theory

$$n(\mathbf{r}_i) = \frac{1}{2Z_i} \sum_{j \neq i} \int n(\mathbf{r} - \mathbf{r}_i) n(\mathbf{r} - \mathbf{r}_j) d\mathbf{r}. \tag{2.38}$$

The last term in (2.37), is the sum of atom-atom Coloumb integrals for

each pair of atoms. It is of the form

$$V_C(\mathbf{r}_i, \mathbf{r}_j) = \int \frac{[n(\mathbf{r} - \mathbf{r}_i) - Z_i\delta(\mathbf{r} - \mathbf{r}_i)]\,[n(\mathbf{r}' - \mathbf{r}_j) - Z_j\delta(\mathbf{r}' - \mathbf{r}_j)]}{|\mathbf{r} - \mathbf{r}'|} d\mathbf{r}d\mathbf{r}', \tag{2.39}$$

where Z_i represents the charge of the atom i and this atom can be any atom of the periodic table. ΔF_J is a function of the jellium density, and is the only parameter that is fitted to experimental data. It can be obtained either for experimental data of homo-nuclear diatomic and bulk systems, [76] or from linear muffin tin orbital (LMTO) calculations for bulk systems. [78, 79] All the integrals are evaluated through the use of Chevyshev smoothing techniques (more exactly numerical integration using Gauss Chevyshev quadrature), in a equally spaced grid using inverse square distance and cubic polynomial interpolation for the functions. For more details about the implementation see Ref [75].

This potential is not suited for systems where small energies are critical. Energy differences of the order of 0.1 eV must be treated with caution. It works particularly well for bulk systems that are greater than 9 layers due to its long range interactions. Another advantage is that it works reasonably well at short distances, making it suitable for collisions. In addition, for cluster formation in the sputtering process, it has been shown that the MD/MC-CEM potential allows a much more realistic description of the small clusters than the EAM potential. [77, 54]

Tersoff-type potentials. This is a family of potentials developed by Tersoff, [80, 81, 82, 83] and they are based on the concept of bond order initially proposed by Abell [84]. In these potentials the idea of N-body potential (2.34) is abandoned and replaced by the central idea that, in real systems, the strength of each bond depends on the local environment. Unlike traditional methods this idea makes possible the successful treatment of covalent bonding interactions without using quantum mechanics. All parameters are entirely derived from the system geometry, treating the electronic degrees in a purely empirical manner. In the beginning the formalism was developed for modelling the group IV of the periodic table, and later extended to a broader spectrum of situations like semiconductors and hydrocarbons. [85] Their base functional form is

$$\mathcal{V}_T(\mathcal{R}) = \frac{1}{2}\sum_{i,j}\left[V_R(r_{ij}) + b_{ij}V_A(r_{ij})\right], \tag{2.40}$$

where V_A and V_R are the attractive and repulsive functions which depend on the distance r_{ij} and atomic types i and j, and their functional form depend on the specific Tersoff-type potential chosen. The main feature is the term b_{ij}. It is the bond-order function, which carries all many body

effects such as many body bonding topologies, bond angles, coordination numbers, etc. In fact, all variety of chemical effects that affect the bond strength are in this term. These potentials are not pair potentials because b_{ij} is not a constant and depends on the local environment:

$$\begin{aligned} b_{ij} &= b(G_{ij}) \\ G_{ij} &= \sum_{k(\neq i,j)} f_c(r_{ik}) g(\theta_{jik}) f(r_{ij} - r_{ik}). \end{aligned} \tag{2.41}$$

In this term, g is a penalty function that imposes a cost on bonds that are closer, the f_c term is bond-weighting factor that switches off interactions as a function the bond distance, and f is usually represented as a exponential function.

One particular case of the Tersoff-type potential is the reactive empirical bond-order potential (REBO) defined by Brenner for describing covalent bonding interactions in carbon and hydrocarbon systems. [86, 87, 88] REBO has been especially designed to reproduce properties of diamond structures, graphitic ribbons, graphene, amorphous graphite, and C_{60} reaction with surfaces. [85, 89] Its parametrization functions have been improved through the time, being distinguished as first and second generation. [90] In the latter, the improved repulsive function is represented by a screened Coloumb potential with effective charge Q, or

$$V_R(r) = \left(1 + \frac{Q}{r}\right) A e^{\alpha r} \tag{2.42}$$

and the attractive function represented by

$$V_A(r) = -\sum_{n=1}^{3} b_n e^{-\beta_n r}, \tag{2.43}$$

where Q, α, b and β depend on the interacting atom types.

Finally, a close relationship has been probed between Tersoff and EAM. It has been shown that for a reasonable choice of the functional forms and parameters, the two potentials are identical. The main difference is the manner in which angular interactions are incorporated. [91]

Adaptive Intermolecular REBO potential (AIREBO). Despite the success of REBO with hydrocarbon systems, the absence of dispersion and non bonded repulsion term in the potential constitutes a drawback for the study of systems composed of intermolecular interactions like liquids, hydrocarbon compounds, graphite and polymers. In the AIREBO potential, this problem is solved by adding to the REBO cohesive energy

(2.40) a term for handling intermolecular interactions and another which introduces the dependence with dihedral angles, that is

$$\mathcal{V}_A(\mathcal{R}) = \mathcal{V}_{REBO}(\mathcal{R}) + E_{LJ}(\mathcal{R}) + E_{rot}(\mathcal{R}). \tag{2.44}$$

Intermolecular interactions are introduced through an adaptive treatment of them. This is done by the implementation of a switching function, hence its name AIREBO. This switching function is a multiplicative weighting factor that is used first, to eliminate switching off smoothly the interfering produced on the REBO term by the term r^{-12} of LJ; second, to switch off smoothly the repulsive and attractive parts of REBO energy. In the former when interacting atoms exceed typical bond distances, and in the latter for non-short ranges interactions. Third, to ensure that the torsional energy of the dihedral angles be removed smoothly as any of the constituent bonds be broken.

In summary, the historical sequence in the development of potentials for hydrocarbon systems is *Abell* $\rightarrow$ *Tersoff* $\rightarrow$ *REBO* $\rightarrow$ *AIREBO*. The last one is a sophisticated generalization, which can be considered as a universal hydrocarbon force field. For more details see the Ref [92].

Intermolecular interactions, Universal Force Field (UFF). This is a model in which the bonding interactions are treated as a superposition of four terms given by the N-body equation (2.34). More exactly,

$$\mathcal{V}_{UFF} = \underbrace{(E_R + E_\theta + E_\phi + E_I)}_{\text{bonded}} + \underbrace{(E_{VdW} + E_{el})}_{\text{not bonded}} \tag{2.45}$$

where the terms are, the two body bond stretch E_R, three body bond-angle bend E_θ, and forth bodies dihedral angle torsion E_ϕ and inversion term E_I. The bond and angle terms are usually modeled using harmonic oscillators or Morse representations, while the other terms have more various functional forms. The nonbonded interactions E_{VdW}, are usually treated with a simple LJ term, and Coloumb representation for the E_{el} term. The parametrization and functional forms for each of the terms can be found in the Ref [66, 93]. Also, another more sophisticated force field (ReaxFF) than UFF - and with better parametrization - has been created for Hydrocarbons, for more details see Ref [94].

2.5.6 Repulsive interatomic potentials

At very small distances almost all the potentials described above fail to describe interactions properly. In most of the cases they were developed for minimization of the energy and optimization of geometrical structures and not for collisions with an energy of the order of the keV.

For instance, LJ is too repulsive with its r^{-12}, and Morse too soft. In fact, at very small distances, the repulsive interaction between the nuclei can be regarded as essentially Coulombic

$$V_R(r) = \frac{1}{4}\pi\varepsilon_0 \frac{Z_1 Z_2 e^2}{r}\phi\left(\frac{r}{a}\right), \tag{2.46}$$

where ϕ is a "screening function", Z_1 and Z_2 are the atomic numbers of the atoms in the collision, r is the interatomic distance, and a is called the "screening length". [95, 96] The most common repulsive potentials are the Molière V_{Mol}, Krypton-Carbon V_{KrC}, Universal V_{Univ} of Ziegler-Biersack, and Sommerfield V_{Som}, with screening functions represented by

$$\begin{aligned}
\phi_{Mol}(x) &= 0.35e^{-0.3x} + 0.55e^{-1.2x} + 0.1e^{-6x} && (2.47)\\
\phi_{KrC}(x) &= 0.190945e^{-0.278544x} + 0.473674e^{-0.637174x} \\
&\quad +0.335381e^{-1.919249x} && (2.48)\\
\phi_{Univ}(x) &= 0.1818e^{-3.2x} + 0.5099e^{-0.9423x} \\
&\quad +0.2802e^{-0.4029x} + 0.02817e^{-0.2016x} && (2.49)\\
\phi_{Som}(x) &= \left(1 + \left(\frac{x}{12^{2/3}}\right)^{0.8034}\right)^{-3/0.8034} && (2.50)
\end{aligned}$$

where $x = r/a$. Those functions can be considered as "universal" in the sense that they are independent of the colliding atoms types, i.e., they are independent of Z_1 and Z_2. For the screening length, there are different possible options, all based on the Thomas-Fermi function

$$a = \frac{0.88534}{(Z_1^m + Z_2^m)^n} a_{Bohr} \tag{2.51}$$

with (m, n) being $(1/2, 2/3)$ or $(2/3, 1/2)$. In the case of V_{KrC} and V_{Univ} newer improved coefficients $(0.23, 1)$ are implemented. In all the cases, the screening factor is multiplied by a value f (called Firsov corrector factor) in order to have a better match with the experimental results for Z_1 and Z_2, that is

$$a_{corr} = af \tag{2.52}$$

with

$$\begin{aligned}
\text{Mol: } f &= (0.045 \pm 0.003)\left(\sqrt{Z_1} + \sqrt{Z_2}\right) + (0.54 \pm 0.02)\\
\text{KrC: } f &= (0.013 \pm 0.003)\left(\sqrt{Z_1} + \sqrt{Z_2}\right) + (0.79 \pm 0.03)\\
\text{Univ: } f &= (0.001 \pm 0.004)\left(\sqrt{Z_1} + \sqrt{Z_2}\right) + (0.95 \pm 0.03)\\
\text{Som: } f &= (-0.022 \pm 0.004)\left(\sqrt{Z_1} + \sqrt{Z_2}\right) + (0.61 \pm 0.03)
\end{aligned}$$

Once an interaction potential has been chosen to model a particular system, its non-physical behavior at short-range distances must be corrected. Then, at short-range distances the potential is replaced by a repulsive type potential (usually Molière) which provides an acceptable description of such high energy collisions. The coupling between the two potentials is done via a polynomial function. The potential used for sputtering is

$$Vs(r) = \begin{cases} V_R(r) & \text{if } r < r_{min} \\ V_{Pair}(r) & \text{if } r > r_{max} \\ V_{Spline}(r) & \text{if } r_{min} < r < r_{max} \end{cases} \tag{2.53}$$

where

$$\begin{aligned} V_{spline}(r) &= \left((1 - S(x))\, V_R(r) + S(x) V_{pair}(r)\right. \\ S(x) &= x^3 \left(6x^2 - 15x + 10\right) \\ x &= \left(\frac{r - r_{min}}{r_{max} - r_{min}}\right) \end{aligned} \tag{2.54}$$

where r_{min} and r_{max} are two values that must be carefully chosen. They permit that the specific pair and repulsive potentials match at these values, as well as their first and second derivatives. V_{Pair} represents the dominant pair potential term of the potential to be matched with the Molière. The standard procedure to choose r_{min} and r_{max} is to plot the forces and see where they are equal, r_{min} and r_{max} are chosen around this point. Graphs of the repulsive potentials and spline of Molière with the Morse potential are shown in Figure2.8. The MD/MC-CEM and AIREBO potentials do not require a Molière at short internuclear separations, because they have included they own Coloumb terms (see terms (2.39) and (2.42)).

2.6 The SPUT code

The SPUT code is a MD program developed for the simulation of keV particle bombardment (sputtering) of solids. The current program has been developed by *Barbara J. Garrison* and collaborators. The SPUT code has been written in fortran 90, and there are several different versions, "SPUT2005" and "SPUT2007" are the versions used herein. The potentials and integration methods discussed below have been all implemented into the code. The fifth-order Gear predictor-corrector is implemented to integrate the equations of motion, and a lower-order integrator using Taylor expansion is used for atoms subject to stochastic

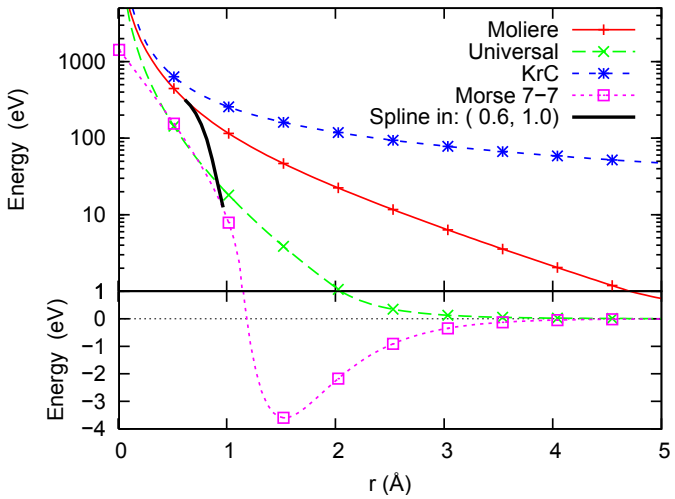

Figure 2.8: Graphs of the repulsive potentials and spline of Molière with the Morse potential in the interval $(r_{min},\ r_{max}) = (0.6, 1)$, for the case when $Z_1 = Z_2 = 7$. The Firsov factor f used for the Molière function is $0.69 + 0.0051(Z_1 + Z_2)$, and 1 for the KrC and Universal functions.

forces. These integrators have been implemented to handle situations involving high energies and large mass differences, and for a moderate cost in CPU time. Therefore, one can expect to obtain energy conservation in the order of 1-10 meV.

The key of the code efficiency is based on three main features. First, to calculate the forces between N interacting atoms, an array with a list of neighbors or "neighbor list" is implemented, reducing the computational cost from computing $N \times N$ interactions, to calculating $N_{nei} \times N$ interactions (with N_{nei} being the number of neighbors of each atom). Second, this neighbor list has to be refreshed after some time, and that means to calculate again $N \times N$ interactions. To avoid that, the space is divided in boxes or "subcells" with a size of the largest cutoff distance of the potentials r_c. In this way, for each particle, it is only needed to calculate the interactions with the neighbors N_C inside of the box where it belongs and with the other 26 nearest boxes. In this manner the computational time is reduced to calculate $27N_C \times N$. In addition, because the SPUT code was developed to handle with solids, the list is only updated for those atoms which move faster and go outside of the neighbor list (most of the atoms remain close to the equilibrium position), hence reducing additional computation. A third important feature of the code is the ability to increase and decrease the timestep as the equations of motion soften and stiffen. It is done by using a variable

timestep size, which is calculated with the magnitude of the third and fourth derivatives. These functions reach their maximal value when the forces are changing rapidly and approach zero when the motion becomes more harmonic and thus provide the necessary gauge to control timestep.

Finally, cubic polynomial interpolations for several of the potential energy and force functions as well as for their differentiation are implemented in the form of tabular data. For that, SPUT has an efficient cubic polynomial interpolation scheme which performs these operations. For more details of the code see Garrison's notes. [97]

2.7 How to handle ionization in simulations

The ideal way of handing the ionization is via the introduction of the electronic subsystem, that is properly treated by quantum mechanics. It can be done through the use of *ab initio* theories, i.e., methods that do not need to use or introduce experimental parameters (as for example lattice and elastic constants, cohesive energies, etc), and which only require a specification of the present ions, which are represented by their atomic numbers. [98, 99] Of these methods, one that was considered as a promising one, and that was created ∼30 years ago, is the Car-Parrinello method. It introduces the calculation of forces into the lagrangian from quantum mechanics on the fly. [100] However, this *ab initio* method demands to first relax the electronic part, which requires minimization of the total energy with respect to all the degrees of freedom, thus the integration of the equations of motions for the ions is not straightforward. Therefore, this method is limited to small systems of 10-300 atoms. Also other methods exist in the frame of Density Functional Theory (DFT), but again, they are only for small systems. [99] Nonetheless, some interesting works have been done using these techniques. [101, 102, 103, 104] For instance, in a recent work Time Depending Density Functional Theory (TD-DFT) is used to analyze the charge transfer between a colliding butane molecule and gold atom. [105] That system is implemented to understand the fundamentals of the charge transfer in the metal organic interactions - as in the MetA-SIMS case - typical of the keV bombardments.

On the other hand, the Wucher group has implemented another way to handle the electronic problem using MD for the specific case of metal surfaces. [106, 107, 108, 109] In addition to the description of the atomic collision cascade initiated by the particle impact, their model incorporates the electronic degrees of freedom of the target. Therefore, it is capable of simultaneously predicting secondary ion formation in sputter-

ing as well as ion-bombardment-induced kinetic electron emission. They consider their method as an approach to close the gap between classical MD simulations usually excluding electronic effects and *ab initio* methods. [110, 111, 112, 113, 56] With this method, Duvenbeck in his thesis, [55] shows that about 60% of the kinetic energy imparted by the Ag projectile into the $Ag(111)$ solid is dissipated into electronic degrees of freedom rather than the collision dynamics.

The main idea of the latter model consists in considering that the atomic collision cascade is embedded into a free electron gas characterized by its Fermi energy E_F, density n_e and electron mean-free path λ. The kinetic excitation is given via direct atom-electron collisions in the framework of the Lindhard theory of electronic stopping which yields a velocity-proportional friction force acting on every moving cascade atom, [114] i.e., the electronic energy loss dE_k within the time interval dt for the ith particle is proportional to its kinetic energy E_k, or

$$\frac{dE_k}{dt} = -Kv^2 = -AE_k, \tag{2.55}$$

where A is a constant equal to $2.9{\times}10^{12}$ s^{-1} for the specific case of an Ag atom moving in silver.

However, this method has only been implemented to calculate the dynamics of keV $Ag \rightarrow Ag(111)$ bombardment in order to predict kinetic electron emission yields. Nothing is said about other metals different to silver and the possibility of implementing the method to insulators or organic materials.

Despite the important work accomplished to understand ionization, a generally applicable model is still needed.

Chapter 3

Metal organic models

This chapter is dedicated to all the computational and theoretical details of the construction of the specific systems that will be used as sample/target to be interrogated with different projectiles and under different initial conditions. The Section 3.1 is concerned with the geometrical construction of the polymer. Then, the physical coarse grain approximation of the polymer - needed to reduced the computational time - is discussed in Section 3.2; and finally, Section 3.3, explains how metal deposition on the polymers is done. The models are compared to the experimental work found in literature.

3.1 Organic sample model: polyethylene

Nowadays polymers play an important role in materials science, they have a number of applications, for example in the development of new materials, in the production of semiconductors, medicine, surface analysis etc. [115] As a proof of the importance of polymers in our world, the current volume of polymers used for commercial and industrial applications already exceeds the volume of aluminium and steel combined. Motivated by this, the polyethylene (PE) material has been chosen as the model for the organic system representation in this study. The main reason of this choice is the simplicity of this material and its well known properties. [116, 117]

3.1.1 Experimental parameters of the polyethylene

The PE is a structure formed by chains, and it has two main representations for its bulk structure: crystalline and amorphous. More specifically, each PE molecule chain is formed by the polymerization in

one direction of ethylene molecules, which are formed by 2 carbons and 4 hydrogen atoms. Normally, at the ends of each chain, there are 3 hydrogen atoms, which make the chains chemically stable.

The molecular chains in a crystalline structure are regular and periodic with C-C zigzag theoretical angle of 112° and bond length of 1.533 Å. The C-H bond length is 1.07 Å and the H-C-H bond angle is close to 107°, each chain is formed by links with periodicity in z direction of $c = 2.548$Å. [116] As an example, the geometrical model of 2 chains is shown in Figure 3.1.

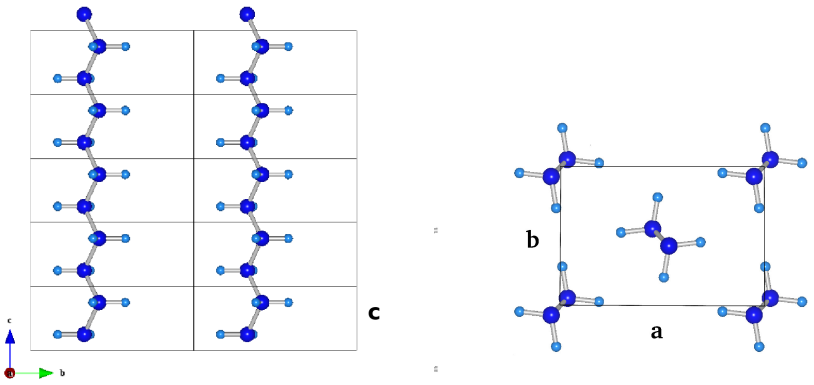

Figure 3.1: Left: two molecular chains, with periodicity in z direction of $c = 2.548$ Å. Right: Ideal orthorhombic unit cell with lattice parameters $a = 7.121$ Å, $b = 4.851$ Å. Only the six atoms inside of box are needed to reproduce the unitary cell.

The crystalline structure is an orthorhombic unit cell forming a rectangular packing with a central molecule having its plane perpendicular to the molecules located at the corners of the rectangle as is shown in the right hand of Figure 3.1. This primitive cell contains twelve atoms which belong to two equivalent chains (one in the corner and another in the cell center) which belong to the space group *Pnam*. [118] Unlike the chain, to properly describe the crystal structure, nine parameters are needed: the lattice parameters a, b and c, and six internal coordinates represented by the numbers c_1, c_2 for carbons, and h_1, h_2, h_3, h_4 for hydrogen atoms. These numbers determine the positions of all atoms in (x_f, y_f, z_f) fractional coordinates, or

$$
\begin{aligned}
\mathrm{C} &= \pm\left(c_1, c_2, \frac{1}{4}\right) \\
\mathrm{H} &= \pm\left(h_1, h_2, \frac{1}{4}\right) \\
\mathrm{H} &= \pm\left(h_3, h_4, \frac{1}{4}\right) \\
\mathrm{C} &= \pm\left(\frac{1}{2} - c_1, \frac{1}{2} + c_2, -\frac{1}{4}\right) \\
\mathrm{H} &= \pm\left(\frac{1}{2} - h_1, \frac{1}{2} + h_2, -\frac{1}{4}\right) \\
\mathrm{H} &= \pm\left(\frac{1}{2} - h_3, \frac{1}{2} + h_4, -\frac{1}{4}\right)
\end{aligned} \tag{3.1}
$$

with $c_1 = .044183$, $c_2 = 0.059859$, $h_1 = 0.186360$, $h_2 = 0.011509$, $h_3 = 0.027079$ and $h_4 = 0.277646$, those parameters are calculated from the bond distances and angles. The cartesian coordinates in Angstroms are given by

$$\mathrm{X}_{angs} = \pm\left(x_f a, y_f b, z_f c\right)$$

where $a = 7.121$ Å, $b = 4.851$ Å and $c = 2.548$ Å are the lattice parameters measured at 4 K. [119] The former coordinates with periodic conditions are enough to create a crystal with the wanted crystal size. More explicitly, any atom n in the crystal will have the coordinates

$$R_n = \pm\left(n_1 + x_f a, n_2 + y_f b, n_3 + z_f c\right) \tag{3.2}$$

with n_1, n_2, n_3 being the integer lattice points which give the periodicity of the crystal. If only one chain is needed, for example in the z direction, only the first three expressions of (3.1) are needed. In this case the periodicity is only in the third component of these expressions.

On the other hand, in an amorphous structure, only the inter atomic distances are conserved. In this case the chains are entangled when forming the structure.

3.2 Coarse grain approximation

As it was mentioned at the end of Section 2.4.1, one of the main problems in MD is to reduce the computational time required to do one simulation in huge systems. In contrast to covalent and metallic systems,

MD simulations of keV energy impacts on organic materials require the use of bigger sample systems due to the presence of the VdW forces, which implies to use more atoms in the sample. Even worse, organic samples are mainly composed of carbon and hydrogen atoms. The latter presenting fast vibrations that require to reduce the integration time step. This is the most critical problem. On one hand, full atomistic simulations can be implemented by using the AIREBO potential (2.44). However, that will include around 300 neighbours per atom. On the other hand, the use of simple potentials, as it is expressed by the UFF (2.45) allows to avoid introduction of such a quantity of neighbours, although some precision is given up. Even in the latter approximation, simulations of the organic systems are almost impossible with the computational resources that we have today. Then how to get rid of that problem? One of the solutions is to apply the Coarse Grain approach (CG), which consists in grouping two or more atoms to form an entity that represents the global properties of the group. More exactly, in this work, it consists in combining the carbon and hydrogen atoms to form a single coarse grained particle. That is explained in more detail in the next section.

3.2.1 Geometry and physical parameters of PE in the coarse grain approach

In the PE case, CH_2 and CH_3 subunits were united to form single CG entities of 14 and 15 amu, respectively. These CG entities were placed at the carbon positions according to the equations (3.1). In this specific case, the interacting molecular and intermolecular potential are constructed with the Morse (2.30) and LJ (2.27) pair potentials to describe both bonding as well as VdW interactions between the CG particles that form the molecules. The potential is

$$V_{CG}(r_{ij}) = \begin{cases} V_M(r_{ij}) \text{ or } V_{LJ}(r_{ij}) & \text{if } i,j \text{ are in the same molecule} \\ V_{LJ}(r_{ij}) & \text{if } i,j \text{ are in different molecules.} \end{cases} \tag{3.3}$$

In the same molecule, for each atom i, first and second neighbours interactions are handled by Morse, and third, four, etc, neighbours by LJ. At short distances, both terms should be substituted by a repulsive potential (2.53). In each chain, Morse equilibrium distance between consecutive CG entities (first neighbours) is set to 1.54 Å, and in order to simulate the zigzag structure of PE, an additional Morse interaction with each second neighbour is added, with an equilibrium distance equal to the periodicity c in z direction, or $r_e = 2.52$ Å (see in Figure 3.1). In the Morse potential (2.30), the cohesive energies are set to 3.6 eV and 0.03 eV respectively, both with a width of $a = 2$ Å. This trick allows us to

keep the zigzag structure, avoiding the need of the expensive three body angular dependence.

To be in a better agreement with experimental data, the LJ equilibrium distances for intermolecular and VdW interactions were obtained by relaxing the sample at 4 K. [120] To achieve this goal the temperature-dependent lattice parameters were redefined by

$$\begin{aligned} a(T) &= (7.74053 + 0.000471 \times (T - 400)) \\ b(T) &= (4.45817 + 0.000261 \times (T - 400)) \\ c(T) &= (2.52748 + 0.000014 \times (T - 400)) \end{aligned} \tag{3.4}$$

which gives a = 7.554 Å, b = 4.355 Å and c = 2.522 Å. Based on this orthorhombic unit cell, crystal samples were modeled using chains formed of 200 elements (198 CH_2 and 2 CH_3 at the chain ends). The best agreement of the LJ equilibrium distances with the experimental lattice parameters were $r_e = 4.335$ Å for CH_2-CH_2, and $r_e = 4.381$ Å for both CH_2-CH_3 and CH_3-CH_3 interactions. The cohesive energies were set to 0.0052 eV, 0.0062, and 0.0076 eV respectively. [66]

3.2.2 Advantages and drawbacks of the coarse grain approach

Although CG has been widely used in the sputtering of organic systems, in its origin it was implemented to explain structure properties in which the attractive part of the potential energy was dominant. [121] The main goal was to avoid the problem of hydrogen vibrations and, hence, very short time steps. Still, in simulations of the sputtering process in which the repulsive part has an important role, a better justification of how it should be understood is needed. At short distances interactions are repulsive and the dominant forces are between pair of atoms. At such distances, molecules (or CG entities) do not exist for the potential; therefore, such CG approximation does not seem to be valid anymore. Thus, what does one understand of CG, in order to justify its use? First, due to the large difference between carbon and hydrogen masses, the main contribution to the total sputtered mass comes from carbon. Second, as it is said in Section 2.2 on page 11, the main contribution to the stopping power is nuclear (transfer of momentum from the energetic particles to target), therefore, at short distances the transfer of the energy is mainly between the heavy atoms, hydrogen does not influence too much. However, one fact of the CG is that, in contrast to the full atomic representation, in the CG the energy is not used to break C-H bonds (in a full atomistic system, each broken bond costs around 3.5 to 5 eV), so

collisions of CG entities are totally elastic. Therefore, this energy, which is not spent as internal energy, should be transferred to the CG system, hence, an increase of total yield should be observed. Nonetheless, from Equation (2.3) the maximum energy transfer is when particles masses are equal. Therefore, one should expect that energy transfer be mainly between carbons and that not too much be spent in C-H collisions.

One important disadvantage of the CG approach is in chemical analysis of fragments. For example, in the case of large chains of PE, CG does not allow to obtain $C_nH_{2n\pm m}$ fragments (here m represents the hydrogen atoms that are tied to the ends of the fragments of chains and takes values from one to four). In the CG approach, these hydrogen atoms are ignored. Now, considering the differences between the masses of carbon and hydrogen, the CG fragments will have an error in their total mass that will depend more or less on the presence or absence of any of the four hydrogen atoms at the ends. An explicit calculation of the relative error for the footprint of the first fragments of the spectra is given in Table 3.1.

n	Mass (Da)	m	Error
1	14	2	14.29 %
2	28	4	14.29 %
3	42	4	9.52 %
7	98	4	4.08 %
14	196	4	2.04 %

Table 3.1: Relative error of mass of PE fragments $(m/14n) \times 100$ % in the CG approach ($C_nH_{2n\pm m} \approx C_nH_{2n}$). The error is calculated over the maximum number m of hydrogen atoms that can be ignored in the fragmentation process of one chain for each fragment (third column). Only the 4 H in the two ends of the fragment are considered.

Thus, how should CG be interpreted? From the previous observations, CG is an approximation in which some atoms are grouped to form one entity that approximately keeps the main physical properties of the system. That is, CG and full atomic simulations approximately desorb the same quantity of mass and volume, and produce almost same stresses and pressure waves. A comparison of CG and full atomistic systems using AIREBO for benzene target was done. [122] These simulations have shown that CG reproduces well the essential physical properties of the system and reduces the computational time from six months to 4 days. The results can be seen in Figure 3.2. Finally, CG is more suited for studying physical properties such as, crater formation, total sputter

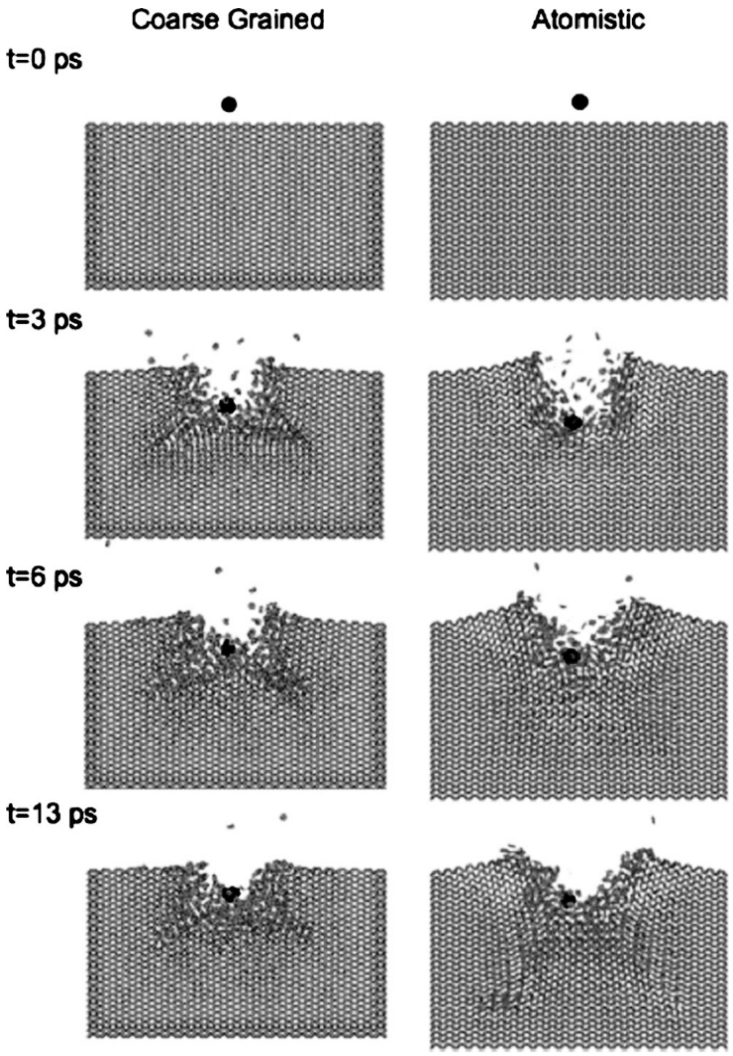

Figure 3.2: Cross-sectional view of the temporal evolution of a collision event by 500 eV C_{60} bombardment. The sample size for the CG calculation is $17.03 \times 9.17 \times 16.89$ nm^3 and $17.03 \times 9.86 \times 6.89$ nm^3 for the atomistic calculation implemented with AIREBO potential. A slice of 1.5 nm wide in the center of the system is shown. The atomistic simulation is two layers larger than the CG case. Taken from ref [122]

yield, ranges, total kinetic energy of fragments, and emission yield of intact molecules.

3.3 Metal-organic systems

As it has been said before, a metal-organic system consists in the combination of an organic material with a metal, in this case PE and gold have been chosen. Three different samples have been created, the first is a gold-coated PE box structure, "*sample A*", the second is a combination of two slabs with a vertical interface between the PE and gold crystals, "*sample B*" and the third, "*sample C*", is an amorphous PE structure also covered with gold, as the *sample A* (see in Figure 3.3). In *sample B*, the slab of PE has a crystalline structure (as it is described by the coordinates (3.2)), and the slab of gold has a fcc structure with a lattice parameter of 4.08 Å. In this specific case, only one third of the total volume of the sample is occupied by gold, and the other two thirds by PE. Indeed, a larger volume of PE is needed to contain the sputtering event and prevent the reflection of pressure waves on the edges. In the *sample A* and *sample C*, a random deposition algorithm has been implemented to create the initial conditions of the layer of gold over the PE, and its implementation is explained in detail in the next section.

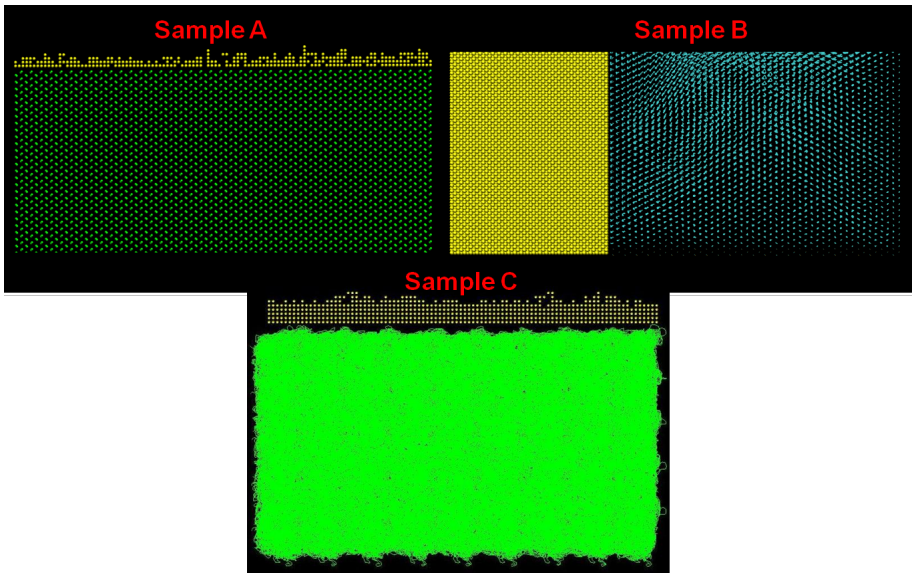

Figure 3.3: Sample A is a crystal of PE covered with gold atoms, and sample B is formed by two slabs of gold and PE. Sample C is an amorphous PE structure covered with gold atoms as in sample A.

3.3.1 Random deposition algorithm

From the macroscopic point of view, one can think that when a layer is created over a surface it becomes uniform, but from the microscopic view, that is not necessarily the case. The manner in which particles are deposited on the surface to form a film strongly depends on the technique used. For instance, particles can be evaporated from a hot filament (or with any other technique for evaporation), which involves a randomness in the emission and deposition process. Therefore, the expected structure should be rather a fractal than a uniform layer. Here, to mimic this fact, a random deposition algorithm is implemented to obtain a system that should be more realistic, and that should be in better agreement with the experiment. The idea of the random deposition algorithm is taken from the ref [123], which explains only the two dimensional case. Here, it is generalized to the three dimensional one. This algorithm is implemented to simulate gold deposition over PE, and the result obtained is used to give the initial conditions of the gold atoms in sample A.

The idea of the algorithm is to divide the space in cells where each cell has the lattice dimension of gold. Consider the plane xz with dimensions $LxLz$ and particles arriving in y direction, which has dimension Ly. An equally spaced grid is created by dividing Lx, Lz and Ly by segment of length a, in this manner a grid with Lx/a, Lz/a and Ly/a segments in each respective direction is obtained. Randomly, a point (i,k) in the plane xz is selected, and a particle is placed at an height $j(i,k)$ according to the following rule: if j is greater than all four neighbors j is increased by one, but if the place (i,k) is a hole, j will take the value of the highest neighbor. In other words:

1. Choose a random site (i,k).
2. Create an array $j(i,k)$ being the height of the column site (i,k).
3. Make the decision:

$$j(i,k) = \begin{cases} j(i,k)+1, \text{ if it is greater than all four neighbors} \\ \max[(i-1,k),(i+1,k),(i,k-1),(i,k+1)], \text{ if it is hole} \end{cases}$$

The process stops when a desired thickness d of gold is reached, or certain number of atoms is deposited. In this manner, a fractal structure is created showing empty regions throughout the gold deposition, and it represents a statistical growth of the film of gold over the surface.

The advantage of this algorithm over others, as for example to put the atoms randomly on the surface, is that each atom is placed in a manner that depends on the neighbors, which gives an homogeneous

distribution over the surface according to the real process of deposition into the chamber. This algorithm guarantees that each atom has at least one neighbor to interact with. In addition, its implementation reduces the computational time needed to form a realistic metal coated surface; it gives a input for MD, in which the interaction between atoms is allowed.

3.3.2 Results of the relaxation: NP formation

After the creation of the geometrical crystalline PE structure - using the carbon coordinates of the Equations (3.1) for each CG entity, which is placed in the lattice according to the Equation (3.2) - the PE surface is covered with gold using the algorithm explained before. The distance between the gold atoms and PE surface is fixed to 4 Å. However, this structure is not stable because interactions between particles are not taken in account. Therefore, the full structure (PE plus Au atoms) must be relaxed by using MD through several relaxation steps in which the excess of kinetic energy is removed until the wanted structure be obtained.

In the MD code, the PE-PE interactions between CG entities are done using the Equation (3.3). Gold interactions are handled with the MD/MC-CEM potential (2.37) and gold-PE interactions with a simple LJ potential with parameters $\epsilon = 0.012$ eV and $r_e = 3.41$ Å. These parameters are taken from the reference [66]. One reason for the choice of this value of ϵ is that metals and polymers are in most of the cases dissimilar materials, e.g., the cohesive energy of metals is typically two orders of magnitude higher than that of polymers. [27] Additionally, Au is one of the most inert metals, and its adhesion to polymers is expected to be lower than for others.

The final result of the relaxation process is the PE surface covered by a nanostructure of gold islets of various sizes with an average diameter around 20-30 Å. The equivalent thickness of the obtained Au layer (different from the thickness d used for the stopping condition), if it were uniform, would be 2.6 Å, which corresponds to a quantity of deposited gold of 2.6 nmol/nm^2. The obtained surface nanostructure is in good agreement with experiments for that quantity of deposited gold (scanning electron microscopy). [11] The top view of the sample before, during and after MD relaxations, compared to the experiment is shown in Figure 3.4. In more detail, the sample was obtained by using rigid boundaries of 5 Å and stochastic forces at 4 K over a region of 15 Å over the five sides (excluding the top with gold NPs). These boundary conditions were implemented using the Langevin equation to provide a heat bath during relaxation. The initial velocities of all atoms were set

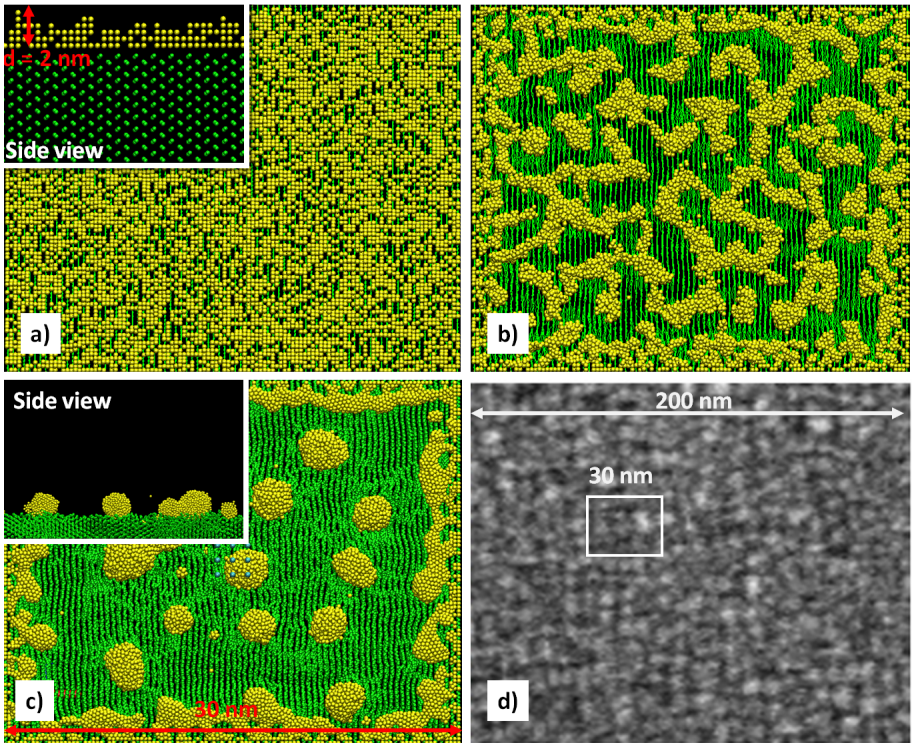

Figure 3.4: a) The random deposition of gold over PE gives a fractal structure. In b) islets after 10 ps. c) Second relaxation until 20 ps with the output of the first relaxation, velocities were reset to zero. d) SEM image of polystyrene covered with 2.0 nm equivalent layer thickness of *Au*, the small box is the equivalent area used in the simulations. (figure, Prabhakaran courtesy).

using a Gaussian distribution with temperature of 4 K. [116, 119] This value of temperature was chosen in order to obtain a good agreement with experimental values of the PE structure obtained at the same temperature (the justification of this is given in the Subsection 2.4.4 on page 25).

One of the most noticeable effects in the final coated sample is the border effects of gold distribution (see in Figure 3.4c). It is due to the use of rigid atoms at the borders. In principle, this effect could be eliminated by applying periodic boundary conditions. However, to obtain a distribution with a NP in the center, on the desired reaction zone is not easy. In addition, this border effect is negligible because it is far from the reaction zone where the crater and emission are produced. Therefore, this relaxation structure was kept.

The process of covering and relaxation of the amorphous PE, sample

C, is done in a similar manner.

3.3.3 Additional MD studies of the gold deposition over PE

Some preliminary tests and studies of the NP deposition and relaxation were done before choosing the model of study for the bombardments. They have shown that NP formation over the organic surface is very sensitive, not only to the initial conditions, but also to the manner in which the simulations are done, the temperature, the box size, the total number of atoms of gold deposited over the surface, the use of different stochastic conditions, etc. They may create different configurations with different NP sizes, distribution and morphology, as illustrated in Figure 3.5. For instance, to check the box size dependence, a small

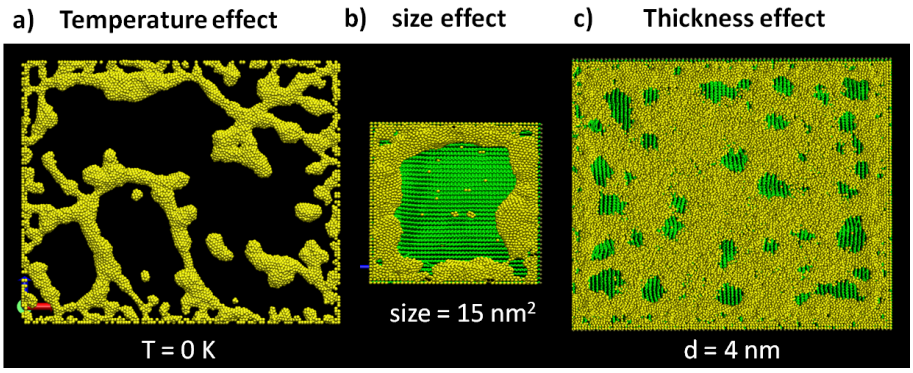

Figure 3.5: Structures obtained from three different initial conditions for the relaxation of gold on surface of crystalline PE. Effects in nano-islets formation when: a) the temperature is changed to zero, b) the box size of PE is reduced, and d) the thickness d or the quantity of Au atoms deposited on the surface is increased.

box of $15 \times 15 \times 15$ nm^3 was relaxed with gold atoms over it. After relaxation, gold atoms were all grouped at the edges of the box. In this case NPs were not formed. Moreover, changing the lattice parameters of gold in this box induced a large variation in the maximum reached by the temperature. Thus, if in the deposition gold atoms are too close, the repulsion increases the kinetic energy.

Other systems with different thicknesses have also been modeled, and they have shown temperature dependency as a function of the total number of deposited atoms (see in Figure 3.6). This is not surprising because these atoms were in an unstable configuration. More gold atoms means more kinetic energy at the expense of the initial potential energy

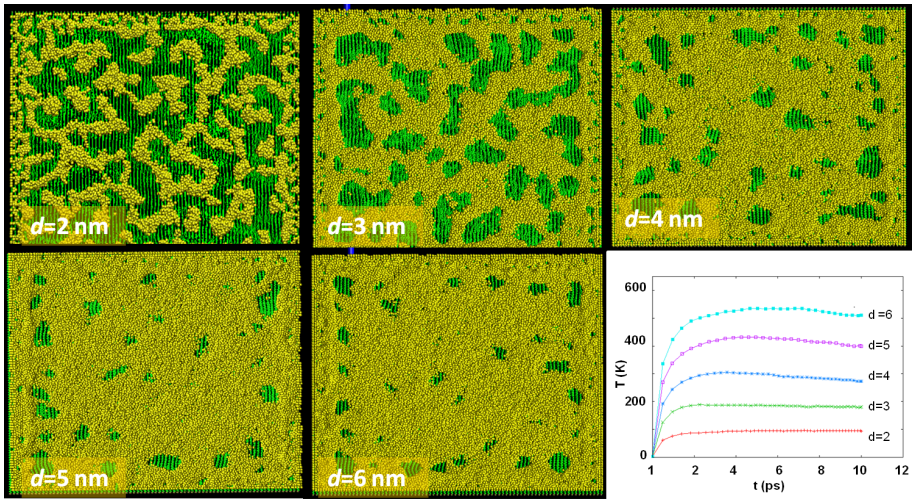

Figure 3.6: Relaxation with different thicknesses of gold until 10 ps. On bottom right corner, temperature as a function of the time.

of such an unstable configuration.

3.4 Conclusions

The construction of the polymer and its metalization has been discussed. The metal-organic samples created here will be used in the next chapters as targets for different projectiles. The MD results show how NPs are created over the PE surface when using the random deposition algorithm to give the initial conditions of the gold atoms. The NP formation with MD has been shown to be sensitive to the initial conditions - as well as to other parameters - that makes difficult to obtain the desired structure with the NPs over it. Though NP formation and relaxation over organic surfaces is a very interesting topic, which could for instance be of interest for industrial applications, no more simulations than those needed to obtain the desired structures for the bombardments were done. The remaining of this thesis is focused on the NP fragmentations and its effects on polymer sputtering, rather than metal-NPs formation and configuration over the organic surfaces.

Chapter 4

Monoatomic vs small cluster projectiles

Molecular and chemical information are strongly related to the conditions in which samples are analyzed, and different projectiles interact differently with the surface. [124] This chapter focuses on the study of the behavior of a metal-organic sample under bombardment by monoatomic and small polyatomic projectiles: Ga, Au, Au_3 and C_{60}.

The first Section is dedicated to the study of metal-coated surfaces. The Section is divided into different topics. It starts from a brief description of the computational method, and the choice of aiming points on the gold coated sample. This is followed by the results and discussion. The total ejected yield is compared in different manners, the analysis of the spectra is done. A detailed discussion of the mechanism of ejection for all projectiles (impacts on NP vs impacts on PE), and implications of the roughness of the surface are also presented. The second Section, 4.2, is related to the study of the metal-organic interface of the respective bulks; similar studies are done in that part. Finally, in Section 4.3 the mechanism of crater formation for different targets is discussed.

4.1 Study of the gold coated surfaces

If a surface is coated with a uniform overlayer or nano-islets, the physics of the mechanism of ejection may drastically change depending on the ratio of the densities of the overlayer-substrate compound. For instance, for a thin water ice condensed onto a Ag substrate bombarded by Au, Au_2, Au_3 and C_{60}, [125] the mechanism shows that the overlayer is swept away, providing an easy escape route for the substrate fragments. This differs from the mechanism in which the ejected sub-

strate fragments have to travel through the overlayer having a series of collisions to be finally desorbed. In this kind of systems, the substrate intensity is expected to decay exponentially as the overlayer thickness increases. [126, 125]

In contrast, when the substrate is soft and the overlayer is formed of a metal, the situation becomes totally different. In this case, many factors play a role for the mechanism of the substrate desorption. First, the metal usually never forms a uniform layer on the surface. Due to the randomization introduced in the deposition process, differences in the adhesion between metal and organics and cohesion between metal atoms, they are grouped on the surface forming islets or cluster-NPs that may vary in form and size (see in Chapter 3). Depending on the diffusion process, they can be also on the surface or buried. [127] Second, the emission yield depends on whether impacts are on NPs or over the interstitials spaces between them. Third, if impact is on a NP, the nature of the projectile has an important role in the manner as the projectile interacts with the NP, and hence differences on the mechanism of ejection. Monoatomic projectiles can either fragment the target NPs, or channel into them; while, polyatomic ones produce compression and disintegration of the NP as it will be shown in this section. All those facts make that in the metal coated substrate, the intensity of the substrate signal vs overlayer thickness follows some distribution (see in Figure 1.1a) rather than an exponential decrease.

4.1.1 Details of the simulations

A box with dimensions of $30 \times 13 \times 25$ nm^3 with 2400 molecules of PE with 200 elements each, was covered with a non-uniform layer of 13386 gold atoms using the random deposition algorithm. The total number of particles in this box is 493386. The system was relaxed using the MD SPUT code as it was explained in Section (3.3). Rigid boundaries of 5 Å and stochastic forces of 15 Å at 4K were used to provide a heat bath and allow sample equilibration. For all the bombardment simulations, the rigid boundaries and a layer with stochastic forces (Langevin equation) mentioned above were used to damp the pressure waves generated in the sample.

The semi-empirical potentials used to describe the forces between particles are: AIREBO potential (2.44) for the *C*-*C* interactions in C_{60} projectile the MD /MC-CEM potential for *Au*-*Au* interactions (2.37). The potentials for PE entities in the frame of the CG approximation were already given in Section 3.2.1 on page 44, and for *Au*-C interactions on page 50. The Molière form (2.46) was used for the *Ga*-PE and *Ga*-

Au interactions. The LJ potential (2.27) was also used to describe the Au-C interactions, with ϵ and r_e parameters equal to 0.00277 eV and 3.561 Å respectively. For Au-CH_2 and Au-CH_3, it was used the same ϵ and r_e equals to 0.012 eV and 3.41 Å in both cases. It is important to remember that at short range (high energy interactions), the potentials must be entirely repulsive ones of the form (2.46); therefore Molière was also used for the short range interactions of the C_{60}, Au_3 and Au projectiles with Au, CH_2 and CH_3.

All projectiles C_{60}, Au_3, Au and Ga were aimed at the sample surface with normal incidence and 10 keV of kinetic energy. Figure 4.1 shows the relaxed gold-coated structure, and the 3×3 matrix with thirty six aiming points. In this system the central Au-NP has a particular importance because it is in the sampled impact zone. It is a quasi-spherical NP (Au_{555}) with an approximated diameter of ~ 2.5 nm.

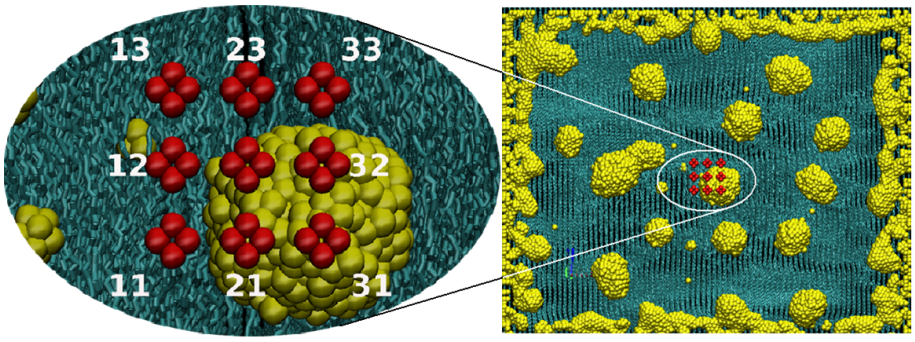

Figure 4.1: Relaxed gold-coated PE surface and the amplification of the nine impact points with distance separation of 1 nm. For monoatomic projectiles three additional aiming points have been defined, separated 0.2 nm in x and y directions for statistical reasons.

For the polyatomic projectiles only one impact per matrix point was done. In the case of the monoatomic ones, three additional impacts were done around each matrix point to obtain a better statistics of the corresponding zone. The physical information obtained was averaged over the four impacts of the corresponding matrix point. The distance between the nine series of matrix points was set to 1.0 nm in each of x and y directions. And for each of the series, the distance between the aiming points was set to 0.2 nm in the x and y directions.

4.1.2 Sputtering yields

One of the best ways to see how Au-NPs alter the surface behavior is to calculate the total sputtered mass, and the total number of frag-

ments per impact. In this manner the fragmentation can be compared to the total mass ejected for each projectile. Those measurements are summarized in the histograms of Figure 4.2. They are taken at the end of the simulations, after 30 ps, when most of the PE fragments have been ejected.

In the graphs of Figure 4.2 the data with the information of each projectile, are separated in three different sets of bars. The first set, corresponds to the total number of sputtered fragments (top graphic) and total sputtered mass (bottom graphic), for impacts on PE. The second set is for impacts on the Au-NP. In both sets, each bar is averaged over its corresponding total number of impact points, as it is shown in Figure 4.1. The matrix points 21, 22, 31 and 32 correspond to direct impact on the Au-NP, while the rest is over PE. Then, the total number of impacts with Ga and Au is 16 on the Au-NP and 20 on PE, while for C_{60} and Au_3 is 4 impacts on the Au-NP and 5 on PE. The third set is the average for each projectile over all impacts (graphs of all the impact points are given in Figure B.3 in the appendix B).

From the plots, C_{60} shows the highest number of sputtered fragments with the smallest fluctuations when impacts are on PE. In this case, the average of the sputter yield is around 330 fragments, which is ~ 4 times higher than the average of Ga. In contrast, the plots show for C_{60} impacts over the Au-NP a significant sputter yield reduction, and large fluctuations which depend on the exact impact point on the Au-NP. Those large fluctuations can be explained because the thickness of gold changes when the impact points are moved from borders to the center of the spherical Au-NP. This produces large differences in the total sputter yield, and hence large fluctuations. For instance, the total sputter yield of the impacts on the border (21 and 22), and close to the center (31 and 32) have a difference of one order of magnitude. Additionally, a comparison of the C_{60} histograms of the first and third sets, shows that the number of fragments per impact reduces from 330 to 230 and the fluctuations increases. This is due to the abrupt change in the target density from PE to the Au-NP. The poor production of yield by C_{60} in the MetA-SIMS configuration has been experimentally observed. [23, 128]

When Ga is used as a projectile, the situation is very different. First, large fluctuations are observed depending on the exact impact point of the projectile with respect to the position of the surface atoms. If the impact is over PE, the projectile can either deposit its energy in the surface layers and induce high yields or channel inside the sample and produce virtually no yield. This well known behavior [53] explains why the data are very spread for Ga, in each series of 4 impacts. When the impact point is over the Au_{555} NP, the obtained results indicate an

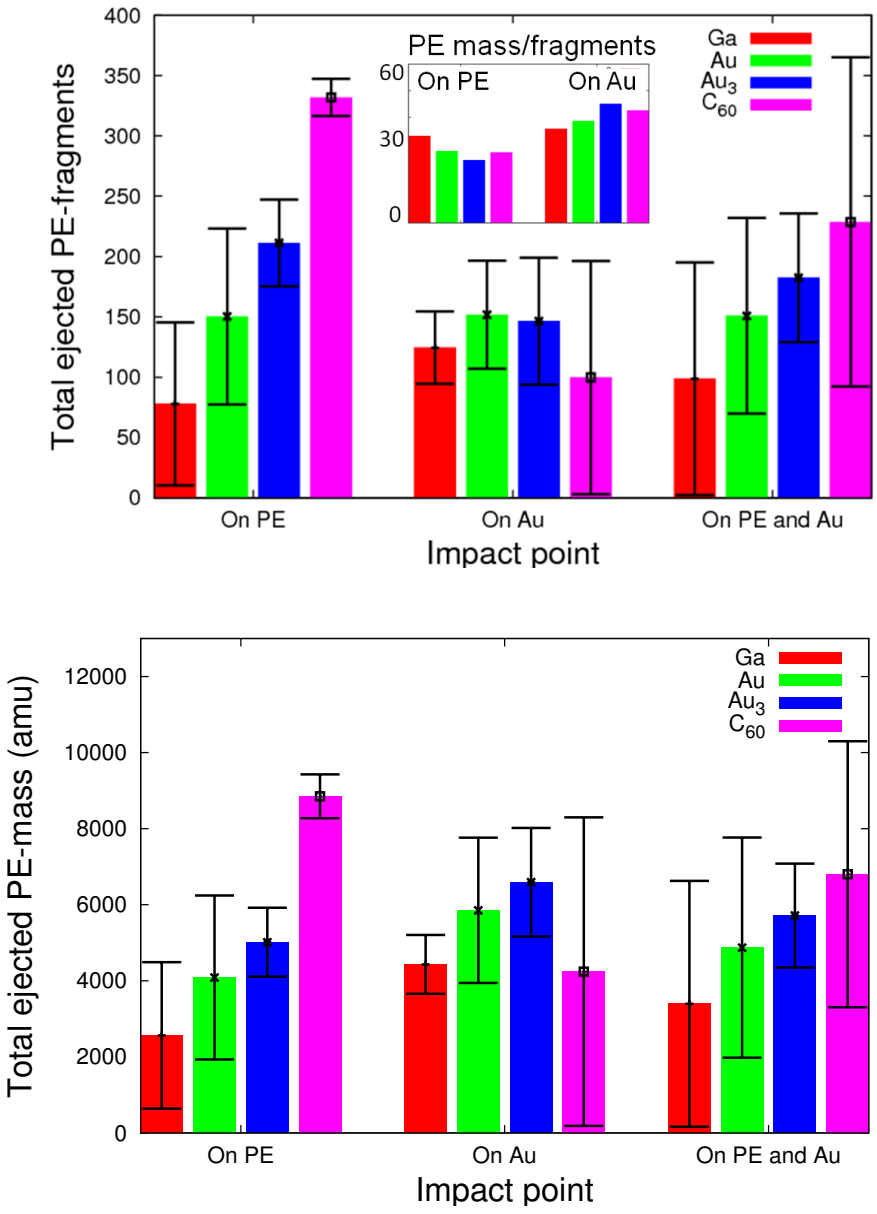

Figure 4.2: Histograms of the total emission of PE fragments (top) and mass (bottom) per impact for each projectile. Data are separated in three sets: impacts on the interstitial points between *Au*-NPs, direct impacts on the *Au*-NP, and average over all impacts and independently of aiming point. The small inset is the ratio mass/fragments.

increase of the average of the PE yield by a factor of almost ∼2. This sputtering yield enhancement is consistent with the observed effects in the MetA-SIMS experiments. [5, 11, 128]

The large fluctuations of the sputter yield of Ga and small fluctuations of C_{60}, when they impact on PE, are also in agreement with previous MD results for organic samples obtained by the Postawa and Garrison groups. [53]

Histograms of the Au and Au_3 projectiles show similar results (see in Figure 4.2). In almost all sets, the averages of the total sputter yield of Au_3 are larger than those corresponding to Au. In addition, in all the histograms the bars share the same interval of error. Both projectiles show large fluctuations for all impacts. The large fluctuations of Au and Au_3 are mainly due to two factors, first, the abrupt change produced by changing the impact point from the center to the periphery of the Au-NP. Second, the channeling effect that may occur with monoatomic projectiles. The latter is mainly in the case of Au. The channeling may also happen to the atoms of Au_3 because the projectile disintegrates, and the individual atoms behave like monoatomic projectiles. The results for Au and Au_3 impacts on PE, show some disagreement with experimental results on organic materials. Experimentally, for the ratio of the sputter yields, (Au_3/Au), a difference of one to two orders of magnitude depending on the ion peak chosen is observed. [129] The large difference of Au and Au_3 fluctuations observed in Figure 4.2 does not explain the disagreement. Nevertheless, the yield of MD is formed by neutral fragments, ionization is not considered.

The higher efficiency of C_{60} compared to Au_3 in pristine samples is well known and it was experimentally demonstrated by Boussofiane-Baudin *et al.* [130] Even, it is also corroborated using MD simulations in materials like Ag and water. [131, 132, 133, 134] The results of impacts on PE are in agreement with these works. However, when the sample is coated the situation is different. A comparison of the average of the total ejected PE produced by C_{60} and Au_3 in Figure 4.2, shows that yield of C_{60} over all point is higher than the sputtering yield of Au_3, although Au_3 has less fluctuations. Nevertheless, if the thickness of gold was increased, C_{60} would be inefficient to produce PE sputter yield and Au_3 could be a better option.

The small inset of the top of Figure 4.2 shows the ratio of total mass per ejected fragments. The inset shows that when the impacts are on the Au-NP there is either an increase of total sputtered PE masses, or a reduction of PE sputtered fragments. This difference between direct events on the Au-NP and on PE will be explained below, in the Section on the mechanisms of the ejection.

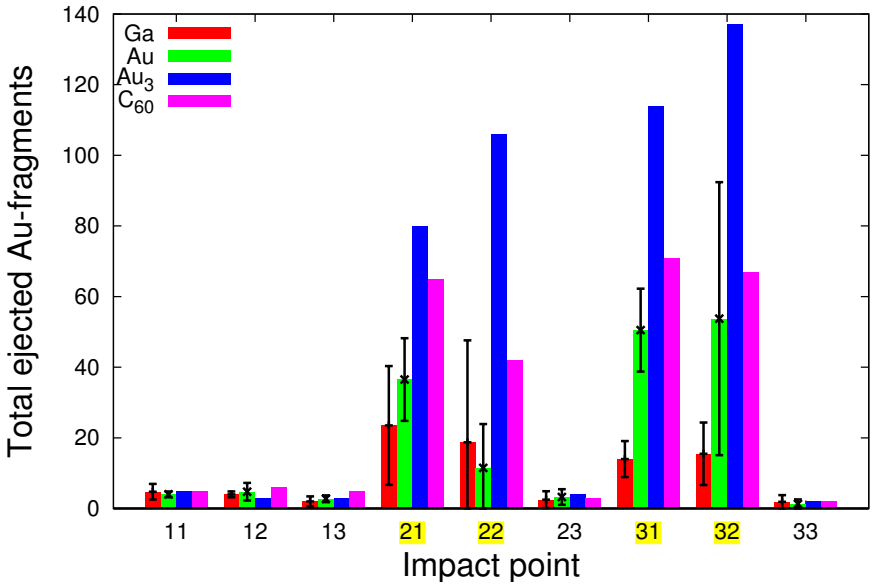

Figure 4.3: Histograms with total ejected Au-fragments for each impact point.

The total gold emission is also analyzed (see in Figure 4.3). In this case, only the results of the total number of sputtered gold fragments are given. In contrast to the analysis of the desorption of PE, the analysis of the desorption of gold fragments for each impact point of the matrix 4.1 is done separately. The reason is that the quantity of sputter yields strongly changes from one point to the other. It is especially evident for impacts over the *Au*-NP. When impacts are on *Au*-NP, the contribution to the gold desorption comes from two sources: fragments of the impacted *Au*-NP and entire *Au*-NPs that lift up. The NP fragmentation explains the large differences observed between the impact point on *Au*-NPs and over PE in Figure 4.3. The total mass per impact is not reported because of the big differences introduced when entire *Au*-NPs are ejected, which makes it difficult to observe the fragments from the target *Au*-NP.

From the data of histograms of Figure 4.3, the average values of total numbers of sputtered fragments of gold over the four matrix points which correspond to the impacts on *Au*-NP, are 20, 38, 109 and 45 fragments per impact for *Ga*, *Au*, Au_3 and C_{60} respectively. On average, Au_3 produces around three times more fragmentation than any other used projectile. On the other hand, in Figure 4.3 it is observed that C_{60} produces almost the same number of sputtered fragments when the impact point is moved over the *Au*-NP. This can be explained because

C_{60} transfers its energy to the first atoms of the Au-NP. The desorption of Au fragments produced by C_{60} is higher than the one produced by monatomic projectiles, but the total mass is less because the emission is almost composed of monoatomic fragments.

4.1.3 Analysis of the mass spectra

As it was previously said, molecular fragmentation constitutes the heart of the SIMS spectra. The study of the sputter yields in the figures 4.2 and 4.3, has shown a strong dependence on the impact point and on the used projectile. In addition, when the impacts are over the Au-NP there is either an increase of the ejected masses or a reduction of the number of fragments, or both. So, how can those facts change the spectrum shape? From the experimental viewpoint this question is important due to the fact that spectra would change depending on the projectile or ionization technique used. The answer is given by the direct analysis of the spectra.

The mass spectra of PE and gold, are calculated for all the impacts done with MD simulations (see in Figure 4.4). C_{60} and Ga spectra are also compared to the experimental data (bottom graphics). Each plot is normalized to its maximum value. Those maximums are given inside of the parentheses of each graph.

An interesting calculation in Figure 4.4a, is to draw the trend lines of spectra only considering the elements with values of mass less than 100 Da for PE. In this case, the difference in the trend lines of the spectra for the four projectiles is given only by a multiplicative factor, where C_{60} gives the highest and Ga the smallest. Moreover, the results show that the intensity in this interval decreases at a rate proportional to its value in an exponential decay. In other words, the intensity is proportional to $exp(-a \times mass)$ where "a" is given by 0.052 with a difference of more of less 3% between the projectile curves. It should be noted that the intensity decreases almost by two orders of magnitude in this mass interval, or in other words, the logarithm linearity is held in the range of two orders of magnitude (with a square value R^2 of more than 0.98 in all curves). This trend line from the simulations (dashed line in Figure 4.4a), is in good agreement with the corresponding ones of the experimental data for Ga and C_{60} (Figure 4.4c).

The mass spectra obtained for Au emission using MD, are in Figure 4.4b. Those spectra are formed from the contributions of the Au-NP fragments. From those pictures, it can be said only that the intensity of gold decreases exponentially with mass below 1000 Da. That is corroborated in the picture 4.4d for the experimental data.

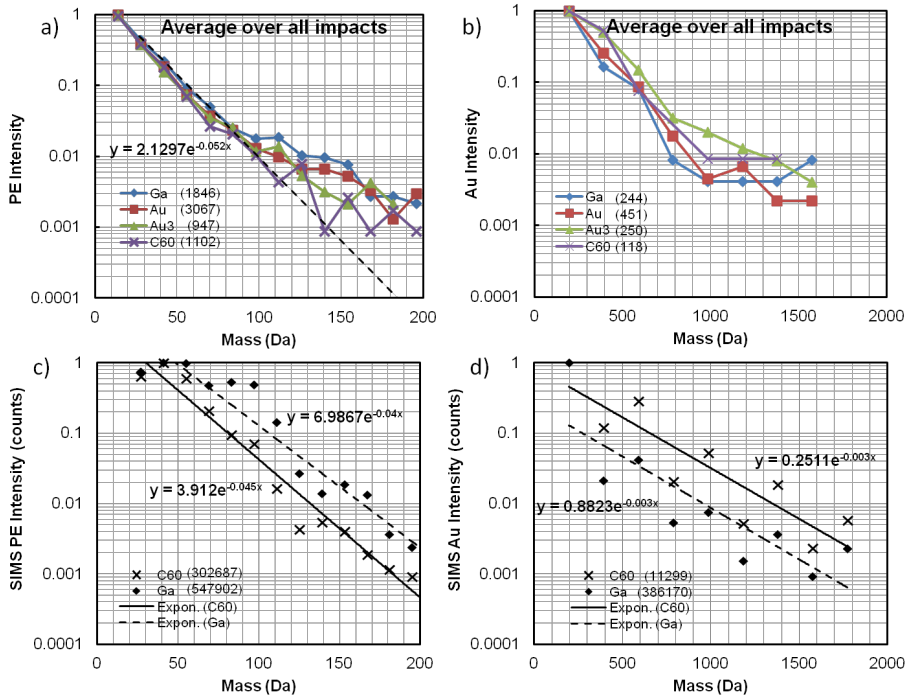

Figure 4.4: Comparison of the mass spectra. On top, MD simulations for Ga, C_{60}, Au, and Au_3. On bottom, experimental data for Ga and C_{60}. In parenthesis, the corresponding normalization values. The left column is the PE intensity counts while right is Au intensity.

Another manner to analyze the data of mass spectra is to separate the impacts on Au-NPs from the impacts over PE. These results are drawn in Figure 4.5. Impacts on the Au-NP show approximately the same trend line, which can be considered as an indication that the fragmentation of PE chains depends more on the direct gold NP fragmentation and interaction with these fragments of gold.

A second analysis of the data from Figure 4.5 is done in Figure 4.6. The difference is that the results of each projectile are plotted separately. In each of the four graphs, impacts on the Au-NP and on PE are compared. Trend lines of the mass spectra of the C_{60} and Au_3 show higher slopes for impacts on the Au-NP, but the slopes of Ga and Au are similar.

The previous mass spectra of PE from pictures 4.4 to 4.6, only represent one part of the total sputter yield. The interval of mass is up to 200 Da, because the noise becomes dominant after this value. The sum of the data excluded after 200 Da, is less than 18% for Ga, Au, and

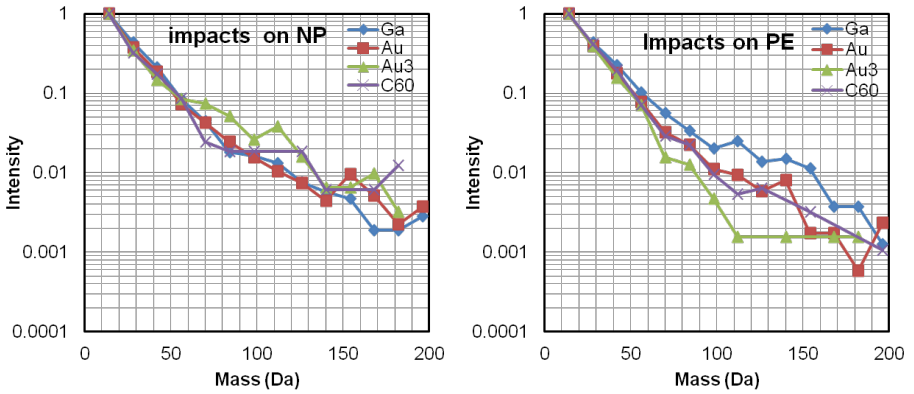

Figure 4.5: Normalized intensity or number of PE fragments as a function of mass for impacts on the *Au*-NP (left) and impacts on PE (right).

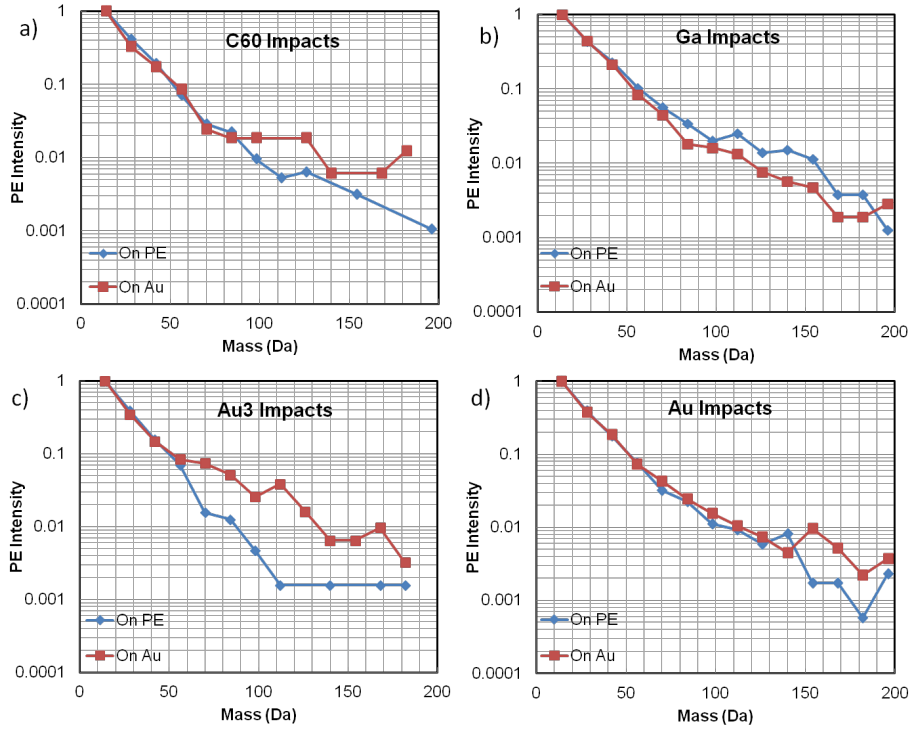

Figure 4.6: Data separation depending whether the impacts are on PE or on the *Au*-NP for each projectile.

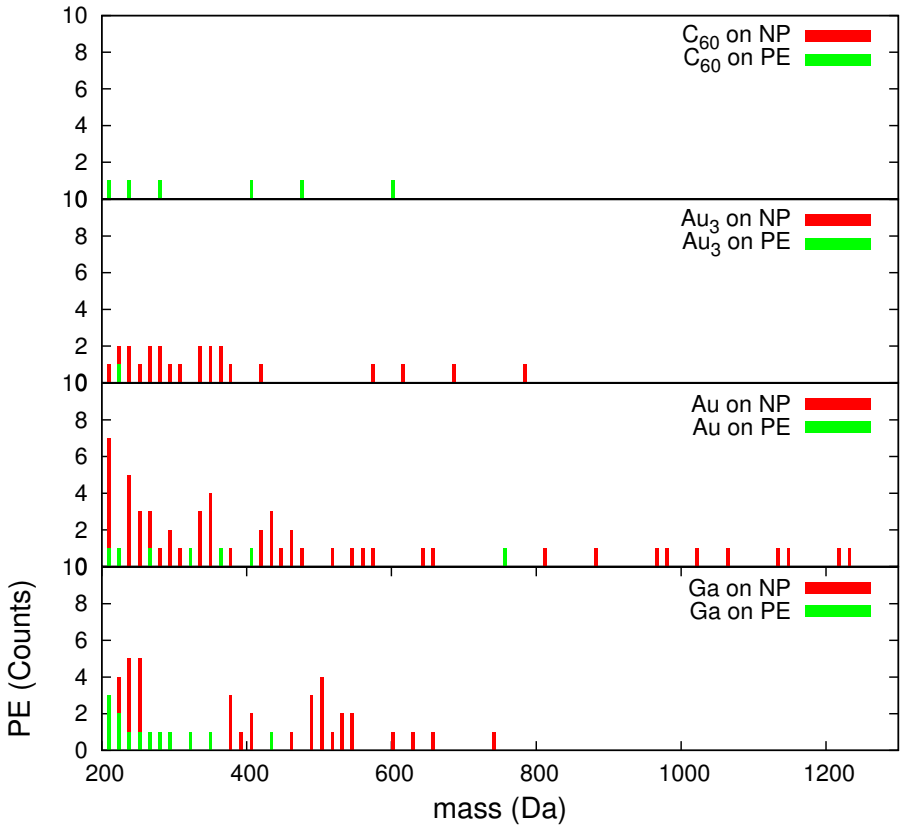

Figure 4.7: Mass spectra of the PE fragments with mass larger than 200 Da. Each graph shows a comparison of the impacts on NP and on PE, for C_{60}, Au_3, Au and Ga, respectively. This part of spectra contains ∼30% of the total mass for impacts on NP, and ∼10% for impacts on PE.

Au_3, and less than 6% for C_{60}. Moreover, for impacts on PE, more than ∼90% of the data is located before 200 Da, while for impacts on NP, it only represents ∼70% of the total, except for C_{60}, which is ∼89%. The mass spectra of the PE fragments with mass larger than 200 Da is shown in Figure 4.7. In those plots, a superposition of the PE fragments when impacts are on PE and on the Au-NP is shown. It is observed that in general, impacts on the Au-NP tend to produce larger PE fragments.

4.1.4 Origin of the fragments and emission depth

The thickness of the surface layer from which most of the sputter yield comes is known as *emission depth*. [135] For flat organic surfaces, the emission depth of sputter fragments is considered to be of the order of 10 Å. [126] Although this estimation is somewhat arbitrary, it gives a first approximation of the origin of emitted particles and emission depth. Moreover, it is known that the signal intensities exhibit an exponential decay as a function of thickness d of the coating overlayers (ultra-thin polymer layers on metal substrates, see Chapter 7 of the ref [16]). However, metal NPs alter the surface properties, meaning that the mechanics of ejection and emission depth do not only depend on the initial projectile energy, sample and projectile nature, but also on the presence of NPs and on their particular arrangement on the surface. For instance, these NPs represent an obstacle in the emission of either large fragments or entire molecules of PE. Moreover, if the projectile first hits them, part of the energy is used for the NP fragmentation.

Figure 4.8 shows the origin of the emitted fragments, for both PE and Au. It also gives an indication of how the energy is distributed into the surface. This Figure summarizes the differences between the four projectiles. The color coding used is, blue for PE and yellow for gold; the central NP is colored in orange if the impact is over it, else yellow is kept. Green and purple represent the origin of the Au and PE atoms ejected after 30 ps. Projectiles are in red, and the PE chains displaced to the surface to form the crater are in pink. The inset pictures inside of every snapshot provide a lateral view of the same impact.

The frames of the impacts on PE show that the origin of sputtered PE is quite arbitrary in its volume and shape (see purple atoms), and it depends on the exact mechanism and how the bonds are broken in PE. Additionally, from the inset figures it is observed that the emission depths for impacts with Au_3, Ga and Au are of the same order of magnitude. C_{60} shows a lower emission depth when it is compared to the others. It produces a quasi-spherical emission region, and the emission depth is of the same order as the radius of the crater.

In the case of the impacts on the Au-NP, the emission depth of C_{60} is particularly interesting. Figure 4.8 shows that the emission depth with C_{60} impact only involves the atoms of the first PE layer, which are removed. The other three projectiles show spread and chaotic distribution of the origin of the PE fragments. In general, the origin of the sputtered PE is highly depending of the exact Au-NP fragmentation. These distributions are characteristic of the stochastic nature of collisions cascades.

The analysis of those frames suggests that in general impacts on the

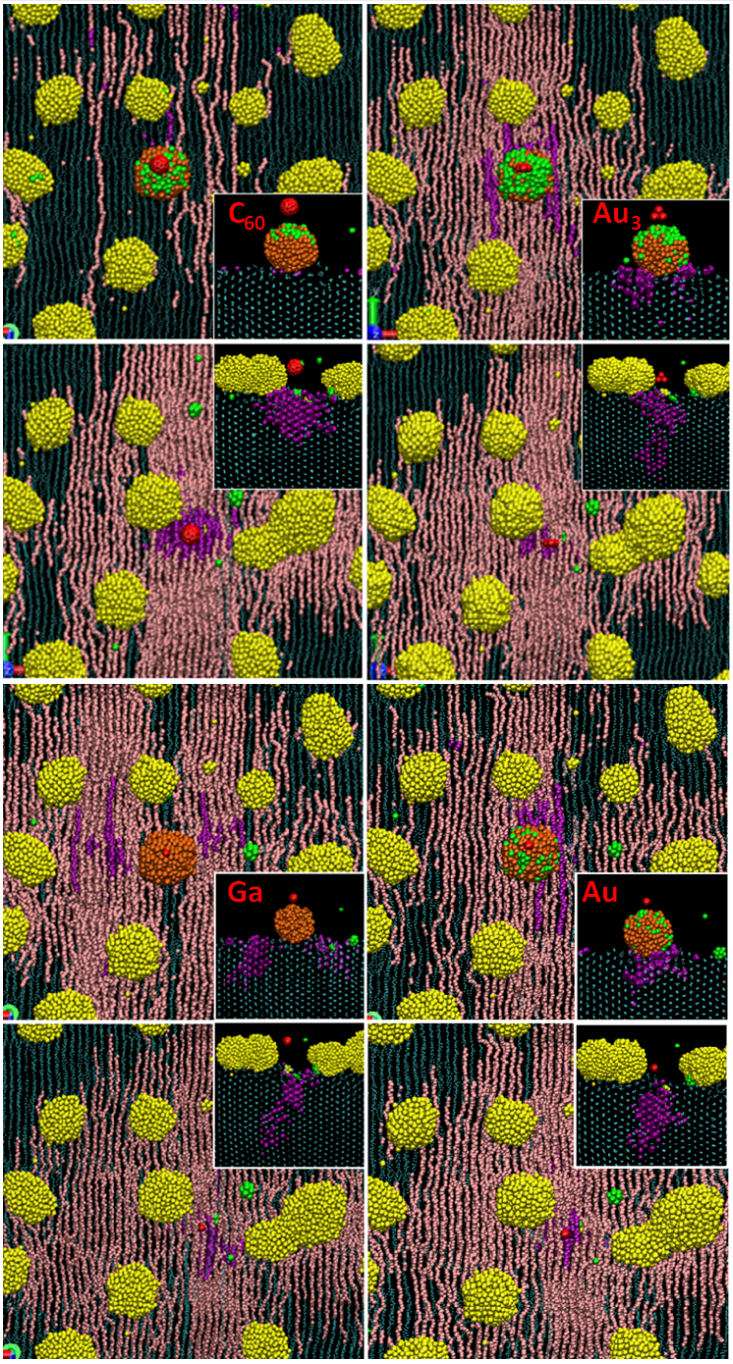

Figure 4.8: Snapshots of the surface illustrating the origin of the yield produced by C_{60}, Au_3, Ga and Au at $t = 0$. Inset frames are the corresponding side views. Color coding: blue is PE, yellow is gold, the central NP is orange if the impact is on it, else yellow is kept. Green and violet are Au and PE atoms which are going to be ejected at $t = 30$ ps. Projectiles are in red, and pink are the PE chains displaced to the surface to form the crater rim.

Au-NP increase the stopping power, because the origin regions of PE fragments are shallower and wider than for impacts on PE. It is important to note that the emission depth is lower than the ranges reached by Au, Au_3, Ga projectiles, but comparable in case of C_{60}.

4.1.5 Fragments size: impacts on PE vs impacts on *Au*-NP

From the mass spectral comparisons of impacts on PE and on the *Au*-NP in Figure 4.6, and Figure 4.7, it seems that impacts on the *Au*-NP create larger sputtered PE fragments. This difference is also observed in the frames in Figure 4.8 - as it is represented by the origin of PE fragments (see purple atoms). This fact could be explained first, because the targeted *Au*-NP can produce tensions over the PE chains, which can break them by the weakest bonds. Some of these bonds can be far from the impact point. Second, depending on the energy of the impact, a cascade effect can start into the targeted *Au*-NP, producing multiple recoil Au atoms, which spread in a larger area over PE, and implant inside. Those Au atoms are also able to break bonds which are far from the impact point. Those two factors can create the conditions for the subsequent ejection of larger PE fragments.

4.1.6 Mechanistic analysis of impacts on the *Au*-NP

An additional comparison of the impacts at 1 ps and 30 ps, is given in the snapshots of Figure 4.9. It shows the process of *Au*-NP fragmentation, as well as the projectile implantation into the PE.

For C_{60}, it is observed that the crater is very small and only the first layers of PE are affected with a few chains broken. The ejection is mainly composed of *Au*-NP fragments. The major quality of C_{60} is to transfer its energy into the top surface, but when the impacts are over the *Au*-NPs it turns to a weakness in terms of polymer emission. This is observed in Figure 4.9 in which the top Au atoms of the target *Au*-NP are removed. Consequently, due to the pressure of the *Au*-NP over the chains, a few PE fragments are ejected. Additionally, small *Au*-fragments are implanted into PE.

In the case of Au_3, the *Au*-NP is completely destroyed, and many Au fragments are implanted into the PE. The crater is not uniform and it shows two not well defined regions. The crater edges are formed with the material that lifts up from the surface (pink colored atoms). Among the four projectiles, Au_3 produces more fragmentation of the *Au*-NP and gold implantation on PE.

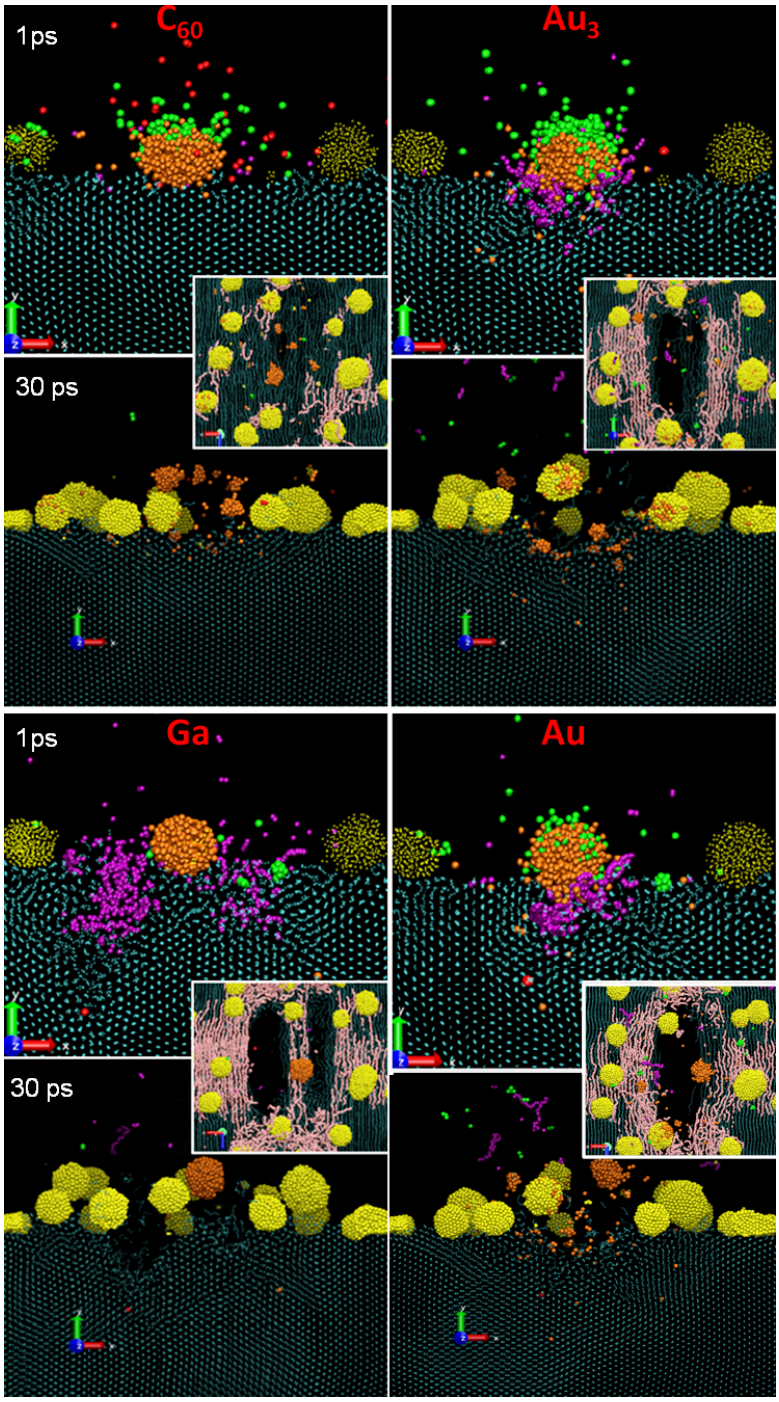

Figure 4.9: Comparison of the craters for C_{60}, Au_3, Ga and Au at 1 ps and 30 ps. Inset frames show the top view of the craters at 30 ps. In frames at 1 ps, Au_n NPs have been attenuated to emphasize the projectile effects over the central NP. Same color coding as in Figure 4.8.

In contrast to the cluster projectiles, the monoatomic projectiles sometimes do not destroy the targeted *Au*-NP, they rather go through it. This is the case shown for *Ga* in Figure 4.9. In this specific event, one atom was removed from the *Au*-NP and implanted into PE. This atom produced a second cascade in the PE. At the end of the trajectory, the targeted *Au*-NP remained almost intact.

In the case of the *Au* projectile, it has a larger interaction range than *Ga* and lower velocity, then channeling is less probable. It produces a more homogeneous *Au*-NP fragmentation. Differently to C_{60} and Au_3, the origin of *Au* emission by Au_3 impact is more distributed in the whole *Au*-NP. For C_{60}, the sputtering comes mainly from the NP surface (see green atoms).

Another interesting phenomenon related to the fragmentation of the *Au*-NP is that not all the gold fragments are ejected or implanted into the PE. Some of these gold fragments can move laterally and collide with the neighbor NPs. They can also aggregate to the other NPs to form more massive NPs (see orange atoms in bottom frames of 4.9). In addition, in all cases it is observed that the nearest neighbor NPs are ejected. This is because of momentum transferred by the chains moving at the surface and by the recoil *Au* atoms produced at the moment of the crater formation.

4.1.7 Comparison to results obtained on gold coated amorphous PE

It is also interesting to compare the previous results with the results obtained on gold coated amorphous PE, which were obtained by Van Hoecke for his master thesis. [136] To have a better match of the gold overlayer microstructure of the crystalline and amorphous samples, the *Au*-NPs of the crystal sample (sample A) were simply transferred to the amorphous sample. These NPs were placed close to the surface with initial velocity of 0.05 Å/fs. Then the system was evolved using MD for 750 fs. Next, the system was restarted with velocities reset to zero and relaxed. Finally, it was bombarded over the center of the Au_{555} NP, at the interface, and over PE with an initial energy of 10 keV.

The ejected masses of those simulations are compared in Table 4.1. The sputter yield for C_{60} as a function of the impacts on NP, interface and on PE, follows the same trend despite the large differences of absolute sputtering yield between the two targets. That is, the *Au* yield increases when the impact moves from PE to the center of *Au*-NP, while the PE yield decreases. In contrast, the averages of the sputter yield of PE produced by *Ga* impacts have an opposite behavior to C_{60}. The large

C_{60} impact	On NP	Interface	On PE
Coated crystal PE			
PE	0.5	7.0	9.9
Au	19.7	15.3	5.1
Coated amorph. PE			
PE	6.02	25.89	52.55
Au	26.2	12.61	0.0
Ga impact	On NP	Interface	On PE
Coated crystal PE			
PE	4.94± 3.00	4.87± 4.75	1.22±2.00
Au	4.67± 1.68	6.74± 7.26	2.16±1.48
Coated amorph. PE			
PE	27.45±16.47	41.53± 49.85	7.01± 13.46
Au	24.46±44.17	23.12± 32.36	0.0 ± 0.0

Table 4.1: Comparison of the results on gold coated amorphous PE and PE crystal. Mass of gold and PE (kDa) sputtered from sample upon 10 keV, *Ga* and C_{60} bombardment. The results from amorphous sample are taken from the master thesis of Van Hoecke. [136]

difference of the sputter yield of PE between the two samples is due to the fact that in the crystal the ends of the chains are tied. In the amorphous case, the emission of entire molecules (1.4 kDa) is allowed, in the crystal only fragments are obtained.

4.2 Study of the metal-organic interface

Until now, only the gold coated surface has been studied. Another interesting case of study concerns the bombardment of a box that includes a planar vertical interface between two bulk regions of PE and gold. This metal-organic sample may represent for example a large NP or a nanowire in a polymer matrix. This sample offers an abrupt change of the properties of the target at the interface. The step change of density, cohesive energy, atomic masses, etc, may create an unexpected or unusual behavior of the emission and crater formation around the interface. Therefore, it is bombarded and the results analyzed and compared to the gold coated system.

This "*sample B*" with vertical interface between PE and *Au* is a box of $30 \times 15 \times 25$ nm^3 containing a total of 591550 CG elements (CH_2, CH_3 and *Au*), among which 227550 *Au* atoms. The relaxed structure of the *Au* slab is fcc with a lattice parameter of 0.408 nm. One third

of the sample volume is occupied by gold and two thirds by PE, i.e., the Au-NP interface is located at 10 nm from the edge on the Au side. Indeed, a larger volume of PE is needed to contain the sputtering event and prevent the reflection of pressure waves from edges. Five series of impact points were chosen: at the interface and at 1 nm and 3 nm of the interface towards the PE and the Au sides. Again, 4 impacts were computed with Ga and Au in each zone to obtain better statistics and only one impact per zone for C_{60} and Au_3 (see inset picture with the impact points in Figure 4.14b). For the simulations performed with sample B, a total trajectory time of 25 ps was sufficient to gather all the sputtered particles.

For all the bombardment simulations, rigid boundaries of 0.5 nm and a layer with stochastic forces of 1.5 nm using the Langevin equation (2.22) implementation were used to damp the pressure waves generated in the sample.

4.2.1 Sputtering yield of the metal-organic interface

The results presented in this section correspond to the series of impacts at the metal-organic interface and points close to it, which were previously described. In a similar manner as it is done for impacts on metal coated surfaces, the total sputtered mass and yield are gathered and plotted as histograms. The results of total sputtered mass produced by Ga, Au, Au_3 and C_{60} bombardments at 10 keV, are given in the graphs 4.10 and 4.11.

At 3 nm from the interface on the PE side, the behavior of all projectiles is not significantly different when compared to results shown in 4.2 for impacts on PE in sample A. In contrast, the impacts at 3 nm from the interface on the gold side, and for all the projectiles, show almost the same behavior as for a simple bulk system of gold. That is, no significant border effects are observed on the PE side and neither PE ejection. Moreover, an additional comparison of the histograms, shows that Au_3 sputters tree times more gold mass than the other tree projectiles.

In Figure 4.10 the histograms of the impacts at 1 nm and 3 nm from the interface on the PE side, show similar sputtered masses of PE with C_{60}, but yields of the other projectiles are difficult to analyze due to the large fluctuations. Impacts on the interface produce almost the same emission of PE than impacts on the PE side. However, impacts at 1 nm inside of gold, show a reduction of more than one order of magnitude of the ejected PE mass. For the emission of gold, impacts at 1 nm of the interface on the gold side offer the most interesting case. In this case, the sputtered gold mass is maximum for each of the projectiles (see in

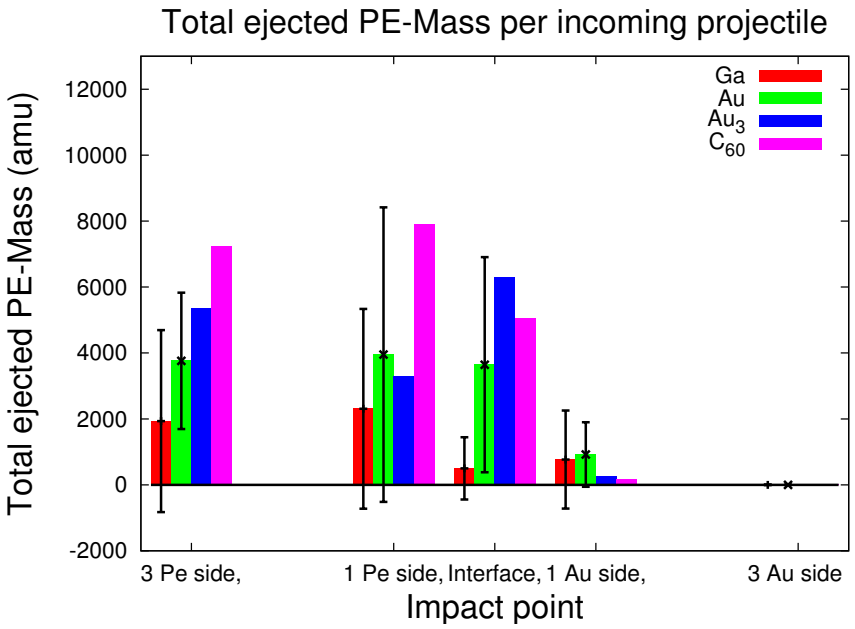

Figure 4.10: Histograms of the total ejected PE mass for impacts at the *Au*-NP interface, and 1 nm, 3 nm away from the interface.

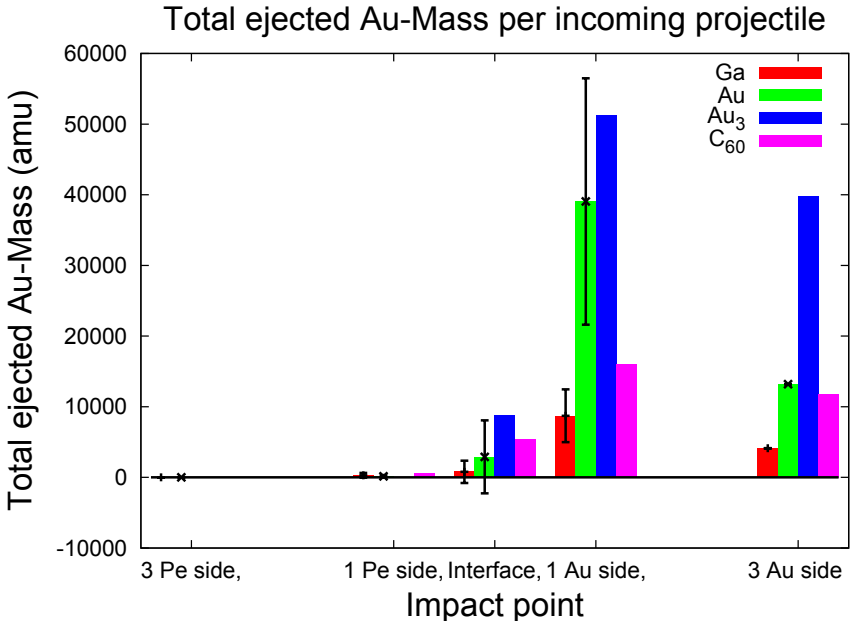

Figure 4.11: Histograms of the total ejected gold mass for impacts at the *Au*-NP interface, and 1 nm, 3 nm away from the interface.

Figure 4.11). Additionally, among the four projectiles, at each impact point on the gold side, Au_3 always produces the maximum gold mass desorption.

In general, impacts at 3 nm of the interface do not produce any significant effect over the other material, the behavior is almost the same as for a simple bulk sample. However, impacts at 1 nm on the gold side, and on the interface, induce the sputtering of both materials.

4.2.2 Mechanism of ejection of sample B

In the snapshots of Figure 4.12, the mechanisms of emission for impacts at 1 nm from the interface (gold side) for C_{60} and Ga are shown, respectively. Color coding is the same as in Figure 4.9, but here the atoms highlighted in orange represent the atoms that move to the surface to form the edge of the crater. When Ga impacts at $\sim$1 nm from the interface, in the Au zone, there may be sputtered PE fragments or not depending on the manner in which the border of the gold bulk fragments. In Figure 4.12b Ga implants in the gold and the emission of PE

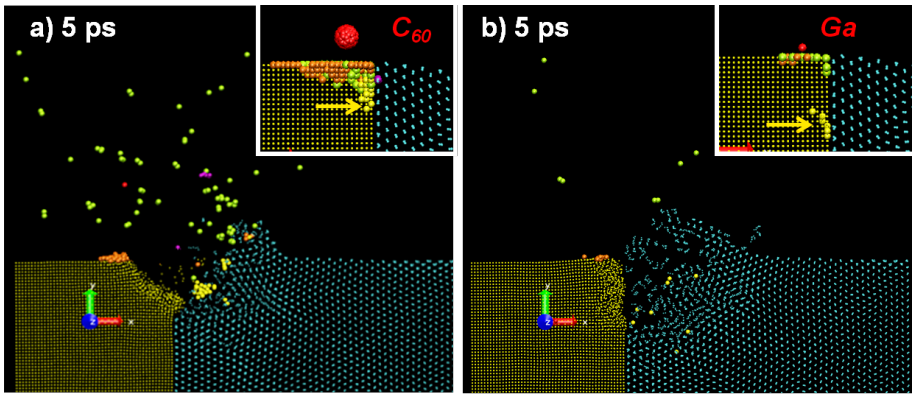

Figure 4.12: Snapshots of 10 keV impacts at 1nm from the interface on Au side for a) C_{60} and b) Ga for the *sample B*. Color coding: the same as in Figure 4.9, but orange are now the Au atoms moving to form the rim on surface and highlighted yellow the Au atoms implanted into PE (see the arrows).

is mainly due to the recoil atoms of gold which penetrate in the organic material. This is shown by yellow arrows which point to the highlighted atoms in the same color. These gold atoms break bonds and transfer their energy to the organic fragments. For C_{60} bombardment at 1 nm on the Au side (Figure 4.12a), some Au atoms also implant in the PE side. They are responsible for the sputtering of PE.

Additionally, in picture 4.13 is shown a second example of the direct

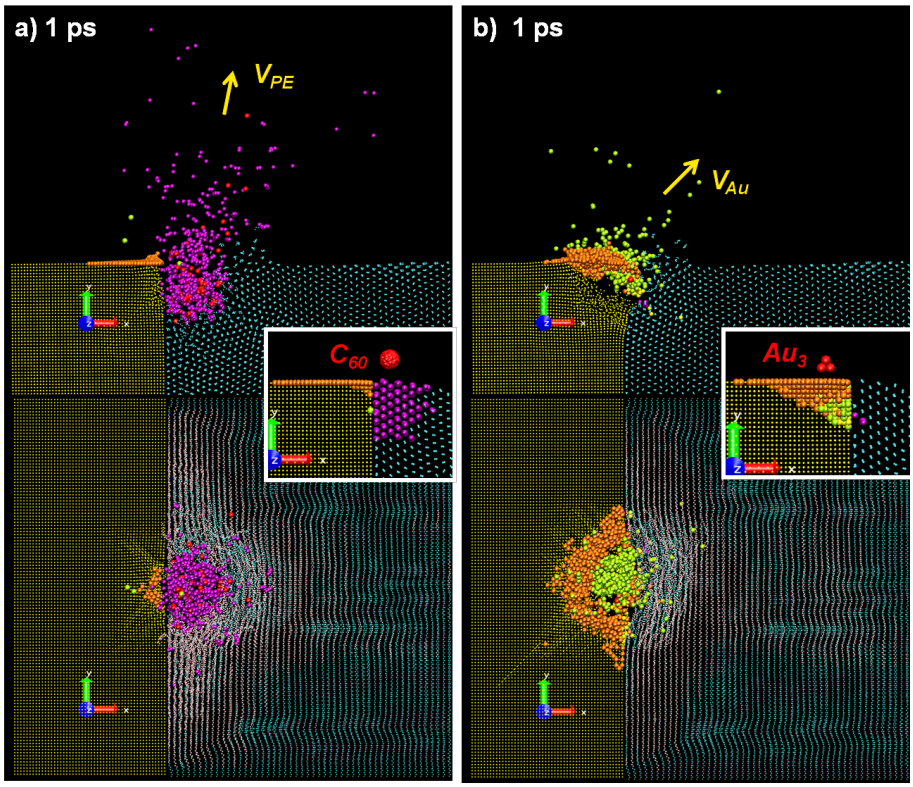

Figure 4.13: Impacts of C_{60} on PE (a) and Au_3 on gold (b), both at 1 nm of the interface. On top, side view, and on bottom, top view of the crater and sputtering mechanism at 1ps. Small insets are the side views at time zero showing the origin of sputtered PE. Color coding: the same as in Figures 4.9 and 4.12.

impacts of C_{60} over PE and Au_3 over gold. In the frames, it is observed the material that lifts up and of the crater formation at 1 ps, at 1 nm from the interface. On the top are given the side views, while in the bottom are given the top views of both impacts. In the small insets is indicated the origin of the ejected material. For Au_3 bombardment at 1 nm on the Au side, again as in Figure 4.12, some Au atoms implant on the PE side, producing PE emission. The sputter yield of gold moves more laterally. On the other hand, the impact of C_{60} on PE, barely damages the gold side. The sputtered fragments of PE which collide with the gold interface, gain additional lateral momentum. In both cases, yellow arrows show the most frequent direction of the sputtered mass of PE and Au. In addition, the stress produced by the impacts on the gold side can also be observed (lines close to the impact which are produced by the

compression in each specific direction).

The crater formation and mechanism of ejection induced by Au are similar to those of Au_3. The crater formed by Au shows a similar shape as that of Figure 4.13b.

4.2.3 Additional comparison of the two samples bombarded with Ga and C_{60} projectiles

The two considered samples offer complementary microscopic views of the effects of metal-organic interfaces on the sputtering process. Therefore, to compare with the effects of impacting the interface of the *sample B*, the series of impact points 13, 22 and 31 of the Au coated *sample A*, which mimics a layer of gold evaporated on PE, Figure 4.1, are reused here (insets of Figure 4.14). These sets correspond to 3 series of 4 impacts for Ga bombardment: (i) in the PE zone; (ii) at the interface between the Au-NP and the PE surface; (iii) near the center of the Au-NP. The masses of the sputtered PE fragments are reported in Figure 4.14a for the two projectiles and the three bombarded zones.

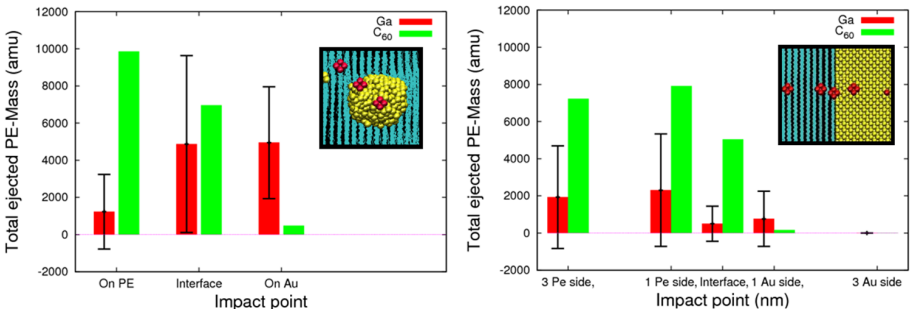

Figure 4.14: Total ejected PE mass in sample A (left) and sample B (right) for different impact points and projectiles (Ga and C_{60}). The insets show top-down views of the center of the samples with the considered aiming points.

Despite the differences between the two systems, Figure 4.14 shows that, upon C_{60} bombardment, the ejected PE mass is quite comparable for the corresponding regions surrounding the metal-organic interface (7-10 kDa in the PE zone; 5-6 kDa at the interface and less than 1 kDa in the Au zone). This good agreement between the two model samples confirms the very limited fluctuations observed with C_{60} projectiles. For both samples, displacing the impact point towards the metal by 1nm induces a drastic reduction of the yield, by one order of magnitude or more.

When Ga is used as a projectile, the situation is very different. In sample A, Ga shows an opposite behavior to C_{60}. On the other hand for sample B, despite the large standard deviation of the data, the results show that the average PE yield is not so dramatically affected when going from 1nm on the polymer side to 1nm on the Au side.

4.3 Note on the mechanism of crater formation in different materials

In the cascade effect started by a keV projectile, for each collision, a certain quantity of energy is transferred among the interacting particles. Depending on whether the energy transferred is higher or lower than the binding energy D of the target, and if the range of interaction of the projectile is of the order or higher than the interatomic distances - so the projectile channeling can be discarded - the process of crater formation and ejection can be explained as a function of the energy transfer E among the interacting particles/entities in each collision. In these conditions, it is possible to rationalize the differences in the crater formation in a bulk monoatomic system, or a polyatomic one with small or large molecules, using simple energy and geometrical concepts.

Consider any molecular target system with intramolecular binding energy D, and intermolecular energy ϵ. Let E be the energy transferred among the particles/entities involved at certain time in a collision cascade initially created in that target by a primary projectile with initial energy E_0 in the range of keV. As long as the relation $E >> D > \epsilon$ holds the collisions can be considered to happen only between individual pair of atoms. The collisions generated in the cascade can be considered as collisions of atomic entities in a complex interaction or spike regime, and geometry plays a second role, the density being more important. It is in this energy interval that the highest atomization of the sputtered fragments are produced. This is, because the atoms closer to the spike have a potential energy which is entirely repulsive. In this process, some recoil atoms that move with similar momentum may form a molecule - if the relative measured kinetic energy from their center of mass is of the order or less than D.

When the energy E is of the order or lower than the intramolecular binding energy D, $(D > E > \epsilon)$, the intermolecular interactions become important. The remaining energy is not sufficient to break bonds or produce fragments for ejection, and the particular geometry of molecules become an important factor to consider. However, in this energy interval, the entire molecules have the opportunity to leave the target without

being destroyed by the impact.

As an example, consider a bulk sample of PE, which can be either crystalline, or amorphous. For the PE crystal, two situations can be taken into account, the impact is perpendicular to the orientation of the chains or the impact is along their orientation. In the first case, the crater formation has two steps: in the beginning (when $E > D > \epsilon$) the crater takes the shape given by the atomic collisions. For example, approximately hemispherical if the projectile is a cluster and it has the same target mass. When energy relation changes to $D > E > \epsilon$, a collective or correlated movement of chains starts to create an elliptical crater oriented in the direction of the PE chains. Therefore, depending on the size of the PE chains, they can be either ejected, or displaced to the borders to form the crater edges. For the second case, when the PE chains are oriented along the projectile's trajectory, during the impact, the crater starts to form as in the first case. However, when E becomes lower than ϵ, the remaining energy is not enough to move the chains away, and its geometry stays almost as it was created in the first energy interval, although with some small variations due to the lateral movement of the chains. Those effects are observed in the Hamraoui and Delcorte work, [137] in which a PE crystal is impacted in both directions and with different energies.

If the PE structure is amorphous, the crater formation starts forming in a similar way as in the crystalline case. However, as E becomes lower than D, the crater evolution begins depending on the entanglement of chains (geometric arrangement becomes important). In the case, where chains are so entangled that they cannot be separated, and therefore not ejected without being broken, the crater keeps almost the shape created in the first energy interval when $E > D$. Although, in some cases, the chains can find the path or mechanism thereby they can leave the bulk without being broken, and change the shape of the crater. The same reasoning for the crater formation can be used for medium and small molecules, like for example benzene.

The case of bulk atomic (covalent or metallic) systems is more simple, because there is no intermolecular energy. The crater is formed while the energy E remains higher than the cohesive energy D, and afterwards the remaining energy is transformed into thermal forms, i.e., lattice vibrations.

To illustrate the similarities and differences during the crater formation as a function of the transfer of energy in time, Figure 4.15 shows the comparison of C_{60} (left) and Au_3 (right) impacts at the interface of Au-PE, at 0.5 ps and 25 ps. The top images at 0.5 ps clearly show that, the crater formation is quite similar for both types of materials

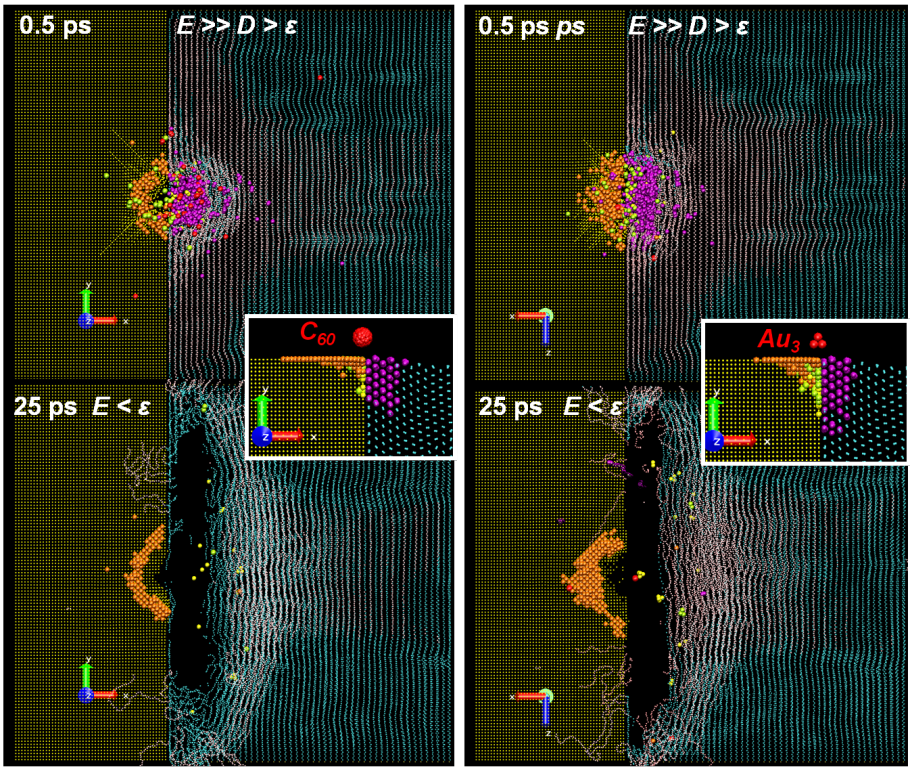

Figure 4.15: Top view of the crater formation as a function of the energy transfer for 10 keV impacts of C_{60} (left) and Au_3 (right) on the interface. Insets: side view at time $t = 0$ ps showing the origin of sputtered PE. Color coding: the same as in Figures 4.9 and 4.12.

and projectiles, independently of the target. At this time, the transfer of energy E is still higher than D. The main contribution is from the potential energies of the interacting atoms in the reactive zone, and it is entirely pairwise repulsive as given by the expression 2.46. In addition, both projectiles have almost transferred all the energy to the atoms involved in the cascade. In other words, as long as the atoms involved in the collision cascades keep the relation $E >> D > \epsilon$ in both samples, the craters will have the same evolution. Of course the radius of the crater on both sides is influenced by the differences of densities. The bottom of Figure 4.15 shows the final crater when the energy in the target is close to the thermalisation ($E < \epsilon$). At the end, the final morphology of the crater is defined by the geometry and the particular interaction types of atoms and molecules, hence the large difference between the two parts of the target.

4.4 Conclusions

The study presented in this chapter has helped to understand some of the physical mechanisms underlying the yield enhancement observed in metal-assisted SIMS, where a metal-NP overlayer is used to enhance organic secondary ion yields. In addition, a second system formed by two slabs with a metal-organic interface has been also studied. Both samples offer complementary microscopic views of the effects of metal-organic interfaces on the sputtering process.

When Ga bombards adsorbed gold NPs, it creates energetic gold recoils that efficiently transfer their energy to the PE surface by developing an extended collision cascade, instead of channeling deeply into the surface as it often does on pure PE. Therefore, the average PE sputtering yield tends to increase. Upon C_{60} bombardment, the reduction of the ejected PE mass when the impact is over the gold NPs is due to the fact that the energy of the carbon atoms is used to break the bonds between the gold atoms and that are unable to break covalent bonds in the PE surface. Results upon bombardments with Au and Au_3 on the same impact points have shown intermediate results when compared to Ga and C_{60}. For all projectiles, an increase of the size of the sputtered fragments when impact are on NPs is observed. This is because NP fragments spread and produce chain scissions in a wider area, and also because upon impact exerts pressure on the polymer.

The bombardments on the metal-organic interface and points close to it, have shown that impacts at 3 nm of the interface produce emission of only one type of material. At 1 nm of the interface, on the metal side, the organic yield upon C_{60}, Au and Au_3 impacts are reduced by one order of magnitude with respect to the yield produced at the interface. If the results are compared to the metal coated system, they show a good agreement. Finally, the crater formation can be qualitatively explained in terms of the energy transfers among colliding particles, the molecular dissociation energy D, the intermolecular dissociation energy ϵ, and the geometric arrangement of the atoms.

Chapter 5

From small to massive cluster projectiles

As it was observed in the Chapter 4 and in the literature, [1, 2, 3, 4] the comparatively mediocre performance of C_{60} and even Bi_n, [23, 138] for sputtering metal-organic layers when compared to monoatomic projectiles like Ga, forces one to look for other alternatives. Small light clusters are inefficient to retransfer momentum to the organic material when impacting adsorbed metal NPs; so, the use of heavy or large clusters may alleviate that problem. Therefore, this chapter focuses on two new types of cluster probes that are produced experimentally: the heavy Au_{400} and Ar_n projectiles.

This chapter is divided in three main sections. In the first section 5.1, C_{60}, Au_3 and Au_{400} are compared at constant energy of 10 keV. The second part, section 5.2, is related to Au_{400} at different energies. That section starts by analyzing the sputtered species distributions (5.2.1), and continues by investigating different cases of Au_{400} projectile interactions with the surface. Differences in behavior are explained in section 5.2.2. A particular emphasis is placed on the cluster-cluster interaction in subsection 5.2.3. The final part of this chapter, section 5.3, is dedicated to the interaction of metal-organic systems with argon clusters as a function of their energies and sizes.

5.1 Comparison of C_{60}, Au_3 and Au_{400} impacts

The main aim of this section is to compare the bombardment with C_{60}, Au_3 and Au_{400} projectiles at the same constant energy of 10 keV. Projectiles are aimed at the sample surface with normal incidence at three different strategic impact points; similar as it is done in section

4.2.3. The first one is over the center of the *Au*-NP, the second at the interface and the third on the side of the *Au*-NP, just over PE (remember the Figure 4.14).

In a similar manner as it is done for *Ga* and C_{60} in section 4.2.3, the respective results obtained for impacts over the PE surface, the metal NPs and the frontier between the metal and the polymer are analyzed and compared for the three projectiles. These results help to understand the behavior and to predict the performance of different cluster types for sputtering, as a function of the target nature.

5.1.1 Analysis of the sputtered mass

The sputtering data for the three aiming points are summarized in the Table 5.1. This table shows that, with C_{60}, the sputtered organic

	On NP	Interface	On PE
C_{60} bombardment			
Gold fragments mass	19.7	15.3	5.1
PE fragments mass	0.5	7.0	9.9
Au_3 bombardment			
Gold fragments mass	41.6	61.5	3.3
PE fragments mass	5.6	7.6	4.2
Au_{400} bombardment			
Gold fragments mass	12.6	35.0	3.0
PE fragments mass	0.3	0.4	0.0

Table 5.1: Mass of gold and PE (kDa) sputtered from sample upon 10 keV C_{60}, Au_3 and Au_{400} bombardment after 30 ps.

mass increases when the point of impact moves from the center of the Au_{555} NP to the PE substrate (1 order of magnitude difference). Upon Au_3 bombardment, the sputtered organic mass does not vary much when the impact point is changed. In contrast with the two other projectiles, 10 keV Au_{400} induces very little emission, irrespective of the impact zone. Additionally, if the average for the sputtered PE is taken over the three impacts points it gives 5.8 kDa, 5.8 kDa and 0.2 kDa for C_{60}, Au_3 and Au_{400}, respectively. These values suggest that, for a mixed surface where *Au* NPs would cover half of the PE substrate, one should expect that 10 keV C_{60} and Au_3 generate roughly the same emission yield of organic material while Au_{400} produces an order of magnitude less. Table 5.1 also reports the sputtered mass of gold at 30 ps after impact. It indicates that significant ejection of gold occurs only when the *Au*-NPs are hit

by the projectiles and that, at this energy, Au_3 is the most efficient to generate the emission of Au atoms and Au-NPs. However, the results of Table 5.1 do not include the mass of the entire Au-NPs that start to desorb at the end of the trajectories.

Figure 5.1 shows the PE sputtered mass versus the maximum cumulated kinetic energy of the atoms belonging to the top 3 nm of the target, i.e. the useful region in which the projectile energy should be

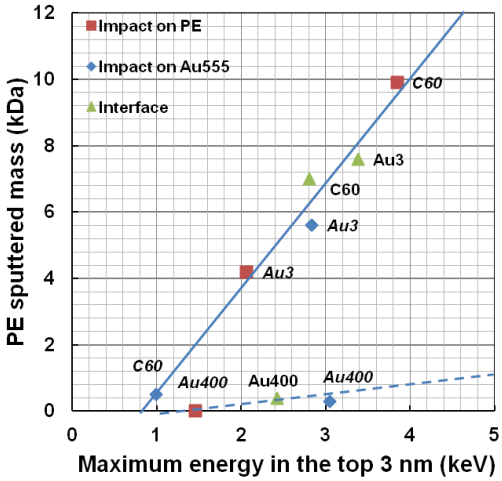

Figure 5.1: PE sputtered mass as a function of the maximum kinetic energy reached in the top 3 nm of the polymer surface for 10 keV initial bombardment. The colors relate to the impact points and the labels to the projectiles.

deposited to maximize emission.[131, 139] Overall, the energy deposited in the 3 nm layer is in the range of 13% to 34% of the initial projectile energy, the maximum being for the C_{60} impact on PE and the minimum for the C_{60} impact on Au_{555}. Figure 5.1 clearly indicates that, for C_{60} and Au_3, the PE sputtered mass is proportional to the maximum kinetic energy transferred in the extreme surface. The fact that the yield results obtained with these two clusters fit on the same line indicate that they both depend on that parameter in the same manner (in other words, the physics is similar). In addition, the different impact points fit quite well on this line, meaning that the details of the interaction, e.g. whether the energy is deposited directly in the polymer or via recoil atoms from the gold cluster, are irrelevant. However, the results obtained for Au_{400} exhibit a totally different behavior. First, unusually low sputtering yields are obtained despite the significant quantity of energy transferred to the surface region. Second, in strong contrast with C_{60}, the energy deposited

in the surface is the highest when the impact is on the Au-NP and the lowest, when the impact is on the PE substrate. In the following subsection, the mechanism of interaction is explored in detail in order to explain the difference of Au_{400} behavior.

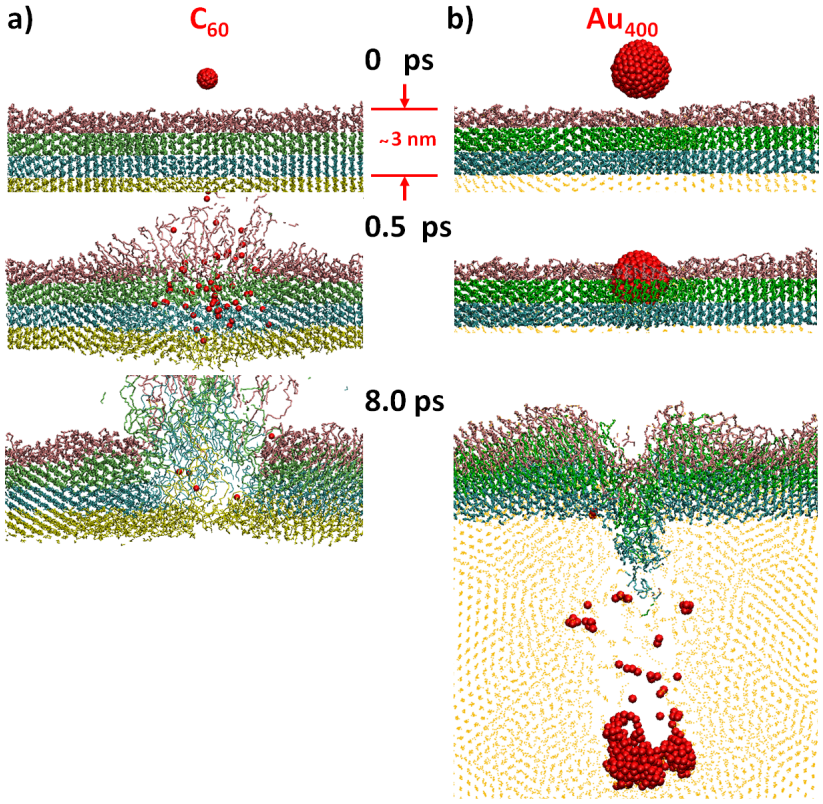

Figure 5.2: a) 10 keV C_{60} and b) Au_{400} projectile impacts over PE. The colored target layers are ∼1 nm each. Au-NPs are omitted for clarity.

5.1.2 Microscopic view

The snapshots of the molecular dynamics (see in Figure 5.2) show the differences between C_{60} and Au_{400} direct impacts in the PE substrate and they explain their opposite behaviors. Upon C_{60} bombardment (top frames), it is observed that C_{60} disintegrates upon impact on the surface, distributing its constituent atoms in a hemispherical volume that is large compared to the projectile size (crater is 6 times larger than the projectile diameter at 30 ps). In contrast, Au_{400} implants deep into the soft PE substrate, producing an inward motion of the organic material (bottom frames). This observation accounts for the very different

quantities of energy transferred to the PE surface upon 10 keV C_{60} and Au_{400} impacts. We assume that the penetration range difference for the two isoenergetic projectiles is due to a combination of reasons. First, for the same energy, the momentum of the Au_{400} cluster is ∼10 times larger than the momentum of the C_{60} cluster. Second, the mass ratio of the projectile atoms to the target atoms is totally different, i.e. C atoms can transfer all their energy to a target atom in a head-on collision while Au atoms can transfer a maximum of ∼25% of their energy (i.e. ∼6 eV) in such a collision (hard sphere approximation). Because of the mass ratio, Au atoms are only slightly deflected by their interaction with the substrate atoms (the reader is referred to Chapter 6 for a more complete discussion of these effects). Finally, C_{60} is an empty shell in which almost all the atoms directly interact with the target atoms (see in Figure 5.2), while Au_{400} is a full sphere in which only about half of the outer shell atoms (∼15%) initially interact with the target, while the core remains "protected". This effect is obvious in the animation of the trajectories, especially at higher impact energy, where the Au_{400} projectile shell atoms are literally "peeled off" upon interaction with the organic medium (this fact will be explained in more detail in the next section). In a recent experimental and theoretical study, a comparison of various cluster impacts on HOPG (graphite) allowed the authors to propose a law in which the ranges of the projectiles in the target were directly proportional to the projectile momentum p divided by the projected area A of the projectile on the surface (see in Figure 2.3 and Figure 6.7). [46] In our case, the value of p/A is only 1.3 times larger with Au_{400} than with C_{60}, (12.4 u$\text{Å}^{-1}\text{fs}^{-1}$ versus 9.7 u$\text{Å}^{-1}\text{fs}^{-1}$), which cannot account for the large difference of penetration depth (∼13 nm versus ∼1.5 nm). However, a close examination of the results reported in [116] shows that the aforementioned proportionality law does not seem to hold for the lowest values of p/A, around 10 u$\text{Å}^{-1}\text{fs}^{-1}$, when different types of projectiles are compared. Concerning our case, we believe that the main reason why the range of C_{60} and Au_{400} are so different is due to the very different masses of the cluster constituents.

Figure 5.3 shows snapshots of the molecular dynamics (1.5 and 30 ps) for impacts over the central Au_{555} NP. Impacts of C_{60}, Au_3 and Au_{400} are depicted in columns 1, 2 and 3, respectively as discussed in Chapter 4. C_{60} transfers most of the energy to the top of the NP, breaking many Au-Au bonds and inducing a strong pressure on the particle (first column). Because of the low projectile/target atomic mass ratio, a significant fraction of the projectile energy (35%) is immediately lost with the backscattered C atoms (see red atoms). Few energetic projectile/recoil atoms reach the PE substrate. Therefore, the maximum

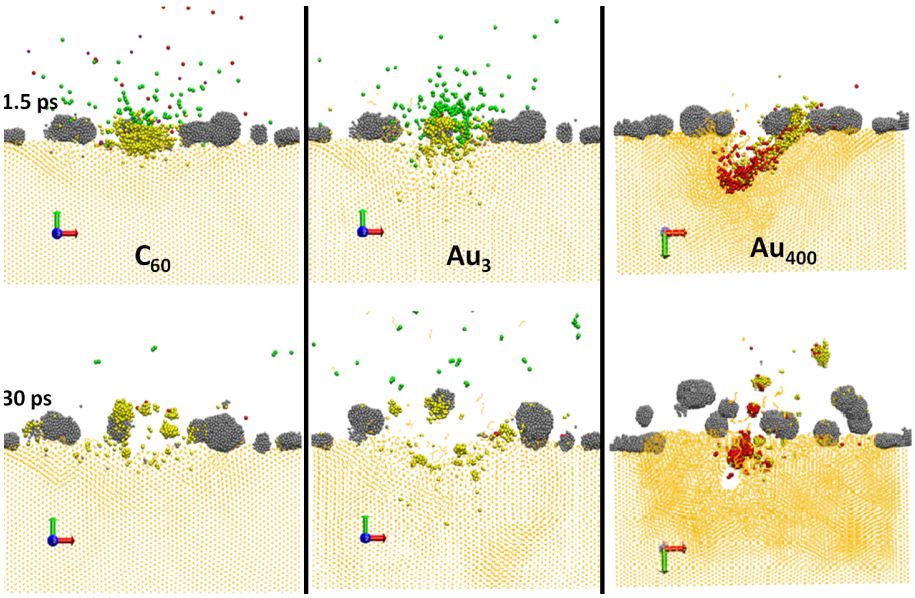

Figure 5.3: Au_{555} cluster fragmentation upon direct impact of 10 keV C_{60}, Au_3 and Au_{555} projectiles (from left to right). Top frames: 1.5 ps; Bottom frames: 30 ps. Color coding: yellow, central Au-NP; green, gold ejected from the central Au-NP; grey, other gold NPs; orange, PE; red, projectile.

energy transferred in the topmost PE layers is only 13% of the total (see in Figure 5.1), few bonds are broken and the PE sputtered mass is low. The behavior of Au_3 seems to be similar to the one of C_{60} (second column). In that case, however, the projectile transfers more momentum to the Au fragments, which in turn break many bonds and implant deeper into the PE substrate. As a result, more organic material is sputtered. Note that, like C_{60}, Au_3 is not implanted in PE, rather, it stops in the NP and transfers all of its momentum to the gold atoms. Finally, the last column of Figure 5.3 shows that the Au_{400} cluster splashes at the surface and blends with the Au NP (1.5 ps). It eventually stops in the topmost layers of the PE substrate where it deposits a substantial part of its energy (∼30%). However, because it acts as a whole and because the energy per atom is very small, few bonds are broken and little organic material is sputtered (see in Figure 5.1). In the end, a few large fragments combining projectile and target atoms are formed, as indicated by the ensembles of red and yellow atoms at 30 ps. Some of them have enough outward momentum to detach from the surface. Note that, for all the projectile impacts, some fragments of the central gold NP move laterally and recombine with other NPs, as shown by the mix of gray

and yellow colors.

5.1.3 Comparison with Au_{400} bombardment on gold coated amorphous PE

Here, it is also interesting to compare our results with the results obtained by Van Hoecke for his master thesis. [136] The amorphous sample with Au-NPs over it, was the same used in Section 4.1.7. In addition, Van Hoecke did a second sample with buried NPs. For that, the NPs were placed close to the surface with initial velocity of 0.05 Å/fs, and the system evolved until 850 fs. Next, it was restarted with velocities reset to zero and relaxed. Finally, the Au_{400} impacts at 10 keV, were done in the center of the Au_{555} NP and bare PE for both systems. The results of the total sputtered mass are given in Table 5.2.

Au_{400} bombardment	On NP	Interface	On PE
On crystal PE			
Gold fragments mass	12.6	35.0	3.0
PE fragments mass	0.3	0.4	0.0
On amorphous PE: NPs on surface			
Gold fragments mass	5.71	- -	0.4
PE fragments mass	7.63	- -	0.8
On amorphous PE: NPs buried			
Gold fragments mass	5.32	- -	0.0
PE fragments mass	17.65	- -	0.25

Table 5.2: Comparison of the sputtered mass (kDa) on gold coated amorphous and crystal PE samples upon 10 keV, Au_{400} bombardment. Results of the amorphous PE are taken from the master thesis of Van Hoecke. [136]

A careful analysis of the table indicates that impacts on the bare PE give similar low sputter yield of PE for the three samples. However, impacts on the NP show a large difference, more than one order of magnitude, between the total sputtered mass of the amorphous and the crystalline sample. Moreover, with buried NPs, an increase of more than double with respect to the case in which the NPs are over the surface is observed. For NPs over the surface, the explanation is the same as that given in Section 4.1.7. The increase is due to the fact that amorphous PE chains are not fixed, as they are in the crystal case. However, when the NPs are buried, another factor comes into play. When Au_{400} hits the buried NP, they first fusion in a similar manner as it happens on the surface, Afterwards, they literally explode in the organic matrix, causing

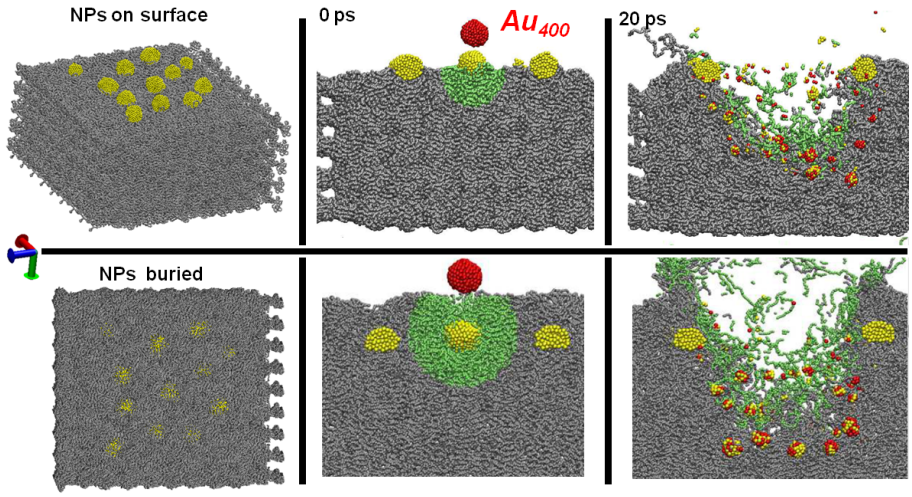

Figure 5.4: Amorphous PE with NPs on the surface (top) and NPs buried (bottom). Au_{400} impacts are on Au_{555} recycle from crystal structure. Frames taken from the master thesis of Van Hoecke. [136]

bond scisions and outward motion of PE fragments. The mechanism of ejection of the two amorphous samples is shown in the frames of Figure 5.4.

The results of those two additional samples corroborate the observation that Au_{400} produces low emission yield when it impacts on bare PE. However, when impacts are on the NP, a clear difference between the yield of the system with NPs on the surface, or buried is observed. Buried NPs induce a large enhancement of the sputtering yield upon Au_{400} bombardment.

5.2 Influence of the projectile energy upon Au_{400} bombardment

This section, explores the interaction of Au_{400} with a metal-organic system as a function of the projectile energy. The sample energies are set to 5, 10, 15, 20, 30 and 40 keV, which is equivalent to 12.5, 25, 37.5, 50, 75 and 100 eV/atom. Because of the higher energies, it was necessary to use a larger sample having dimensions of $30 \times 30 \times 25$ nm^3. The number of chains used in this system was 5200, implemented as it is explained in Section 3.3. Therefore, the total number of elements in the system was set to 1 053 386. The sample is shown in Figure 5.5. A second

relaxation for 10 ps was done. The total integration time was set to 30 ps. After this time the total ejected mass was gathered and analyzed. For the bombardment, Au_{400} clusters with energies ranging from 5 to 40 keV are aimed at two impact points on the surface, over the *Au*-NP and over PE. The projectile energy deposition and sputtering characteristics were investigated in each case.

5.2.1 Energy dependence of the sputtering

The sputtered masses of PE fragments and of gold atoms and clusters are shown in Figure 5.6 as a function of energy, from 5 to 40 keV. The emission of organic fragments, Figure 5.6a, increases as a function of energy for both impacts on the central Au_{555} NP and impacts on the bare PE substrate. However, the sputtered mass difference between these two situations is about one order of magnitude. This effect is particularly true for energies equal or larger than 15 keV. For 10 keV of energy and below, almost no organic fragment emission is observed. A second observation is that the sputtered mass evolution as a function of energy is non-linear in this energy range. It is best fitted by a square function (full lines in Figure 5.6a). This is in contrast with previous results obtained upon bombardment of amorphous polyethylene samples with C_{60} projectiles [139] and with Ar_n cluster bombardment of VdW bonded systems. [140] In the case of Au_{400} projectiles, the region ∼10-15 keV can be considered as the threshold of sputtering.

The organic fragment emission yield distribution (mass spectrum) is reported in Figure 5.7 for different energies and impact points (20, 30, 40 keV for direct impacts on the *Au*-NP, 40 keV for impact on PE). Given the specifics of our simulations, the statistics are scarce, but nonetheless indicative of some trends. First, in the low mass range (below 200 Da), the yield distributions are reasonably well fit by exponential functions ($Y = A\exp(-Bx)$, with R^2 values above 0.9-0.95). For impacts on the central Au_{555} NP, the exponential decay parameter B for the best fit is in the range 0.01-0.02 depending on the projectile energy. In contrast, it is close to 0.04 for the 40 keV impact on PE. At lower energy, the impacts on PE provide so little yield that such an analysis would be meaningless. The results of Figure 5.7 show that, in addition to generating higher yields of organic fragments, impacts of Au_{400} on the NP tend to sputter larger chain segments, as was the case for other projectiles (see in Chapter 4).

Figure 5.8 shows the depth of origin of the sputtered PE fragments. The vertical coordinate Z is calculated with respect to the *Au*-PE interface. The average depth and the vertical coordinate of the deepest

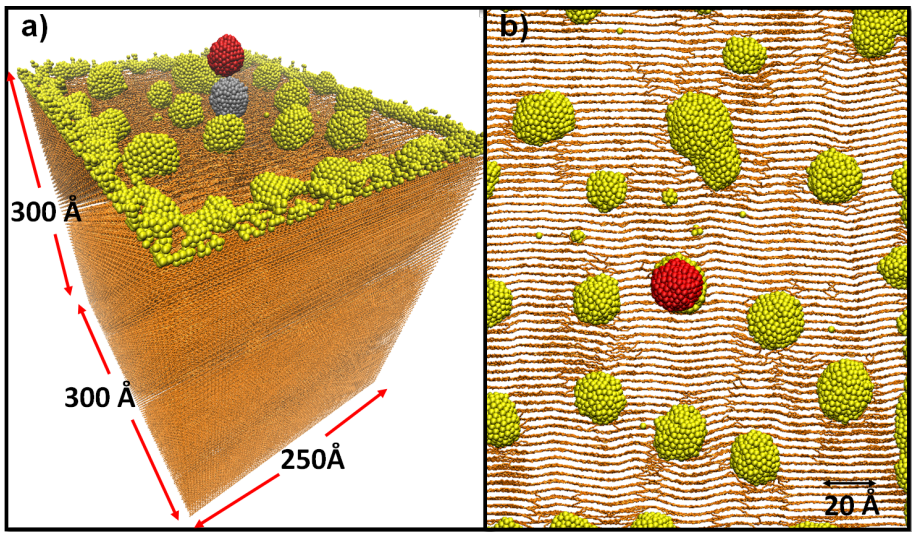

Figure 5.5: (a) 3D perspective view of the simulation cell after sample relaxation and before the bombardment. Configuration with the central Au_{555} NP (gray) and the Au_{400} projectile on top (red). The other Au atoms are in yellow and the PE coarse-grained units are in orange. (b) Top view of the same cell indicating the impact point. For impacts on PE, the gray NP is removed.

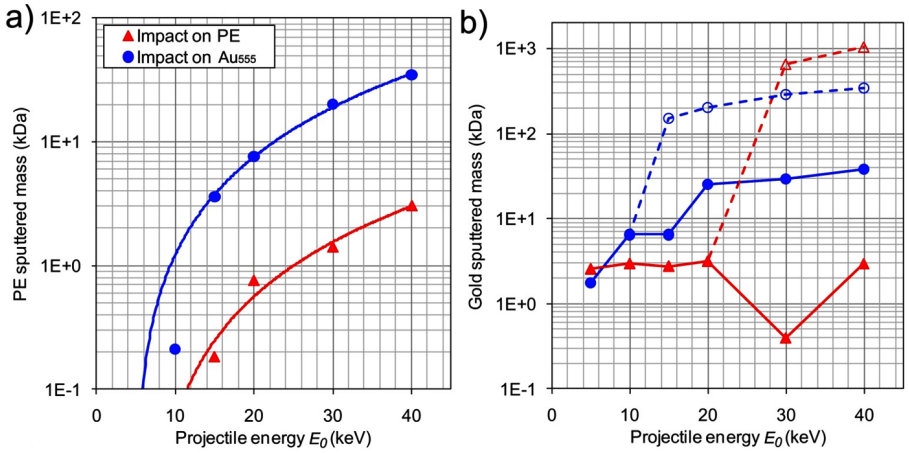

Figure 5.6: (a) Sputtered masses of PE fragments for impacts on PE and direct hits on the Au_{555} NP. (b) Sputtered masses of gold for the same conditions. Full symbols are for Au_n clusters with $n<10$ and open symbols represent the total sputtered gold mass, including entire NP desorbed at much later times.

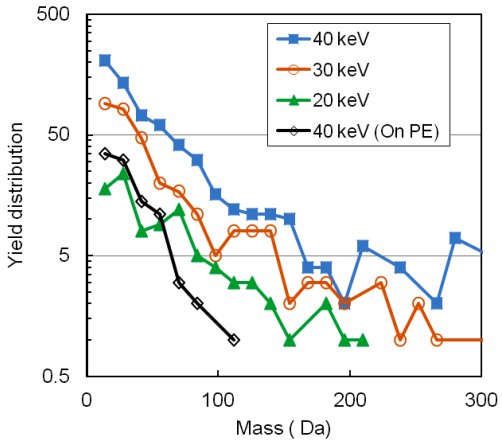

Figure 5.7: Yield distribution of PE fragments (number of fragments per impact as a function of mass). Impact on PE at 40 keV is compared to impacts on the central Au_{555} NP at 20, 30 and 40 keV.

ejected fragments (Z_{max}) are reported as a function of the projectile kinetic energy (E_0). Because the interface between Au and PE is not flat, these quantities may exhibit an error of a few Å, depending on the exact emission point on the surface. The depth of emission tends to increase with the projectile energy but, in all cases, most of the sputtered fragments and/or molecules originate in the top 20 Å of the polymer surface. However, there is again a clear distinction between impacts on the PE surface and on the Au_{555} NP. At all energies, impacts on the NP lead to average emission depths that are more than 2 times smaller with respect to impacts on the polymer. This result suggests that ion beam analysis of organic materials with Au_{400} in the MetA-SIMS configuration, that is, with Au NPs on the surface, should be more surface sensitive than the regular analysis conditions.

The sputtering of Au-NPs is also analyzed in Figure 5.6b. A distinction is made between small Au_n clusters with $n < 10$ (full symbols) and the total sputtered gold mass, including entire NPs desorbed intact from the surface (open symbols). For impacts on the central NP, the mass of small gold clusters (NP fragments) increases almost linearly with the impact energy (R^2 value > 0.9). The branching at 10 keV with the curve corresponding to the total mass indicates desorption of some of the surrounding NPs beyond that energy threshold. In contrast, impacts on PE induce very little fragmentation of the surrounding gold NP or backscattering of the projectile constituents. In that case, the intact NPs start desorbing at the energy threshold of 30 keV.

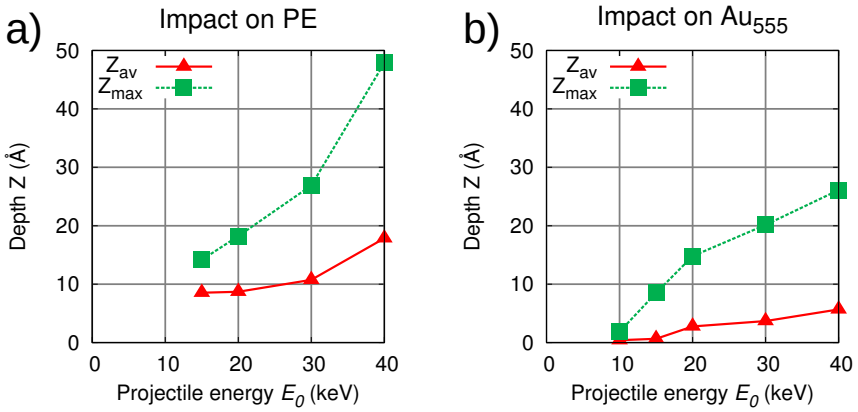

Figure 5.8: Average depth of origin of the sputtered PE fragments (Z_{av}) and Z coordinate of the deepest sputtered fragment (Z_{max}) as a function of the projectile energy for (a) impacts on PE and (b) impacts on the Au_{555} NP. The depths are calculated with respect to the Au-PE interface.

The following sections investigate the physics of the impacts and, in particular, the differences between impacts on the gold NP and the PE surface, giving rise to these sputtering characteristics.

5.2.2 Ranges and energy deposition in the surface

In order to understand the large sputtering yield differences between the impacts on the Au NP and over PE, additional information has been gathered from the analysis of the projectile penetration and energy transfer to the surface.

Figures 5.9a and 5.9b show cross-sectional views of the samples upon 40 keV Au_{400} impacts, when the projectiles reach their maximum penetration depth (8 ps for impact on PE and 4.5 ps for impact on the Au-NP). In Figure 5.9a, corresponding to the impact on PE, the projectile atoms are colored as a function of their position in the cluster projectile, in red for atoms belonging to the cluster outer shell and yellow for the cluster core. The projectile implants deep in the organic sample (>200 Å), creating a narrow track of broken bonds and damaged material. The predominance of red projectile atoms in the damage track indicates that the projectile is "peeled off" upon interaction with the organic medium (inset of Figure 5.9a). The picture also evokes the "clearing the way" effect, [40, 39] i.e. the front atoms of the projectile outer shell (red) clear the way for the core atoms (yellow). In contrast, Figure 5.9b, corresponding to the impact on the gold NP, shows the formation of a large

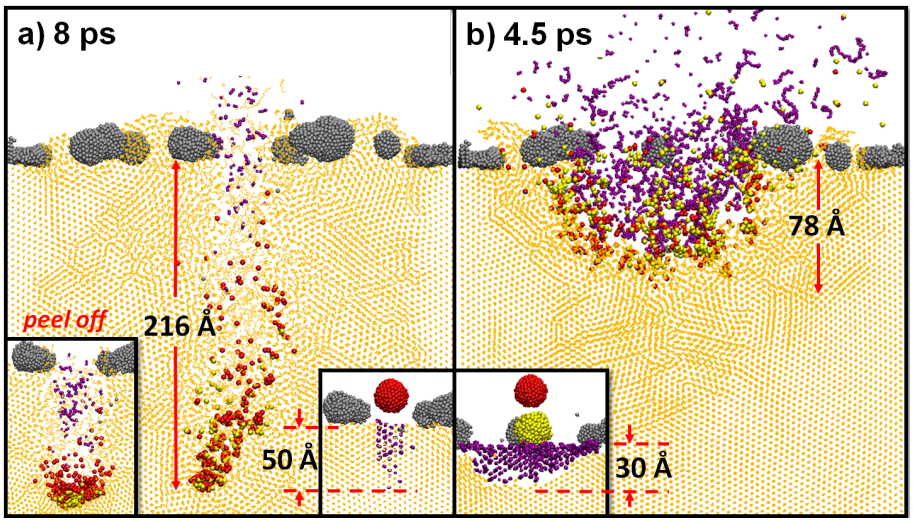

Figure 5.9: Cross-sections of the target at the time of maximum penetration for impacts at 40 keV, (a) on PE and (b) on the Au_{555} NP. The central insets show the origin of the PE fragments (purple) for each case. The left inset shows the effect of "peeling off" of the projectile (red outer shell and yellow core) at 1.5 ps. The vertical distances are calculated with respect to the Au-PE interface.

hemispherical crater with a diameter >100 Å (here, yellow represents the target Au_{555} NP). The maximum penetration depth (range) is attained when the PE material surrounding the crater reaches its maximum compression. At the end, the polymer crystal relaxes with a crater of only 30 Å of depth. Figure 5.10a and Figure 5.10b display the evolution of the penetration of the center of mass of Au_{400} as a function of time for different values of the initial kinetic energy. The first observation is that impacts on PE transfer all the projectile energy to the sample, while direct hits on the Au_{555} NP induce the backscattering of the center of mass. As the projectile energy increases, the reflection becomes faster (see in Figure 5.10b). Second, the different scales in Figures 5.10a,b (top) confirm that the range of Au_{400} is significantly larger upon impact on PE than on the NP for all the considered energies. In Figures 5.10c,d, (bottom) two different estimates of the maximum penetration depth are reported as a function of the impact energy. They are the maximum penetration depth of center of mass, R_{CM}, and the position of the deepest atom,R_{Max}. The divergence between the values of R_{CM} and R_{Max} with increasing energy is an indication of the pulverization of the projectile. This effect is more pronounced for impacts on the Au_{555} NP. This phenomenon was also observed for impact on graphite and gold crystals, as was noted by Anders and Urbassek. [41]

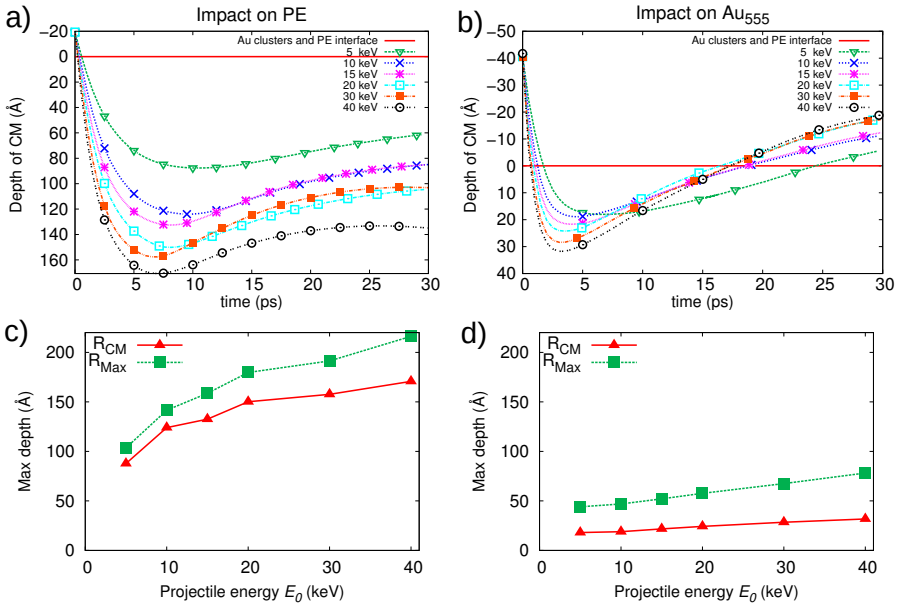

Figure 5.10: On top evolution of the vertical coordinates of the center of mass (CM) as a function of time for impacts (a) on PE and (b) on the Au_{555} NP. Bottom, pictures (c-d) show the maximum range reached by the projectile center of mass (represented by R_{CM}), and vertical positions of the deepest Au atoms of the projectiles (represented by R_{Max}), for these two types of impacts. The vertical distances are calculated with respect to the Au-PE interface.

To have a more detailed view of the energy transfer from the projectile to the sample, the simulation cell has been sliced in horizontal slabs of 3 Å each.The evolution of the kinetic energy in each slab was monitored as a function of time for the different trajectories. The kinetic energy was divided by the volume of the slab ($3 \times 300 \times 250$ Å^3) in order to compare the pressure that one slab exerts over its other two neighbors. However, it is important to point out that the internal pressure (the derivative of the kinetic energy with respect to the volume as it can be deduced from the definition of work) is not in phase with the kinetic energy, i.e. when one is maximum the other must be a minimum. Then, we interpret it as the total kinetic energy of the slab normalized to the layer volume at a fixed time t and that gives us information about how energy transfers between layers, and from one time step to the next. The results are displayed in Figure 5.11 for two energies (5 and 40 keV) and for two different impact points (on PE and on the Au_{555} NP). First, the energy plots of Figure 5.11 confirm that the energy is transferred in the entire depth of the sample upon impact on PE, while the energy peak

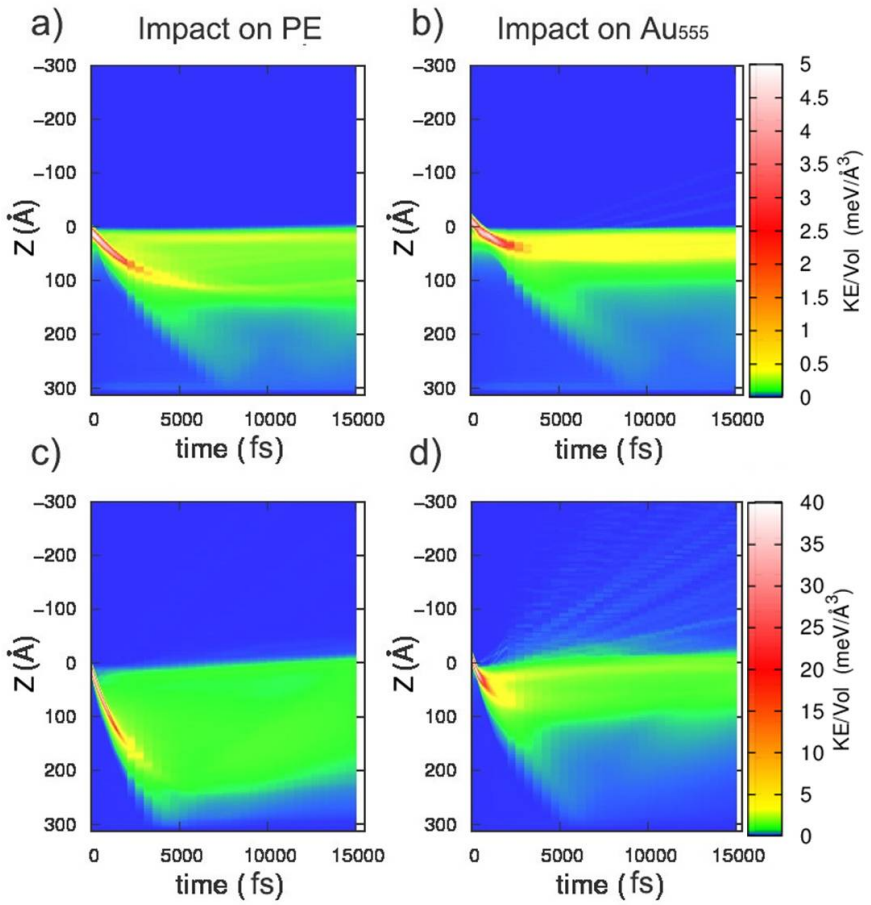

Figure 5.11: Evolution of the kinetic energy per volume of layer KE/Vol in the sample for impacts at 5 keV (a-b) and 40 keV (c-d). The left column corresponds to impacts on PE and the right column to impacts on the Au_{555} NP. The KE/Vol in each horizontal slab of 3 Å is color-coded from blue to white (color scales on the right). The time resolution is 50 fs for the first 2000 fs and 500 fs afterwards. The vertical distances are calculated with respect to the Au-PE interface.

is confined in the top 100 Å for impacts on Au_{555}. Second, the energy plots show that, for all the investigated cluster energies, the Au_{400} cluster impact generates an energy wave in the substrate, with an intensity that is proportional to the impact energy. The decoupling between the projectile implantation and the wave penetration is obvious, for instance, at 5 keV, where the projectile slows down while the wave continues to progress in the solid with an almost unchanged speed. The comparison between the two impact points indicates that the velocity of the wave is slightly larger when impacts are on PE. At 40 keV, it reaches the bottom of the substrate at ∼4 ps for impacts on PE and at ∼6 ps for impacts on the NP. Reflection of the energy wave on the bottom of the sample appears to be minor, indicating that the friction region on top of the last rigid layer plays its role. However, there is some reflection of the energy within the bulk of the substrate, after the initial compression induced by the projectile itself and the developing wave. It is shown by the green shadows below 200 Å in Figure 5.11c,d, which represents less than 0.5 per cent of the maximum energy per volume in the color bar. Finally, lighter rays developing above the sample surface (negative Z values) indicate the sputtering of surface species, for the impact on the Au_{555} NP.

Of particular interest is the energy deposition in the top layers of the polymer, because the sputtered material is mostly originating from there (see in Figure 5.8). The fraction of the projectile energy (E_{3L}/E_0) transferred to the top 30 Å of the target, as a function of the initial energy E_0, is shown in Figure 5.12. Irrespective of the projectile energy, impacts on the central Au-NP always transfer ∼25-30% of the total energy to the top 30 Å of the sample, i.e. E_{3L} is proportional to E_0. This is probably a consequence of the formation of a hemispherical crater in the top surface region. In contrast, for impacts on the organic material, the transferred energy fraction E_{3L} decreases with increasing total energy E_0. This decrease is best fitted by a power function of the form $E_{3L}/E_0 = aE_0^{-n}$ with $n = 0.475$, that is, very close to 0.5. The exponent 0.5 means that E_{3L}/E_0 is proportional to $1/v_0$. So, for a massive Au cluster impinging on a soft polymeric material, with the formation of a cylindrical track, our results suggest that the fraction of the projectile energy deposited in the surface layer is roughly proportional to the inverse velocity, i.e. to the time spent in that surface region. In terms of induced sputtering, Figure 5.12 also helps to rationalize the comparatively mediocre performance of Au_{400} projectiles when impacts are on the polymer.

Some of the characteristics observed in Figure 5.9 and Figure 5.11, such as the track formation and the energy wave development, are due to the cluster projectile effect, i.e. the fact that the constituent atoms of the projectile act as a whole rather than independently, but some

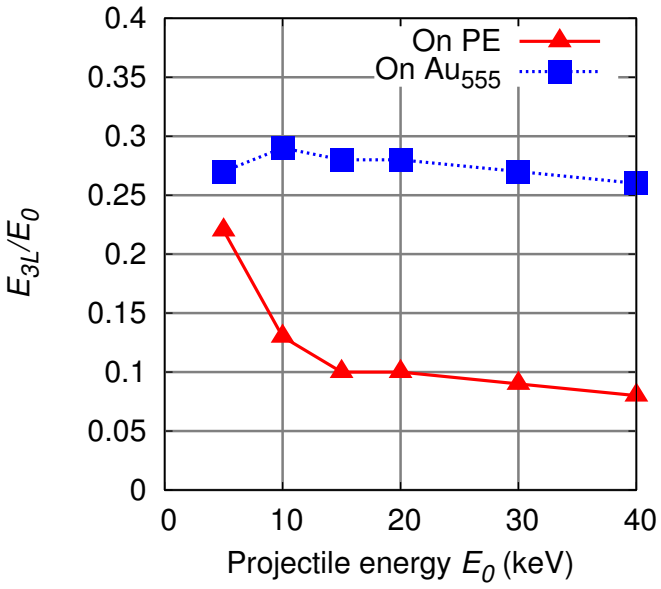

Figure 5.12: Fraction of the projectile energy (E_{3L}/E_0) transferred to the top 30 Å of the target as a function of the projectile energy.

aspects of the interaction can be explained with basic atomistic concepts. In particular, the differences between the impact on the PE and the impact on the NP can be rationalized on the basis of the different atomic mass ratios between the projectile and the target. More precisely, considering the hard sphere approximation and that the atoms of the target are at rest before the collision, when the projectile and the target have the same atomic mass, the sum of the deflection angles of each pair of colliding atoms is 90°. In this particular situation the energy transfer is a maximum. Now, as the time evolves the deflection angles change, the kinetic energy per particle reduces and the attractive part of the inter-atomic potentials becomes important. The global effect is the maximum angle of deflection of all the colliding atoms. This explains why, in the Au_{400}-Au_{555} collision, the damage is confined in the surface, with a semispherical crater, much like C_{60} impinging on PE [139] or Au_{402} impinging on bulk Au. [41] In contrast, because of the mass ratio between Au and C, Au is only slightly deflected by collisions with C atoms and the energy transfer per collision is limited. Therefore, the mass ratio between the projectile and the target atoms certainly plays a major role in the explanation of the different behaviors shown in Figure 5.9 to Figure 5.11.

Note that, in comparison with a bulk Au target, the spherical Au_{555} NP has a significant fraction of its atoms at the surface and, therefore, the total cohesive energy is reduced. Consequently, atoms can move with less constraint, increasing the Au emission yield by more than a factor of two in comparison with a planar target. This effect is also observed by Zimmermann and Urbassek for a spherical Au cluster of 200 Å of diameter. [141] In our case, as a direct result of the different penetration depth and energy transfer scenarios, many more C-C bonds are broken when the impact is on the Au_{555} NP. Indeed, a large fraction of the Au atoms propelled from the NP upon impact redistribute their energy in the organic material, inducing numerous C-C bond scissions and larger emission yields of organic material than direct impacts on PE.

This study of the projectile penetration and energy deposition in the surface explains the evolution of the sputtered masses of Figure 5.6. As it was explained in the previous section (see in Figure 5.2), at low energy ($\lesssim$ 10 keV), impacts of Au_{400} on PE are virtually unable to eject organic fragments and even less gold atoms. Instead, the projectile implants in the soft polymer, inducing an "inward motion" of the chains. On the other hand, 10 keV or less energetic impacts on the NP "splash" it without effective transfer of energy to the PE (see in Figure 5.3). At high energy, an additional mechanism comes into play. When impacts are on PE, the pressure wave induced by the compression of the material around the track eventually lifts up the surrounding polymer surface, which results in the ejection of some of the nearest Au-NPs, with an essentially upward momentum. An indication of this effect is seen in Figure 5.6b, between 20 and 30 keV, when the gold sputtered mass suddenly increases by more than two orders of magnitude. Pressure waves also lead to entire NP ejection when the impact is on the central Au_{555} cluster, but, in that case, an additional lateral momentum is conveyed to the nearest neighbor Au-NPs. This effect can be explained as a consequence of two combined phenomena. First, the Au fragments (or Au atoms) with a lateral motion transfer their momentum to the surrounding NPs. Second, the lateral development of the crater rim acts as an expanding wave, transferring additional lateral momentum. Many of the laterally moving Au atoms and small NPs also recombine with the nearest neighbor Au-NPs.

5.2.3 Cluster-cluster interaction

Cluster-cluster collisions are complex many-body interactions with specific properties. In order to explore the underlying physics, the kinetic and potential energies of the Au_{400}+Au_{555} system have been analyzed in detail over the first two picoseconds of their interaction. The variation

of the kinetic energies (per atom) of the colliding clusters is plotted in Figure 5.13 for different initial impact energies E_0. This plot shows that the dynamics is divided in two regions of time, separated by the maximum of the kinetic energy of the target cluster K_T and the change of slope of the projectile energy E_p. With increasing impact energy E_0, the maximum energy reached by the target cluster Au_{555} shifts to earlier times, as a consequence of the larger impact velocity.

In the first interval, before reaching the maximum of K_T, the total kinetic energy per atom K_{P+T} of the projectile and target Au_{400}+Au_{555} oscillates between its minimum and maximum values. This interval is characterized by multiple collisions among Au atoms, without interaction with the substrate. The binding energy of Au atoms is on average $E_{Au} \sim$ 3.0 eV/atom at the surface and $E_{Au} \sim$ 3.8 eV/atom inside the bulk (calculated with the MD/MC-CEM potential (2.37)). Therefore, at high impact energy ($>$ 10 keV), $E_{Au} << E_0$. In that case, the collisions can be considered as elastic. As mentioned before, the transfer of energy at each collision is a maximum, explaining the high negative slope of the kinetic energy E_p of atoms of the projectile as well as the high positive slope of K_T. Irrespective of the impact energy, more than 60% of E_0 is transferred to the surface cluster within that time range. In that first interval, the two clusters go through a stage of compression followed by a stage of decompression, as shown by the evolution of their potential energies in Figure 5.14 (40 keV case). The maximum potential energy around 250 fs corresponds to the local minimum of K_{P+T} in Figure 5.13. Figure 5.14 also indicates that the interactions with PE chains only start after the maximum compression of the gold clusters. Additional simulations with the same two clusters in the vacuum, i.e. without a PE substrate, and over a larger range of energies were performed to corroborate the results of Figures 5.13 and 5.14. They show that the behavior of the two clusters is equivalent with or without PE before reaching the maximum compression.

In the second time interval, beyond the maximum of K_T, the value of K_{P+T} decreases as the energy gets transferred to the PE substrate. The transfer of energy to the substrate is accompanied by a change of slope of the projectile energy E_p, which can be explained by the less efficient transfer of energy in collisions between Au and C atoms. A remarkable observation from Figure 5.13 is that E_p and K_T behave similarly after the maximum of K_T, for example, beyond 400 fs for the 40 keV case. This suggests that the atoms of the projectile and target clusters become undistinguishable after the collision. This effect is even more obvious in Figure 5.14, where the potential energy curves merge exactly beyond 300 fs, before the beginning of the energy transfer to the substrate. In other

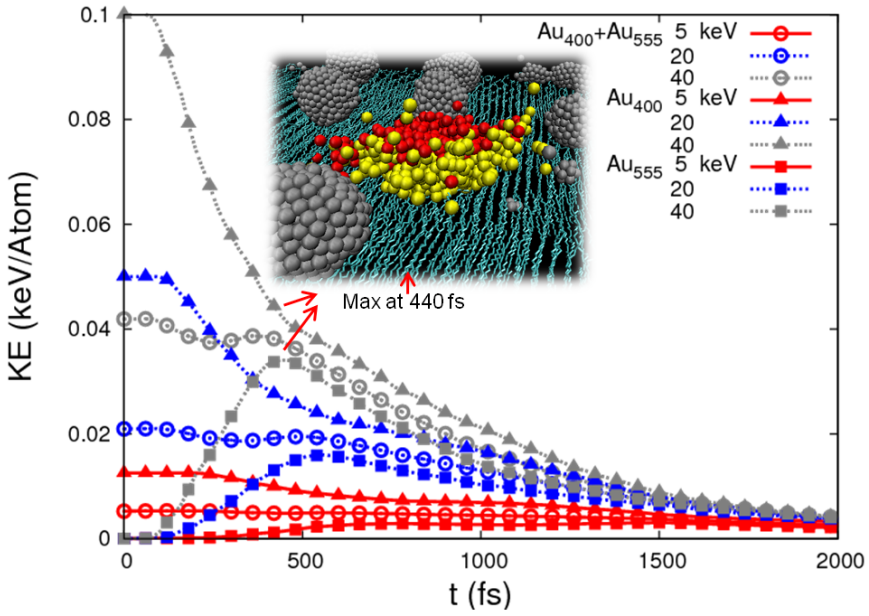

Figure 5.13: Time-evolution of the energy per atom for the projectile Au_{400} (E_P), the surface NP Au_{555} (K_T) and the combination of both Au_{555} + Au_{400} (K_{P+T}). The color coding indicates the projectile energy. Inset: microscopic view of the situation at the maximum of K_T for 40 keV bombardment. Atoms of the Au_{400} projectile are in red and atoms of the surface Au_{555} NP are in yellow.

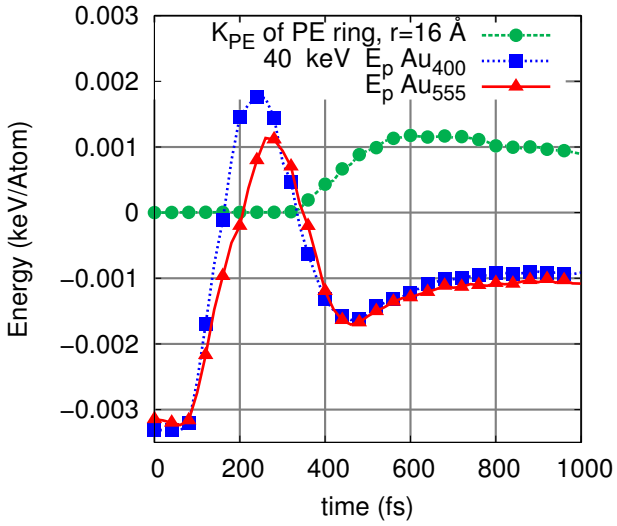

Figure 5.14: Time-evolution of the potential energy per atom (E_p) for the projectile Au_{400} and the surface NP Au_{555} (40 keV impact). The green curve (K_{PE}) describes the kinetic energy in the cylinder of PE under the impact point (16 Å radius and 30 Å depth).

words, the organic material does not see the impact of the projectile but rather the combination of both projectile and target cluster atoms, with a broad angular distribution of velocities, resulting from the initial projectile-target cluster collision. This velocity distribution resulting from the impact is responsible for the energy deposition into a wide semispherical volume just below the two fused clusters. This behavior clearly differs from the hypothetical impact of a projectile with equivalent total mass equal the sum of Au_{400} and Au_{555} masses, i.e., with 955 atoms (not calculated). In that case, all atoms would move in the same direction until they start the interaction with the PE surface.

5.3 Argon clusters

Argon clusters have recently focused the attention of researchers, and they have been studied both theoretically and experimentally. For instance, the Postawa and Garrison groups have used molecular dynamics (MD) to investigate the bombardment of some surfaces under different conditions and parameters with Ar_n clusters. [142, 143, 144, 145] Properties like surface erosion, depth-profiling, sputtering efficiency, as well as effects of impact angles using Ar_n clusters are explained by their studies. For example, they have probed the effect of the impact angle on the efficiency of ejection molecules emitted from benzene by Ar_{366} and Ar_{2953} clusters. It was observed that the angular dependence of the projectile impact is strongly affected by the projectile size. In addition, it was shown that the maximum sputtering yield was between 40 and 50 degrees. [143] From some other of their MD studies it is shown that, surface roughness also plays an important role in the total sputter yield when both kinetic energy and impact angle were modified. [146] Those simulations were not only achieved with Ar_n, but also with Au_3 and C_{60}. [145] However, in these works only sputtering of small molecules of benzene, and $Ag(111)$ surfaces are explored. There is no reference about other organic targets. Other MD simulations using Ar_n clusters have also been conducted by other groups to study other materials, e.g., Si, Ni, and other covalent and metal materials. [147, 148, 149, 150] The behavior of large molecules under argon cluster bombardment still needs to be studied.

Experimentally, it was shown that, incidence of argon clusters at low energy per atom (less than 1 eV), and at lower angles, favor the emission of intact molecular ions, in contrast to the fragmentation of the organic molecules. [151] Moreover, it has been shown that keeping the energy per atom in the range of the bond dissociation energy allows a control of the

broken bond number. [152] At a given acceleration energy, depending on the number of atoms on Ar_n clusters, they can keep the chemical structure intact, or seriously damage the target. [153] In a recent article, [154] the Ar_n clusters were studied under two hypotheses: first, the damage accumulation during organic depth-profiling should be reduced to a level below that observed with C_{60}; second, the spectra should be "cleaner", i.e., fragmentation should be reduced, and molecular ions at higher mass should be more readily detected. It was indeed concluded that large argon clusters cause less damage accumulation compared to C_{60}, with an approximately constant sputter rate as a function of argon cluster size, and that they induced a more gentle ejection in some samples. However, the experimental studies also show a reduction of the ionization of secondary fragments as the size of the argon cluster increases.

It is known from experiments that, covering the surface with noble metals helps to increase the ionization under atomic Ar^+ bombardments. [155, 156] However, to our knowledge, there are no reports in the literature on the use of Ar_n clusters with MetA-SIMS. Therefore, the aim of this section is to understand the influence of Ar_n clusters in MetA-SIMS. Additionally, to understand the mechanism of ejection and damage of large molecules under different initial conditions. For that, the effects of gold NPs on the organic emission, and the redistribution of energy when impacts are on NPs and on PE as a function of the energy and Ar_n cluster size, are studied.

The Ar-Ar and Ar-Au interactions are pair potentials of the LJ form 2.27 (with $\epsilon_{ArAr} = 10.3$ meV, $r_e = 3.82$ Å and $\epsilon_{ArAu} = 4.2$ meV, $r_e = 3.56$ Å), [66, 93] splined to the repulsive KrC potential valid for close encounters, [95] as it is explained in section 2.5.6. The Ar-PE interactions are handled with the pure KrC potential because hydrocarbons do not react with Ar atoms.

5.3.1 Emission produced by different argon clusters

To better understand the emission produced by Ar_n clusters, the results of PE emission are plotted as a function of different parameters and they are presented in the eight graphs of figures 5.15 and 5.16. The graphs are divided in two columns: on the left are impacts on PE and on the right are impacts on the Au-NP.

In Figure 5.15a, the total yield of PE is plotted as a function of the energy per atom of Ar in the projectile. Each plot is normalized to the number of atoms of the respective projectiles. For impacts on PE, the plots of each Ar_n cluster (Ar_{60}-Ar_{2000}), approximately fit on a single line. On the other hand, impacts on the Au-NP (see in Figure 5.15b), do not

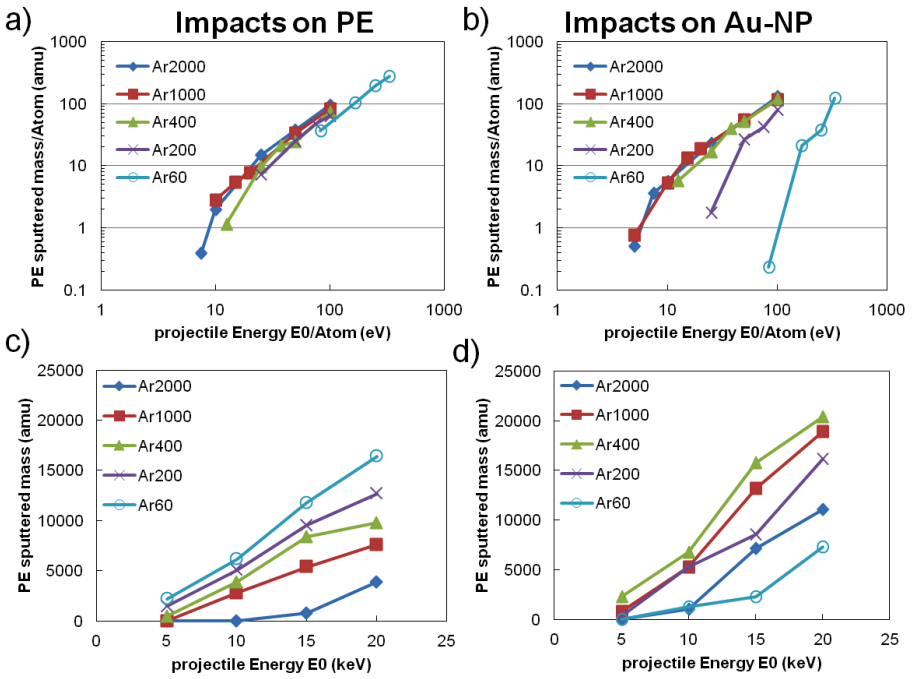

Figure 5.15: Comparison total PE sputtered mass of impacts on PE, and on *Au*-cluster on the surface.

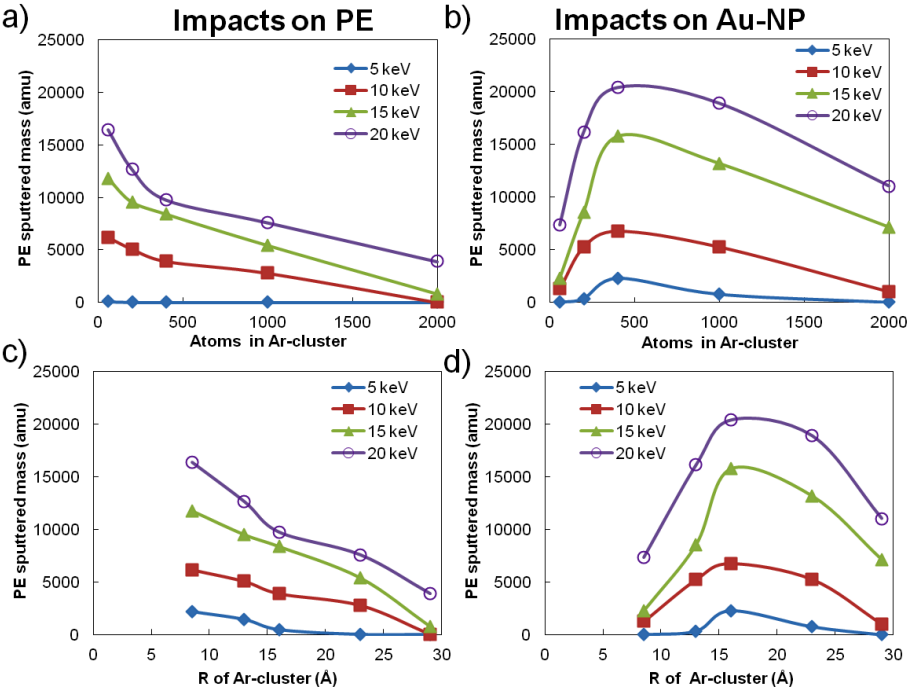

Figure 5.16: PE sputtered mass as a function of number of atoms n (top) and radius R (bottom) of the projectile.

fit in the same line for all the projectiles. Only the plots of the larger Ar_n clusters (Ar_{400} and beyond) seem to fit in a universal line. In contrast, the small ones (Ar_{60} and Ar_{200}), show an increase of the slope as the number of Ar atoms decreases. Figure 5.15c shows, for impacts on PE, a linear increase of the sputter yield (except for Ar_{400} and Ar_{2000}) with the projectile energy, and a monotonic decrease with increasing Ar atoms number in the cluster at fixed energy. Indeed, above a threshold energy, a similar increase has also been observed for other projectiles impinging on amorphous PE, [157] and for other materials. [158, 159] In contrast, impacts on the Au-NP do not follow the same behavior, showing the maximum emission when Ar_{400} was used (see in Figure 5.15d).

Figure 5.16 presents the plots of the total yield of PE as a function of number n of atoms (on top), and radius R (on bottom) of the Ar projectile. Impacts on PE show monotonic decrease for both parameters. However, in all cases, impacts on the Au-NP show a maximum for Ar_{400}, which has the closest radius to the targeted Au-NP (the radius of the Au_{555} target NP is $R_T \sim 14$ Å, while for Ar_{400} it is $R \sim 16$ Å). Moreover, these results show a different behavior depending on the side of the maximum. For $R < R_T$, all the projectile Ar atoms find in their trajectory Au atoms that are 5 times heavier, hence they are backscattered into the vacuum. On the other hand, for $R > R_T$, those Ar atoms that are beyond of R_T, can continue their trajectory until they are directly stopped and not strongly reflected by PE which is 3 times lighter.

Ar_{60} is one of the most interesting projectiles to analyze first, because the maximum emission and fragmentation is produced when Ar_{60} impinges on PE (see in Figure 5.15c). This due to the fact that it transports the maximum energy per atom, hence its performance producing organic fragments. Second, in contrast to impacts on PE, when impact are on the Au-NP, the maximum of energy reflected into the vacuum occurs with Ar_{60} (it reflects ∼30% of the energy with the scattered atoms into the vacuum at 5 keV, although this value decreases to ∼20% when the energy is increased to 20 keV). In summary, Ar_{60} exhibits extreme properties in terms of sputtering: when impact are on the Au-NP it shows the lowest sputter yield, but it is the highest when the impact is over PE.

In Table 5.3, Ar_{60} is compared with the well known C_{60}. For the impact on PE, the PE sputter yield produced by Ar_{60} is ∼1/3 less than that for C_{60}. Although Ar_{60} is ∼3 times heavier than C_{60}, it has less cohesive energy. As a consequence, Ar_{60} spreads in an approximately spherical region, when it impacts on organic targets, as C_{60} does because its atomic mass matches the atomic mass of the organic target.

	On PE		On NP	
	Fragments	Mass (kDa)	Fragments	Mass (kDa)
Ar_{60} 10 keV				
PE	229	6.174	19	1.260
Au	5	93.527	78	25.203
C_{60} 10 keV				
PE	313	8.456	15	0.476
Au	6	5.515	71	19.697

Table 5.3: Comparison of the total sputtered fragment numbers and mass for Ar_{60} and C_{60} projectiles at the same impact point, obtained by MD simulations.

When the impact is on the Au-NP, it is expected that Ar_{60} shows better performance in transferring its energy to the system because the atomic mass ratio between the projectile and metal-target is reduced. However, the increase is very small. Both projectiles show similar behavior when impacting the Au-NP.

Snapshots of the trajectory movies of 20 keV Ar_n bombardments, are shown in the frames of Figure 5.17. As before, impacts are separated in function of the target point, that is, impacts on the Au-NP (top figures) and impacts on PE (bottom). For impacts on the Au-NP we observe the strong reflection of Ar_{60} and Ar_{200}. In contrast, the other larger projectiles tend to cover the Au-NP, strongly reducing the Au-NP fragmentation (see in Figure 5.18a). That is, at given energy, if the projectile size increases, the size of the Au fragments become larger (see gold fragments represented in blue as a function of projectile, from left to right). The latter fact is understandable if we take into account that, as the size increases, the energy per atom decreases. However, at high energy, it is observed that large Ar_n clusters produce less fragmentation at the same energy per atom (see in Figure 5.18b). For instance, if the number of ejected golf fragments per atom of Ar produced by Ar_{60} and Ar_{2000} impacts is compared at the same energy of 100 eV per atom, a reduction by a factor of 7 is observed. That can be explained because Ar_{2000} completely covers the cluster, restricting the movement of the gold atoms.

On the other hand, the bottom frames of Figure 5.17 show that, for impacts on PE, the crater formation is similar for Ar_{60} and Ar_{200} at 0.5 ps and 30 ps. Beyond Ar_{400} the depth of the crater decreases as the number of atoms in the projectile increases.

Finally, a comparison of the total total number of sputtered fragments and sputtered mass is summarized in Table 5.4. Au_{400}, Ar_{400}, and Ar_{2000}

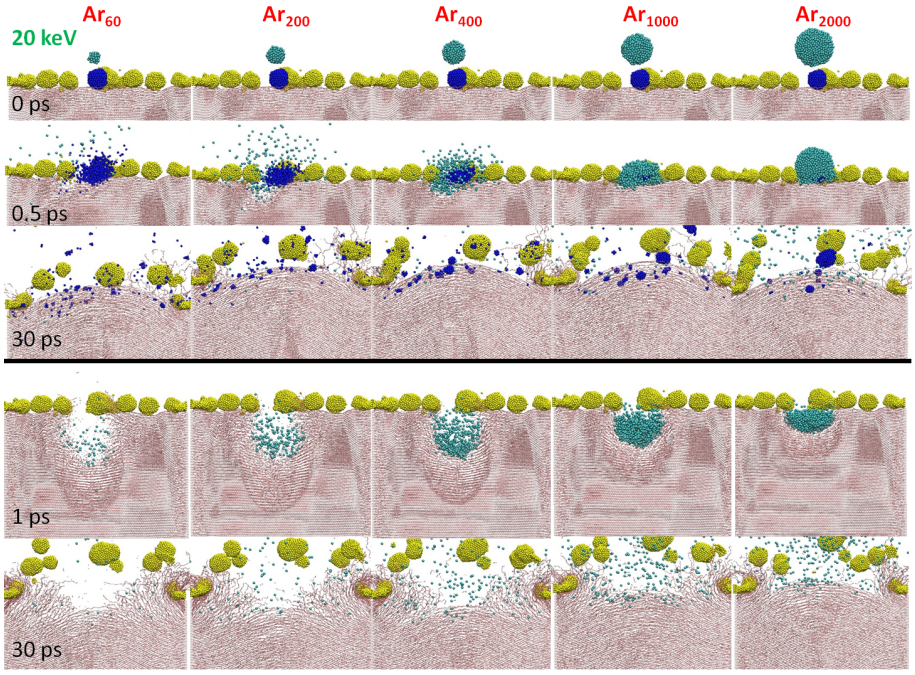

Figure 5.17: 20 keV Ar_n projectiles. At the top of the Figure: impacts on Au_{555}-NP over PE. At the bottom: impacts over PE. Color code: pink is PE; cyan and yellow are the projectile and Au-NPs, respectively; the target NP is in dark blue.

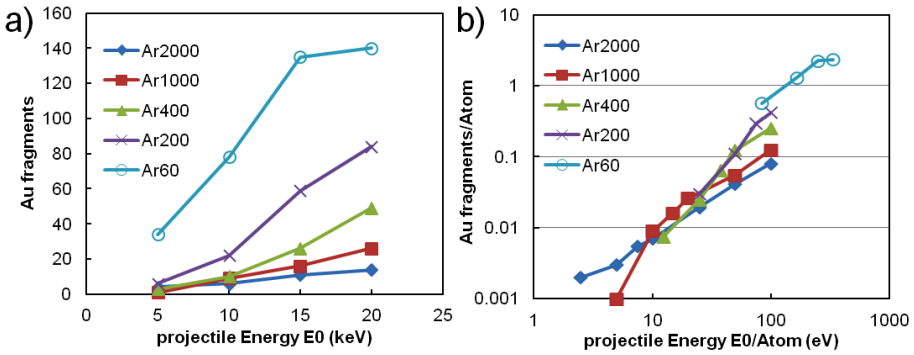

Figure 5.18: Number of ejected Au fragments as a function of energy (a), and Au fragments per number of atoms in the projectile as a function of the energy per Ar atom (b). Impacts are on the Au-NP.

are compared at 20 keV. The smallest total yield is produced by Au_{400} impacts on PE. The highest yield is observed for Ar_{400} impact over the Au-NP, which creates four times more fragments than Au_{400} and three times more than Ar_{2000}. Even, Ar_{400} produced 18 times more yield when impacts are on bare PE than Au_{400}. Then, Ar_{400} clearly shows a better performance than Au_{400}. Moreover, it is better than the performance of Ar_{2000}, so to increase the size of the cluster does not enhance the yield.

	On PE		On NP	
	Fragments	Mass (kDa)	Fragments	Mass (kDa)
Au_{400} 20 keV				
PE	15	0.756	99	7.602
Au	4	3.151	62	200.712
Ar_{400} 20 keV				
PE	283	9.758	457	20.426
Au	12	460.942	49	233.917
Ar_{2000} 20 keV				
PE	21	3.892	146	11.046
Au	8	175.437	14	342.212

Table 5.4: Comparison of the total number of sputtered fragments and mass for Au_{400}, Ar_{400}, and Ar_{2000} projectiles, obtained by MD simulations.

5.3.2 Low energy impacts with the heavy Ar_{2000} projectile

The results shown in the Figures 5.15 and 5.16 suggest that large Ar_n clusters with less than 10 eV of energy per atom produce less fragmentation in organic samples. This is in agreement with experiments. [157] However, the previous simulations cannot say anything about the emission of large molecules. This is because the system was created to model the fragmentation of infinite chains, and the ends of the chains were fixed for this purpose. Therefore, in order to study the emission of large PE chains of 2.8 kDa (200 elements) using Ar_{2000} at the energies of 5 keV and 10 keV, three additional simulations were done up to 80 ps using different border conditions. It should be noted that the projectile energy per atom in both cases, is less than the energy required to break the bonds of the chains. This is done in order to corroborate if keeping the energy per atom below the binding energy of the chains helps the emission, as it was said in references [151, 152, 153, 154]. Figure 5.19 shows the results at 50 ps for three different conditions on both stochastic and

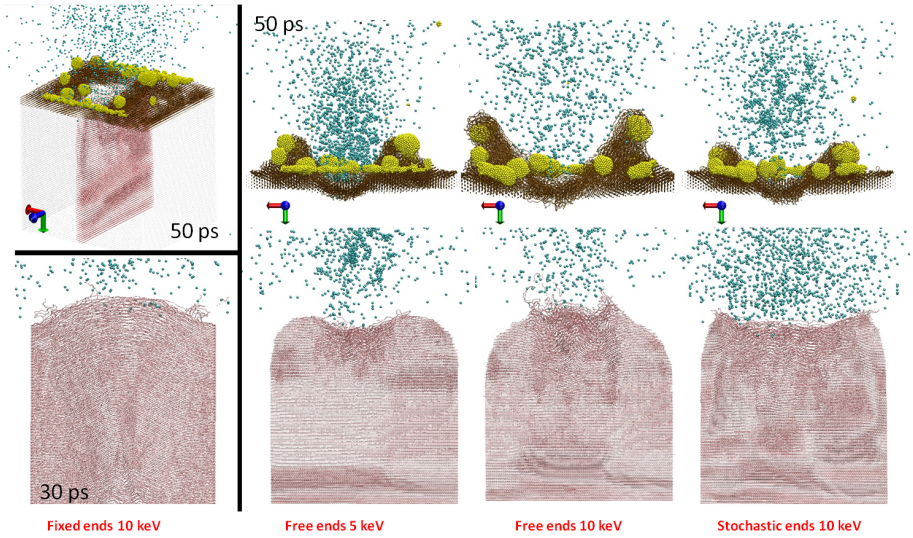

Figure 5.19: Ar_{2000} 10 keV impacts using different border conditions. Border effects on emission of large PE chains of 2.8 kDa. Color code: the same as in Figure 5.18 but here pink and brown are the vertical and top horizontal slides of PE, respectively.

rigid zones. The top frames represent the top 3 nm layers (colored in brown), while the bottom frames represent the vertical cross sections of 3 nm of thickness, which are just below the impact point. They are also compared to the previous result of 10 keV Ar_{2000} impact with fixed ends (bottom left frame at 30 ps).

In contrast to the previous simulations in which the chain ends were tied by rigid atoms, here, the rigid zone, which is perpendicular to the direction of polymerization (at the ends of the chains), is no longer used. The rigid atoms of those two sides are now allowed to move. Three different runs were done: a first one with no stochastic zone and 5 keV of initial energy, a second one with the same conditions but at 10 keV; and a third one with a stochastic region of 20 Å and 10 keV of initial energy. In the three cases the other two sides were kept as before, but the stochastic zone in the bottom was increased from 15 Å to 70 Å.

Due to the highly ordered arrangement of the PE crystalline structure, the emission of large chains, was expected. Indeed the surface chains should gain correlated momentum in the vertical direction. However, it was not the case, as was corroborated for the three impacts at 80 ps. In contrast to the sample in which chains ends were tied to the borders, this sample with free border conditions shows a severe plastic deformation. Energy is not used to produce yield but it is rather dissi-

pated as internal energy. The plastic property of organic materials can be considered as a drawback for the sputtering of large molecules. Another drawback is that the chains are just too long, which makes their ejection difficult. In Figure 5.19 is observed that the chains move to the sides and tends to wrap around the NPs.

5.4 Conclusions

In this study three different analyses were done. First, the interaction of 10 keV C_{60}, Au_3, and Au_{400} projectiles with mixed metal-organic surfaces has been analyzed in detail and some of the important physical parameters governing the sputtering process could be identified. Second, Au_{400} impacts on a polymeric target have been compared with impacts on a physisorbed Au-NP. The differences of emission yield, energy deposition and ranges were analyzed in detail for projectile energies ranging from 5 to 40 keV. Third, Ar_n impacts with six different projectile sizes were analyzed in the same manner, i.e. for impacts on PE and impacts on the Au-NP. The sputter yield was analyzed as a function of the energy, energy per atom, radius and number of atoms in the Ar_n projectile.

The comparison of Au_3 and C_{60} with Au_{400} shows that the manner in which the energy is deposited is crucial. For example, 10 keV Au_{400} does not create energetic recoil atoms. Therefore, it does not induce many bond scissions in the sample, which are necessary to obtain large sputtering yields from the polymer. In comparison with C_{60} and Au_3, which provide equivalent yields of sputtered PE fragments for such a mixed metal-organic surface, we observe that, at low energy, Au_{400} is not a suitable projectile for SIMS because it induces comparatively low yields of PE fragments.

Simulations with Au_{400} at high energies show that the projectile implants deeper and ejects much less organic material when the impacts are on the polymer rather than the NP. The role of the adsorbed NP is to increase the stopping power and decrease the projectile range, confining the projectile energy in the topmost layers of the organic sample. These observations suggest that MetA-SIMS might be advantageous with Au_{400} projectiles. When impacts are on gold, the projectile first splashes and fuses with the target NP so that the two mixed clusters behave like a single entity, where their atoms have the same average kinetic energy and a broad angular distribution that deposits the energy in a wide hemispherical volume of the polymer substrate. The behavior of Au_{400}, with a range exceeding 200 Å in polyethylene at 40 keV, indicates that it should not be suitable for molecular depth profiling of organic and polymeric

samples. However, the results also show that the sputtered fragments originate from an average depth < 20 Å in all cases, which is in broad agreement with the surface sensitivity deduced from experiments. Via collective molecular motions and pressure wave expansion in the polymer, the projectile impacts are also able to desorb entire NPs ($\sim$25 Å in diameter) from the substrate.

Finally, the results with Ar_n projectiles show that, as before, the PE fragmentation strongly depends on whether the impacts are on PE or on the Au-NP. The sputter yield of impacts on PE matches a universal line as a function of the energy per atom. However, this result is not held when impacts are on the Au-NP. Additionally, impacts on the Au-NP follow an non-monotonic function when the sputter yields are plotted vs the size of the cluster, with a maximum close to the situation in which the sizes of the projectile and Au-NP match. Thus, the sputtering produced by Ar_n on metal coated surface shows a strong dependence of the relative size of the projectile and target NP. Those results suggest that, experimentally, guaranteeing a projectile size close to the average sizes of the metal NPs could help to increase the number of sputtered organic ions. Ar_n projectile also produce sputter yield from the top layers of the surface, similar as C_{60}. Thus, Ar_n can be considered as well suited as C_{60} for surface analysis. On the other hand, the analysis of low energy impacts with the large Ar_{2000} and under different boundary and stochastic conditions, show that emission of large entire molecules is difficult due to the high plasticity of the PE and large size of chains. However, because the chosen crystal structure is very specific, more studies with other target structures, for example, amorphous PE are needed to better prove this fact.

Chapter 6

Effects of atomic mass in cluster-induced sputtering

The process of sputtering involves various physical quantities which are particularity important for secondary ion mass spectrometry. This chapter is therefore devoted to understanding the effects of those physical quantities. More precisely, a detailed study of the effects of changing the atomic masses of the NPs on the organic surface and the cluster projectile is done. The focus is placed on SIMS and how to increase the organic yield.

6.1 Role of the atomic mass in cluster-target collisions

From the results of this thesis and from the literature, [41, 44, 139, 141, 158, 159] it can be observed that the maximum sputter yield is obtained when the projectile and target atomic masses are equal. However, none of the previous references discusses this fact. For instance, in collisions into the keV energy regime, this argument can be verified in the case of C_{60} impinging on graphite, fullerite or other organic substrates, [44, 139] where the main components are carbon atoms. This is also valid for heavy clusters like Au_{400} impinging on flat gold targets or Au_n NPs, [41, 141] and even gold coated organic surfaces (see in Figure 5.9). In these cases, if the attractive interaction energy is negligible with respect to the initial kinetic energy per atom, the energy is deposited in a spherical region. A large emission yield is observed and a spherical crater is formed depending of the target density. Additionally, in another recent article, where the polyatomic projectile and target are made of the same molecules (O_2), the question of how far the dissociation energy D of

molecular targets influences the sputter yield is addressed by artificially changing D from 0.1 (close to the intermolecular Van der Waals energy ϵ) up to 20 eV (of the order of the projectile energy per atom used). It is found that the sputter yield only varies by $\pm 20\%$. [160] Here also, the energy is deposited in a spherical region. We can use the same atomic mass ratio argument to explain the extreme cases, when D is 0.1 or 20 eV. At low D (0.1 eV), the projectile energy per atom is higher than the molecular dissociation energy D, thus the spherical crater is formed by each pair of colliding atoms. In contrast, At high energy D (20 eV), the projectile energy per atom is close to this value, so few bond are broken. However, this energy per atom is higher than the intermolecular cohesive energy ϵ; therefore, the crater is formed by the colliding polyatomic molecules. The fact that the cluster and target have the same atomic masses, under the condition that the projectile energy be higher than the cohesive energy (or intermolecular energy in the case of molecules), could have a more important effect in the corresponding emission than other parameters.

6.1.1 Choosing the artificial atomic mass values

In order to understand the role of changing the atomic masses of the target and the projectile in the keV energy regime, complementary simulations have been conducted. For that, the same *sample A* with gold NPs has been used. More precisely, the simulations were divided in two different sets: One where the Au atomic mass was varied and the other where the C_{60} atomic mass was changed. For all the cases, the impact energy was set to 10 keV. This value, fulfills the condition that the projectile energy per atom must be higher than the corresponding interaction energies, and guarantees the full fragmentation of C_{60}. [44] In the first set of simulations, the atomic mass of the Au NPs was artificially replaced by the values of (arrows means equivalent to):

$$\begin{aligned} 1 \text{ amu} &\approx Au/197 \rightarrow H \\ 14 \text{ amu} &\approx Au/16 \rightarrow C \\ 69 \text{ amu} &\approx Au/3 \rightarrow Ga \\ 98 \text{ amu} &\approx Au/2 \rightarrow 7CH_2 \\ 138 \text{ amu} &\approx 2Au/3 \rightarrow 2Ga \\ 197 \text{ amu} &\approx Au \rightarrow Au. \end{aligned} \tag{6.1}$$

The other parameters of the system were kept constant. Then, the central NP was bombarded by C_{60} and Ga. Because of its cluster nature, C_{60} shows a small variation of the sputter yield, [53] so only one impact

per value of mass was done. In contrast, Ga, as atomic projectile shows large variations of sputter yield depending on the impact point. Therefore, four impacts with separations of 0.2 nm were computed, and the results were averaged over those values, using the mean value and the standard deviation for the confidence interval.

6.1.2 Changing the atomic mass of the NPs

For these simulations, the atomic mass of the Au-NPs was replaced by the values given in (6.1). Impacts were done on the center of the Au_{555} NP. After 30 ps, the total PE ejected mass and fragments were gathered and analyzed (see in Figure 6.1). Moreover, an additional set

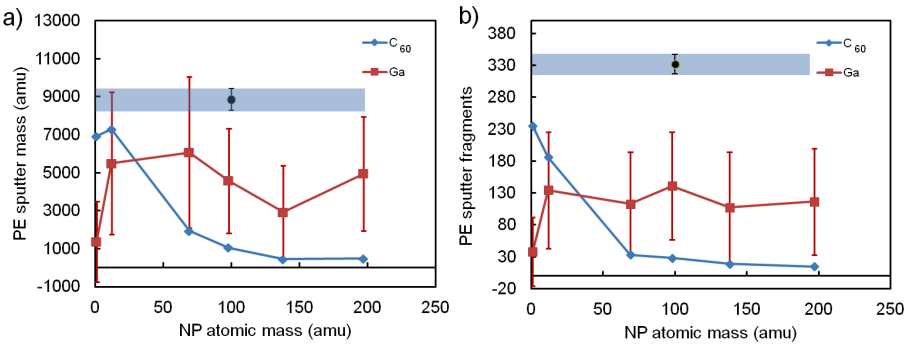

Figure 6.1: Sputtered mass and emission yield of PE fragments when impacts are over NP as a function the NP mass after 30 ps. The impact energy is 10 keV. Data are compared with the interval of emission of the C_{60} impacts over a bare area of the PE surface.

of five simulations with C_{60} impinging on PE at different impact points were done to compare with the impacts on the NP. These results are represented by the point with error bars that shows the corresponding interval of emission (blue bands in Figure 6.1a,b). Those plots show that, although the average emission produced by Ga tends to remain approximately constant (except when the atomic mass of the NP is equal to H), there are large fluctuations, which are characteristic of atomic projectiles. [53] Moreover, for Ga in Figure 6.1a, the average of the PE sputtered mass over the different atomic masses, is ∼40% lower than the corresponding average produced by C_{60} impinging on PE (as it can be compared to the blue band in the plot). While in Figure 6.1b, the average of the PE sputtered fragment numbers is ∼60% lower. In the latter case, the corresponding intervals in each average (C_{60} and Ga impacts on NP compared to C_{60} impacts on PE) do not have common values for the PE emission.

On the other hand, C_{60} impacts on the NP show that the emission decreases as the atomic mass of the NP increases. This is understandable because of the large size of the C_{60}, so it covers a larger area than Ga, and because as the NP atomic mass increases the inertia also increases. Thus the reflection of the carbon atoms increases. The maximum of the PE sputtered mass is when the projectile and the NP atomic masses match, but the sputter yield of PE is still lower than the sputter yield for the C_{60} impacts on PE. This can be explained by the energy spent to break the bonds of the NP.

It is important to note that, for the considered metal-organic system, some late events might still happen after 30 ps, such as late desorption of massive intact NPs. Therefore, caution should be used in the discussion of the sputtered mass values. Consequently, nothing can be said about the gold emission except that, as its atomic mass is reduced, the Au_n-NP fragments are ejected with higher velocities.

Figures 6.2a,b show a comparison of the average kinetic energy per atom of the NP (KE) as a function of time for each impact with C_{60} and Ga. For all the plots, the average KE of the NP reaches a maximum and later decreases as the energy is transfered to the PE. However, those maximums, as well as the rate of the energy transfer, are different when C_{60} and Ga are compared. With C_{60} impacts, the peak maximum, increase as the projectile and the NP atomic masses become close, having a maximum value when the atomic masses match. These peaks occur faster as NP atomic mass decrease. In contrast, the KE maximums reached with Ga impacts occur faster than with C_{60} and the sizes of the peaks are independent of the atomic mass of the NP. They rather show a chaotic behavior as a function of the NP atomic mass. Depending on the exact atomic mass of the NP, Ga can collide with atoms of the NP in many different ways and even it can channels through the NP. This stochastic situation creates a broad range of possibilities for the fragmentation and projectile energy transfer in the NP. It is also responsible for the large fluctuations in Figure 6.1. The comparison between C_{60} and Ga impacts also shows that energy transfers faster from the NP fragments to the PE when impacts are with Ga, with the peaks reached in the first 20 fs (see inset in Figure 6.2b). After 1500 fs, only $\sim$2 keV remains in the Au fragments upon Ga bombardment against $\sim$4 keV upon C_{60} bombardment (except for atomic mass of Au equal to one amu). This observation is in agreement with the results shown for sputter yields in Figure 6.1.

The fragmentation of the target NP is also analyzed using the movies from the simulations. Monoatomic and polyatomic projectiles show a very different behavior when they interact with the NPs over the sur-

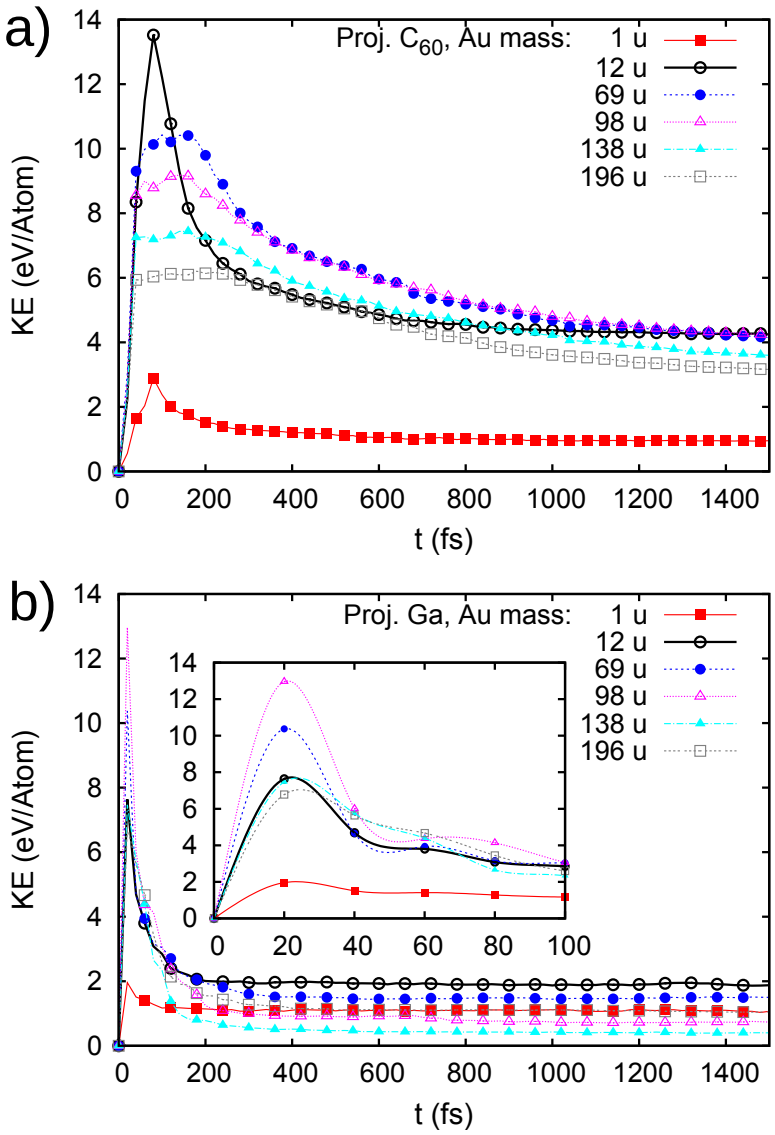

Figure 6.2: (a) Time evolution of the average kinetic energy (KE) of the NP when it is impacted by C_{60} and (b) when it is impacted by Ga. The inset shows the peak maximums in detail.

face. While *Ga* produces fission and fragmentation of the NP due to the stress produced when the projectile goes through it, C_{60} first induces a compression followed by decompression of the two colliding clusters, producing fragments that are finally responsible for the organic emission (see chapter 4).

In the collision process of C_{60} with the NP, the manner in which the fragmentation happens is very important. If the fragments are spread laterally with sufficient energy, the energy can be concentrated in the surface and the emission of the organic sample can be enhanced. In fact, this is the case when the projectile and the target NP have the same atomic masses. The results are illustrated in Figure 6.3.

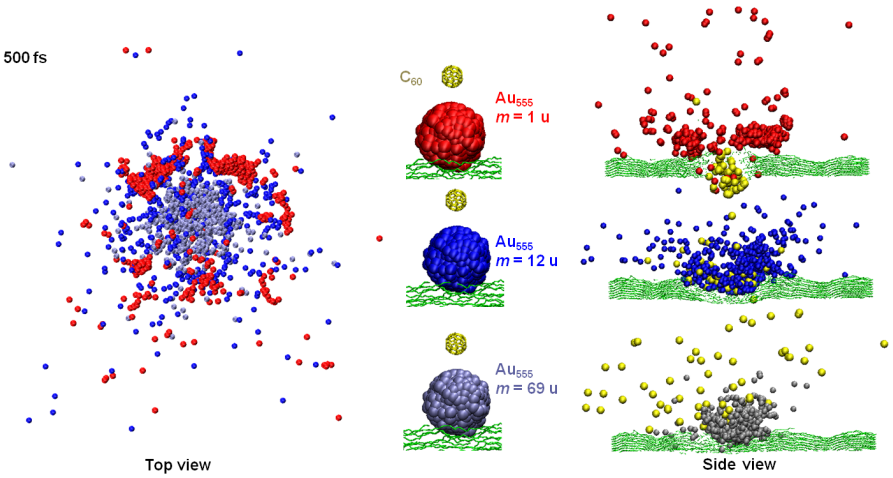

Figure 6.3: Comparison of the C_{60} and Au_{555}-NP collision, when the atomic mass the of NP is $m = 1$ amu (red), $m = 12$ amu (blue) and $m = 69$ amu (gray). Right, side view of the NP fragmentation and reflection of C_{60} at 500 fs, 10 keV. Left, top view of NP fragmentation.

When the atomic mass of the target is less than the atomic mass of the projectile, C_{60} goes through it without significant change of its direction. On the contrary, when the atomic mass of the target is larger than the atomic mass of C_{60}, the atoms of the projectile are reflected. However, if the target and projectile have the same atomic mass, the deflection of colliding atoms and the number of fragments are maximized. In Figure 6.3 the top view clearly shows the maximized number of fragments (dark blue), while the side view shows their maximum dispersion.

6.1.3 Changing the atomic mass of C_{60}

In the second set of simulations, a total of five impacts on bare PE are calculated at 10 keV, changing the atomic mass of the C_{60}. In this set, the considered atomic masses are 14, 69, 98, 138 and 197 amu. Here, to obtain an exact match in projectile-target atomic masses, the carbon mass is replaced by the mass of a CG PE unit, equal to 14 amu. The results are given in the four plots of Figure 6.4. In the top graphs of

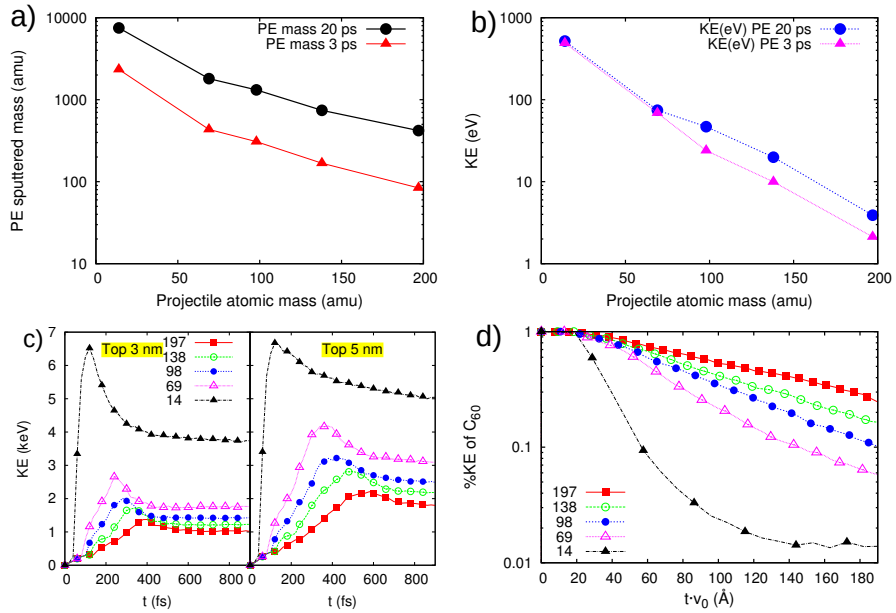

Figure 6.4: Top: comparison of the total sputter PE mass (a) and its kinetic energy (KE) as a function of the C_{60} atomic mass (b) at times of 3 and 20 ps. Bottom: comparison of the KE transferred from C_{60} to the top 3 nm and 5 nm of the PE surface (c). Percentage of kinetic energy ($\%KE$) that the projectile looses as it changes its position in the space, for the first 1.5 ps (d).

Figure 6.4, the sputtered masses and their corresponding kinetic energies have been gathered at 3 ps and 20 ps. Although 3 ps is not sufficient to cover the entire emission process, the results at 20 ps show that the PE emission vs atomic mass keeps almost the same functional form in time. The most striking results from the top graphs of Figure 6.4 are observed when the projectile and the target have the same atomic masses. If atomic masses match, first, the emission is maximum. Second, of the total quantity of ejected fragments after 20 ps, those fragments that leave the system before 3 ps transport ∼95% of the kinetic energy, and they have only ∼30% of the total sputtered mass. This can be confirmed by the respective maximums of sputtered mass in graph 6.4, which are 2338 amu and 7504 amu and for energies, which are 489.995 eV and 519.353 eV, at 3 ps and 20 ps, respectively.

In addition to the total sputtered mass and its respective energy, it is also important to understand how the energy is transferred from the cluster to the target. These results are summarized in the two bottom graphs of Figure 6.4. The bottom-left plots, show the comparison of the energy transfer into to the top 3 nm and 5 nm of PE as a function of

time, for each value of atomic mass. ∼65% of the projectile energy, is transferred in the first 120 fs into the top 3 nm layers when masses are equal. Similar plots for the top 5 nm slab, show that peak maximums increase in all cases except when atomic projectile-target masses match. This indicates that, indeed, most of the energy is deposited into top 3 nm when atomic masses match. In addition, Figure 6.4d, shows the percentage of energy that the projectile looses as it changes its position in space, for the first 1.5 ps (*t-axis* is scaled by the initial velocity). The differences between the slopes in the linear region are clear: when the projectile and target atomic masses match, the energy is transferred in the sample surface. Furthermore, the projectile looses more than ∼95% of its energy in the first 200 fs.

To have a more detailed view of the energy transfer from the projectile to the sample, an additional analysis is given in Figure 6.5. The

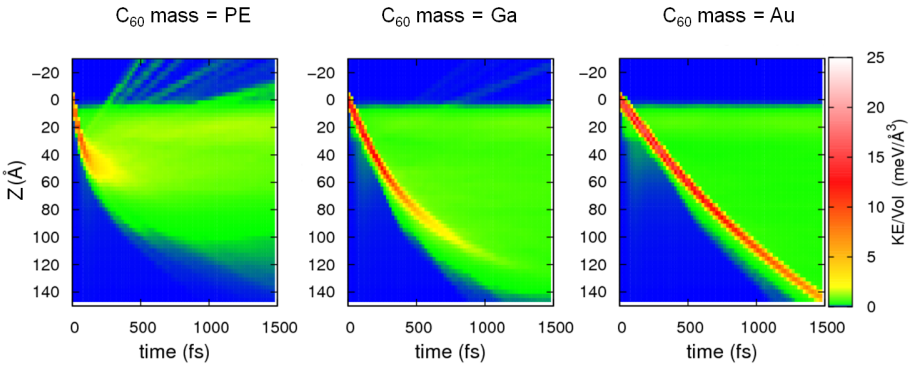

Figure 6.5: Evolution of the kinetic energy per volume of layer (KE/Vol) in the sample for C_{60} impacts at 10 keV on PE as a function of projectile atomic masses: $C_{60} \rightarrow$ PE, $C_{60} \rightarrow Ga$ and $C_{60} \rightarrow Au$. The KE/Vol in each horizontal slab of 3 Å is color-coded from blue to white (color scales on the right).

simulation cell has been sliced in horizontal slabs of 3 Å each, in a similar manner as it was done in Figure 5.11 in the previous chapter. Then, the evolution of the kinetic energy in each slab was monitored as a function of time for the different trajectories. These pictures show that if the atomic mass is increased, the energy tends to remain longer in the projectile. In addition, if the projectile-target atomic masses match, the energy is quickly dissipated on the top layers. In the first femto-seconds, when the transfer of energy is in the linear region, (see in Figure 6.4d) the cluster impact generates an energy wave in the substrate, with an intensity that is proportional to the impact energy. Then after, the wave starts to be damped because no more energy is transferred from the projectile. The lighter rays developing above the sample surface (negative

Z values) indicate the sputtering of PE fragments. This is particularity noticeable for a C_{60} atomic mass equal to 14 amu.

The top pictures of Figure 6.6 compare the C_{60} projectile fragmentation and dispersion when it impacts on PE with atomic mass values equal to PE, *Ga* and *Au* (blue, gray and red respectively). The comparison is made at three different times: 200 fs, 500 and 1000 fs. These pictures show that the maximum dispersion occurs when the projectile and target have the same atomic masses. The bottom frames also indicate the PE damage and crater formation after 1500 fs. Those pictures corroborate and help to explain the results shown in Figure 6.4. When the projectile is heavy, it is implanted deeper and its atoms are not strongly dispersed. Hence, target bonds are only broken in the initial projectile direction. However, as the atomic masses of the projectile and target match, the crater becomes spherical, due to a broad dispersion of the projectile atoms.

Finally, to understand how the atomic mass influences the range of clusters in matter, the ranges of the center of mass (R_{cm}) and of the deepest implanted atom (R_{max}) are plotted in Figure 6.7 as a function of the projectile momentum. The range increases with the atomic mass, in contrast to the decrease of the mass of ejected fragments. The lowest range and highest sputtering yields are therefore observed when the atomic masses of the projectile and the target match. Comparable effects have been observed by Urbassek *et al.* [44] for gold nanoclusters impinging on various materials. The linear function is also in a perfect agreement with the results shown for experiments with cobalt cluster bombardment of graphite made by Popok and co-workers (see in Figure 2.3). [46] It should be noted, that they divided the momentum by the projected surface area of the projectile on the surface, but in our case, this area is a constant because the projectile is always the same.

6.2 Conclusions

The effects of varying the atomic masses of the projectiles and the NPs on an organic surface have been studied in this chapter. Upon impacts on the NP with the C_{60} projectile, the simulations show that the sputter yield of PE rapidly decreases as the atomic mass of the NPs increases, showing a maximum when the atomic masses of projectile and target NP match. Moreover, the maximum NP fragmentation is also observed when atomic masses match. In contrast, for the *Ga* projectile, the simulations have shown that changing the atomic mass of the NPs does not induce a variation of the sputter yield of PE. The NP fragmentation

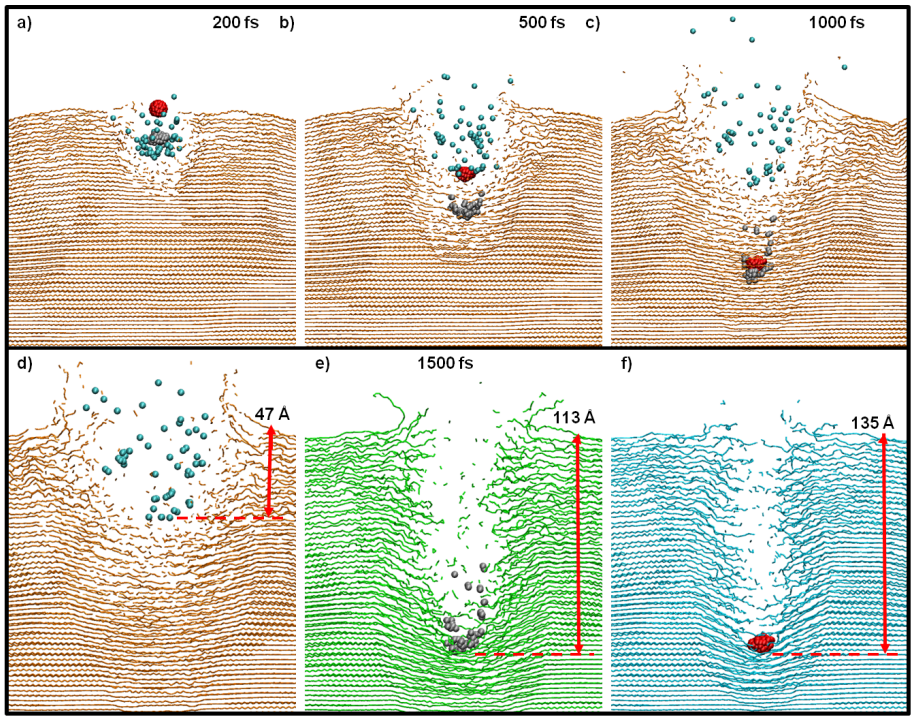

Figure 6.6: Top a), b) and c): comparison of projectile fragmentation when the C_{60} atomic mass is equivalent to the mass of PE (blue), Ga (gray) and Au (red) at three different times. Only the damage by blue projectile is shown (coffee). Bottom d), e), and f): crater comparison as a function of the three masses at time of 1500 fs.

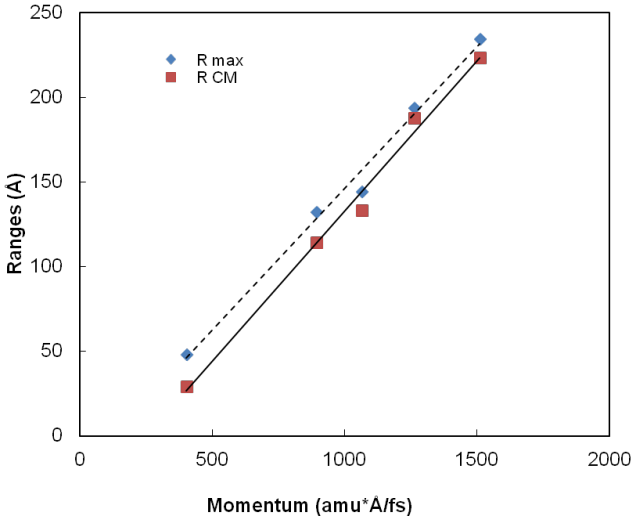

Figure 6.7: Ranges of the center of mass (R_{cm}) and deepest atom implanted (R_{max}) of 10 keV C_{60} clusters with modified atomic masses in a crystalline PE sample as a function of the projectile momentum.

is rather a random process that depends more on the exact impact point. On the other hand, for impacts on PE, it is observed that increasing the atomic mass of C_{60} results in implantation of the projectile and energy loss into the depth of the target, below the sputtering crater. In contrast, atomic masses much smaller for the cluster than the target lead to energy loss via reflection of the projectile constituents. In general, the simulations confirm that the energy is more efficiently transferred to the target when the projectile-target atomic mass ratio is equal to one. This concept explains why C_{60} efficiently transfers the energy in organic surfaces. The fact that atomic mass ratio be one implies a maximized dispersion and energy transfer.

Chapter 7

Conclusions and perspectives

Throughout this thesis, a fundamental and theoretical study of hybrid metal-organic systems in the framework of the sputtering process by keV projectiles have been conducted. Two different samples have been chosen and modeled using classical molecular dynamics. The first one, a metal coated organic system, has provided much insight into the fundamentals of the MetA-SIMS method; while the second, a bulk sample with a metal-organic interface, has been used to obtain complementary information. The results were compared with experimental observations and with other computational studies from the literature.

This research has been focused on the advantages and drawbacks of surface metalization for organic sample sputtering. Special attention has been given to the influence of the metal NPs in the formation of the sputtered organic species yield by different projectiles. Ga, C_{60}, Au, Au_n and Ar_n projectiles have been used to bombard the surface in a systematic way. The sputter yields of organic and metal NP fragments have been compared in different manners, as a function of the impact point, nature of the projectile, projectile energy, and atomic mass ratio of the projectile and target. Also, the variation of the initial conditions, has permitted to compare, the damage produced in the target, the crater size, the origin of yield, ranges, pressure waves, the energy given into the top layers, etc.

The most important results are summarized hereafter:

- When Ga bombards the Au-NPs it creates energetic recoils, and produces a collision cascade. Energetic gold recoil atoms efficiently transfer their energy to the PE surface by developing an extended collision cascade which results in high sputtering yields. Instead, Ga often channels deeply into the surface on pure PE.

- When C_{60} bombards the Au-NP, a significant part of the energy

is reflected due to the mass difference between C and Au. Consequently, the energy is not efficiently transferred to the organic material. In addition, the energy of the recoil Au atoms is too low to induce polymer fragmentation. Hence organic emission is low.

- Au and Au_3 produce higher fragmentation of the Au-NP. The energy is efficiently transferred to the polymer. However, for all the impacts, the PE emission yield remains lower than the sputter yield produced by C_{60} impacts on bare PE.

- Despite the differences of behavior observed for Ga, Au, Au_3 and C_{60} projectiles, the mass spectra of the sputtered fragments have similar shapes. The observed distribution of fragments are in agreement with experiments.

- Impacts of Au_{400} on PE produce few fragments, and as the projectile energy increases, the projectile implants deeper. On the other hand, impacts at low energies with Au_{400} on the NP splashes both the projectile and the NP, and little PE emission is observed. However, at high energy, Au_{400} is destroyed upon impact. Atoms are spread over the PE surface, producing a lot of broken bonds and a large PE yields. In general, impacts on the NP produce larger PE fragments than impacts on PE.

- A comparison of C_{60}, Au_3 and Au_{400} shows that, the sputtered mass of PE is proportional to the projectile energy deposited in the top 3 nm PE layers. The constant of proportionality is similar for C_{60} and Au_3 but smaller for Au_{400}.

- At high energies, Ar_{400} produces more PE emission than Au_{400}. For example, 20 keV Ar_{400} produces 4 times more yield for impact on the NP, and 18 times more for impacts on PE.

- The sputtered mass induced by Ar_n impacts on the metal coated surface shows a strong dependence on the relative sizes of the projectile and target NPs. Those simulations suggest that, to guarantee a projectile size close to the average size of the metal NPs could help to maximize the sputtered organic yield.

- Sputtering of large intact molecules of PE by impacts of low energies with Ar_{2000} is difficult due to the large plasticity of the organic material.

- Ar_n clusters produce emission from the top layers of the surface, in a similar manner as C_{60}. Thus, Ar_n can be considered as well suited as C_{60} for surface analysis.

- Our results show that, the atomic mass matching of the projectile and target lead to a more efficient energy transfer in the surface and larger sputtering yields.

- In general, for heavy cluster projectiles, if the energy per atom is higher than the cohesive energy of the projectile and of the adsorbed NPs, the impacts on the NPs increases the stopping power and enhance the organic sputter yield.

A critical fact in the study of the sputter yield is the number of trajectories needed to have a good statistics, to be in a better agreement with the experiments. Unfortunately, in most of the simulations only one impact was computed. Still, in some cases a few additional simulations were performed and the statistics was considered. For instance, it is well known that the sputter yield produced by cluster projectiles shows small fluctuations, while large fluctuations are observed for atomic ones. [53] This fact was corroborated here for different impacts computed over the bare organic surface. However, in the metal coated surface, when impacts were over the NPs, the sputter yield has shown to be highly sensitive to the exact impact point. In addition to the poor statistics of the impact points, the error introduced by the coarse grain approach and the small size of the sample at high energy impacts, constitute the main drawbacks of this work. Nevertheless, the large difference observed between impacts on PE and on NPs justify the results found.

Beyond these issues, some of the result might constitute a guide for experimentalist, showing the relevant parameters - as for example in MetA-SIMS - and how to modify them according to the experimental aims. In particular we note that, (1) the match of the projectile and target atomic masses and, (2) the match of the projectile and NP sizes, help to enhance the sputter yield. (3) For projectiles made of heavier elements than carbon, one way to deposit more energy in the surface, not tested here, would be to increase the incidence angle. (4) For massive clusters (Au_{400}), energies beyond 10 keV are in the range of the sputtering threshold, therefore, higher energies are recommended. (5) Kiloelectronvolt Au-NPs can be implanted in the subsurface of soft organic materials and the energy-range relationship established for Au_{400} clusters provides a chart for the experimentalist. (6) All the tested clusters are able to desorb Au-NPs from the surface through pressure waves, which might be a way to measure NP size distributions provided that

they become ionized. (7) The extent of the sputtering yield variation observed in the MD between impacts on the bare polymer and on the NPs is insufficient to explain the SIMS results. Therefore, a significant effect of the ionization is expected. Beyond sputtering, experimentalists should continue to focus on improving ionization.

In this thesis, a higher level of understanding of the process of sputtering of metal-organic systems has been gained, yet there is still much work to be done. Thus, some *perspectives* for future work are:

- To study other organic samples.
- To use a full atomistic representation for some short simulations to corroborate some of the results and to compare the differences.
- To study the organic interactions with other metals.
- To implement better potentials than Lennard-Jones for the description of the metal organic interactions.
- To study the metal-organic interface using other angles and other energies.
- To do additional studies of the cluster formation in the surface.
- To explore more systematically generic laws for sputtering (and ionization), as it was mentioned in the equation (2.7) on page 16.
- To study the ionization using *ab initio* methods.
- A huge challenge is to find a way to introduce the ionization into molecular dynamics simulations.

Regardless of the work made throughout this thesis, still more research is needed in this field to find the best conditions to enhance the secondary ion emission in SIMS and gain more insights into metal-organic systems.

Appendix A

Relationship between atomic mass and cohesive energy

In Chapter 6, the effects of artificially changing the masses of the projectile and the NPs have been analyzed. However, other authors have already discussed the effects of changing the cohesive energy [44], which is closely related to changing the masses. Although mass and cohesive energy are conceptually different, they are tied to the manner in which the differential equations of motion integrate. In a system where all particles are of the same type, the motion of each particle is described by the Newton equation

$$m\ddot{\mathbf{r}} = \mathbf{F} = D\mathbf{f}(\mathbf{r}), \tag{A.1}$$

where the cohesive energy D is explicitly written in the force, and $\mathbf{f}(\mathbf{r})$ is usually a conservative function, or

$$\mathbf{f}(\mathbf{r}) = -\nabla_{\mathbf{r}}\phi(\mathbf{r}, \mathbf{r}', \ldots \mathbf{r}^{\mathbf{N}}). \tag{A.2}$$

For instance, in the simple Lenard Jones potential (2.27), D is equivalent to ϵ, and $V_{LJ} = \epsilon\phi$ with potential function ϕ given by

$$\phi(r) = 4\left[\left(\frac{\sigma}{r}\right)^{12} - \left(\frac{\sigma}{r}\right)^{6}\right] \text{ with } r = |\mathbf{r} - \mathbf{r}'|. \tag{A.3}$$

Now, if we consider

$$\ddot{\mathbf{r}} = (D/m)\mathbf{f}(\mathbf{r}) \tag{A.4}$$

either to change the inverse of the mass m, or to change D will produce the same results, i.e., if (D/m) is varied in any interval by multiplying it by any positive parameter, the results can be interpreted as function of a variation of the dissociation energy, or a variation of the mass. However,

this situation does not hold when the projectile and target are composed of different kinds of particles. For instance, consider a system with many types of different atoms, which implies different interactions and different masses between them. In this case, for each particle (atom or particles entities if the coarse grain approximation is used), we have the equation

$$m_a\ddot{\mathbf{r}} = D_{aa}\mathbf{f}_{aa}(\mathbf{r}) + D_{ab}\mathbf{f}_{ab}(\mathbf{r}) + [D_{ac}\mathbf{f}_{ac}(\mathbf{r}) + \epsilon_{ac}\mathbf{f}_{ac}^{VdW}(\mathbf{r})] + \dots \quad \text{(A.5)}$$

where the subscripts a, b, c mean the type of particle or entity, D_{xy} is the explicit dissociation energy for each interaction, and $\epsilon_{ac}\mathbf{f}_{ac}^{VdW}(\mathbf{r})$ is the force produced by the VdW interactions between molecules having an intermolecular cohesive energy ϵ_{ac}. Here, if we change the mass of one type of atom or particle, for example the atom a, the ratio (D_{ax}/m_a) will change. This situation clearly differs from the previous one in which all the particles are of the same type (equation (A.1)). In (A.5), to change the mass means to vary at the same time, all the D_{xy}, and not only to vary D_{aa}. Moreover, if potentials include the contribution to the rotational and the binding energies, they will be also affected by the variation of the mass. In general, changing the mass affects the interaction of one particle with each of the others, while changing the dissociation energy only alters one particular type of interaction.

Appendix B

Some additional comments on sputtering yield and energies

Upon impact part of the energy escapes into the vacuum with the sputtered particles or fragments. This energy can give important information of the sputtering process. Therefore, the kinetic energies of the total sputter fragments for impacts on NP and impacts on PE (see in Figure 4.1 on page on page 57) are compared in the plots of Figure B.1. Each of the distributions include all the fragments of gold, PE, and remains of the projectiles, that are moving into the vacuum at 30 ps. Intensities are calculated considering the total number of fragments with energy between $(E, E + dE)$. All the plots are normalized to their respective maximums and the same $dE = 0.2$ eV is considered. For all the simulations, impacts on NP seem to produce fragments that move with more kinetic energy than the fragments from the impacts on PE. This fact can also be corroborated if the maximum kinetic energy, KE_{max}, of the fragments is computed and compared for both kinds of impacts. As a consequence, sputtered fragments of the impacts on NP transport additional kinetic energy (see KE_T giving the total energy, in table insets). The distribution is also wide with C_{60} impacts on PE.

The plots of Figure B.2 shows the percentage of the energy taken with the reflection of the C_{60} atoms. Both samples are considered. A comparison of the KE_T given in B.1 for C_{60} with the average over impacts on NP gives approximately the same values, which means that C_{60} impacts on the NP do not transfer efficiently the energy to the target. In this case, the major part of the energy of the sputtered fragments is transported by the remains of the projectile.

Figure B.3 shows in detail the total sputter yield for each impact point used to take the averages of Figure 4.2 on page 59.

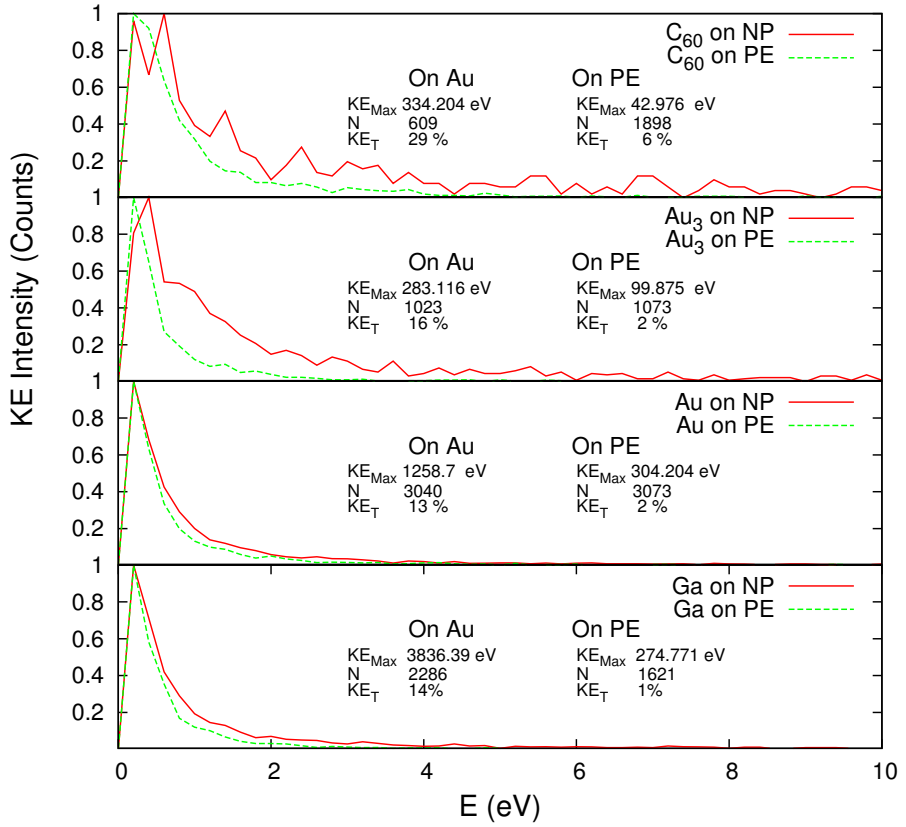

Figure B.1: Comparison of the kinetic energy distributions of the sputter fragments at 10 keV impacts for C_{60}, Au_3, Au and Ga, respectively. In table insets: KE_T is the percentage of kinetic energy of all sputtered fragments (total energy/10 keV×100%), N is the total number of fragments, and KE_{max}, is the maximum kinetic energy reached by any fragment in each case.

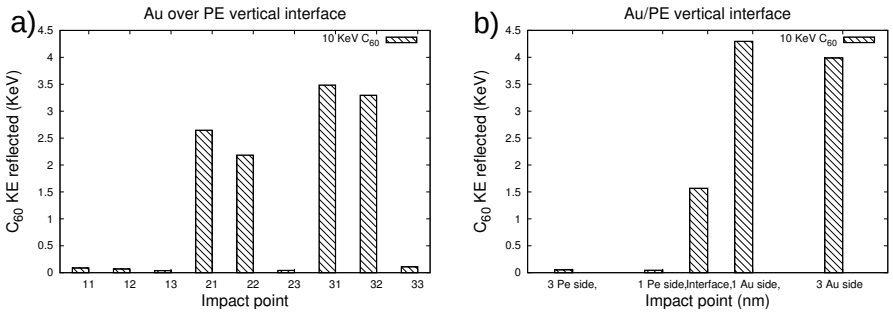

Figure B.2: Percentage of KE reflected with C_{60} at 10 keV impacts. In left *sample A* and in right *sample B*, as it was defined in Section 3.3 on page 48.

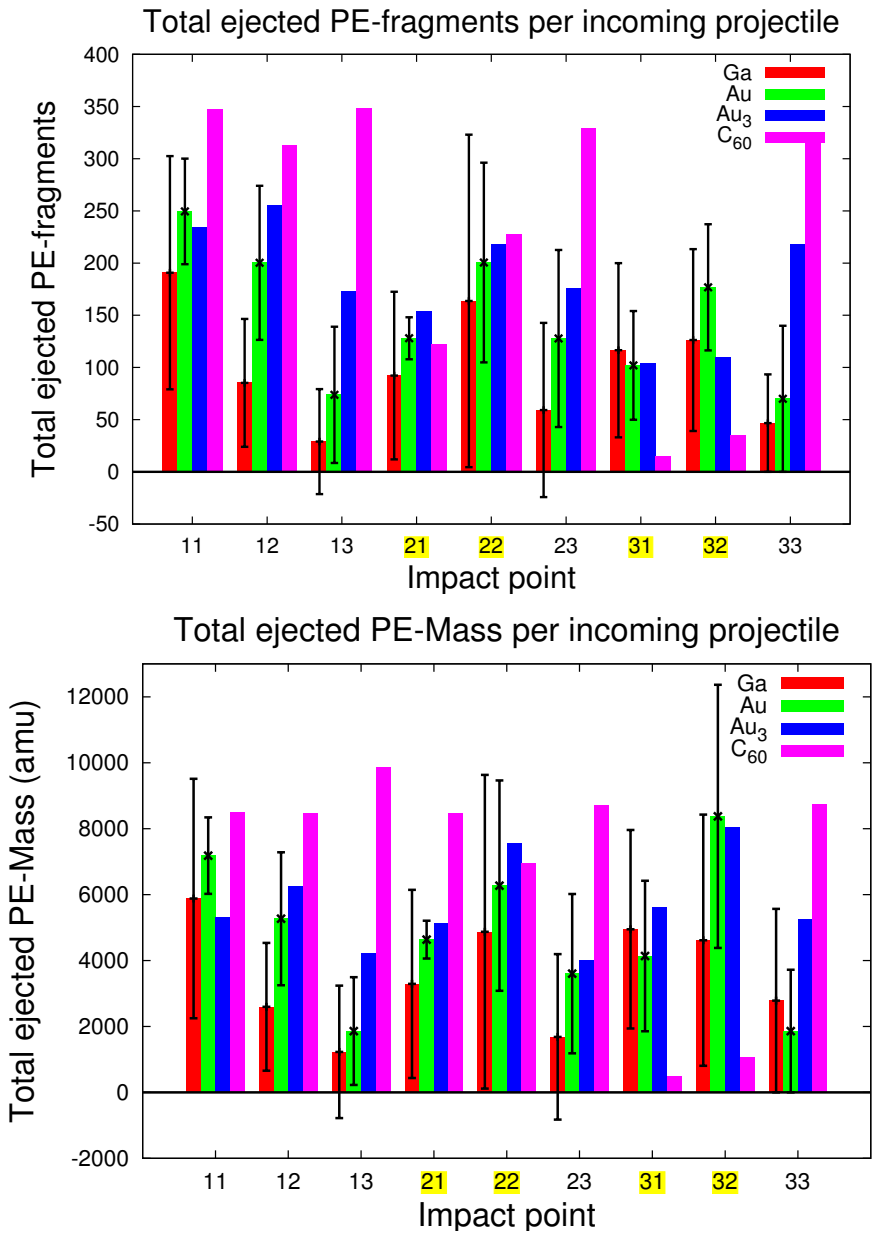

Figure B.3: Histograms of the total emission of PE fragments (top) and mass (bottom) per impact for each projectile as a function of the impact point. Impact points are shown in Figure 4.1 on page 57. Yellow points are impacts on NP.

List of Figures

1.1 (a) Experimental yields of Au^+, $C_7H_7^+$ and Au-cationized PS oligomers measured upon 12 keV Ga^+ bombardment of a thick PS coating, as a function of the fraction of the surface covered by gold. The inset shows the SEM micrograph of the sample surface (200-nm width). (b) and (c) Experimental yields of $C_7H_7^+$ sputtered under 12 keV Ga^+ and C_{60}^+ bombardment of pristine and metal-covered PS coatings (1 and 20 mg/ml PS solution concentrations, and 0.5, 2, 6 nm Au equivalent thicknesses). Figures from ref [25]. 7

2.1 Maximum penetration depth R_{max} of Au_{13} and Au_{402} into graphite at same constant energy of 100 eV/atom. The *Clearing the way* effect can be observed. Taken from Ref [41]. . . . 13

2.2 Ranges of Au_{402} as a function of impact energy per atom. U/U_{Ar} denotes the cohesive energy divided by the cohesive energy of Ar. In a) maximum range, and in b) range of the center of mass. Bottom: maximum ranges as a function of the cohesive energy of the target in c), and ranges of C_{60} on four different targets d). Taken from refs [42, 41]. 14

2.3 In a) MD simulations of the deepest implanted Co atoms vs projected momentum for different clusters sizes, and b) comparison to the corresponding experimental data. Taken from Ref [46]. 15

2.4 Comparison of Ar_{961} cluster impacts with a hard particle impact on carbon diamond structure at an energy E of 100 keV (10 Å cross-section). Taken from Ref [47]. 16

2.5 Sputtering yield in benzene molecule equivalents vs individual aiming points for 15 keV Ga and C_{60} bombardment. From Ref [53]. 18

2.6 Average kinetic electron emission yield as a function of projectile energy for $Ag \rightarrow Ag$ bombardment; model calculations employing both excitation mechanisms (electronic friction + electron promotion, -■-) are compared with the corresponding model calculations that disregard electron promotion processes (-□-); the symbols correspond to experimental data (Lakits *et al.* (⊙), Alonso *et al.* (+)) for $Xe^+ \rightarrow Au$ bombardment. Figure from Ref [56]. 19

2.7 Example of LJ potentials for four different interactions as they are described by the Equation (2.27). The parameters will be used later in Chapter 3 for polyethylene and gold interactions. 29

2.8 Graphs of the repulsive potentials and spline of Molière with the Morse potential in the interval $(r_{min}, r_{max}) = (0.6, 1)$, for the case when $Z_1 = Z_2 = 7$. The Firsov factor f used for the Molière function is $0.69 + 0.0051(Z_1 + Z_2)$, and 1 for the KrC and Universal functions. 38

3.1 Left: two molecular chains, with periodicity in z direction of $c = 2.548$ Å. Right: Ideal orthorhombic unit cell with lattice parameters $a = 7.121$ Å, $b = 4.851$ Å. Only the six atoms inside of box are needed to reproduce the unitary cell. 42

3.2 Cross-sectional view of the temporal evolution of a collision event by 500 eV C_{60} bombardment. The sample size for the CG calculation is $17.03 \times 9.17 \times 16.89$ nm^3 and $17.03 \times 9.86 \times 6.89$ nm^3 for the atomistic calculation implemented with AIREBO potential. A slice of 1.5 nm wide in the center of the system is shown. The atomistic simulation is two layers larger than the CG case. Taken from ref [122] 47

3.3 Sample A is a crystal of PE covered with gold atoms, and sample B is formed by two slabs of gold and PE. Sample C is an amorphous PE structure covered with gold atoms as in sample A. 48

3.4 a) The random deposition of gold over PE gives a fractal structure. In b) islets after 10 ps. c) Second relaxation until 20 ps with the output of the first relaxation, velocities were reset to zero. d) SEM image of polystyrene covered with 2.0 nm equivalent layer thickness of Au, the small box is the equivalent area used in the simulations. (figure, Prabhakaran courtesy). 51

3.5 Structures obtained from three different initial conditions for the relaxation of gold on surface of crystalline PE. Effects in nano-islets formation when: a) the temperature is changed to zero, b) the box size of PE is reduced, and d) the thickness d or the quantity of Au atoms deposited on the surface is increased. 52

3.6 Relaxation with different thicknesses of gold until 10 ps. On bottom right corner, temperature as a function of the time. . . 53

4.1 Relaxed gold-coated PE surface and the amplification of the nine impact points with distance separation of 1 nm. For monoatomic projectiles three additional aiming points have been defined, separated 0.2 nm in x and y directions for statistical reasons. 57

4.2 Histograms of the total emission of PE fragments (top) and mass (bottom) per impact for each projectile. Data are separated in three sets: impacts on the interstitial points between Au-NPs, direct impacts on the Au-NP, and average over all impacts and independently of aiming point. The small inset is the ratio mass/fragments. 59

4.3 Histograms with total ejected Au-fragments for each impact point. 61

4.4 Comparison of the mass spectra. On top, MD simulations for Ga, C_{60}, Au, and Au_3. On bottom, experimental data for Ga and C_{60}. In parenthesis, the corresponding normalization values. The left column is the PE intensity counts while right is Au intensity. 63

4.5 Normalized intensity or number of PE fragments as a function of mass for impacts on the Au-NP (left) and impacts on PE (right). 64

4.6 Data separation depending whether the impacts are on PE or on the Au-NP for each projectile. 64

4.7 Mass spectra of the PE fragments with mass larger than 200 Da. Each graph shows a comparison of the impacts on NP and on PE, for C_{60}, Au_3, Au and Ga, respectively. This part of spectra contains ∼30% of the total mass for impacts on NP, and ∼10% for impacts on PE. 65

4.8 Snapshots of the surface illustrating the origin of the yield produced by C_{60}, Au_3, Ga and Au at $t = 0$. Inset frames are the corresponding side views. Color coding: blue is PE, yellow is gold, the central NP is orange if the impact is on it, else yellow is kept. Green and violet are Au and PE atoms which are going to be ejected at $t = 30$ ps. Projectiles are in red, and pink are the PE chains displaced to the surface to form the crater rim. 67

4.9 Comparison of the craters for C_{60}, Au_3, Ga and Au at 1 ps and 30 ps. Inset frames show the top view of the craters at 30 ps. In frames at 1 ps, Au_n NPs have been attenuated to emphasize the projectile effects over the central NP. Same color coding as in Figure 4.8. 69

4.10 Histograms of the total ejected PE mass for impacts at the Au-NP interface, and 1 nm, 3 nm away from the interface. . . 73

4.11 Histograms of the total ejected gold mass for impacts at the Au-NP interface, and 1 nm, 3 nm away from the interface. . . 73

4.12 Snapshots of 10 keV impacts at 1nm from the interface on Au side for a) C_{60} and b) Ga for the *sample B*. Color coding: the same as in Figure 4.9, but orange are now the Au atoms moving to form the rim on surface and highlighted yellow the Au atoms implanted into PE (see the arrows). 74

4.13 Impacts of C_{60} on PE (a) and Au_3 on gold (b), both at 1 nm of the interface. On top, side view, and on bottom, top view of the crater and sputtering mechanism at 1ps. Small insets are the side views at time zero showing the origin of sputtered PE. Color coding: the same as in Figures 4.9 and 4.12. 75

4.14 Total ejected PE mass in sample A (left) and sample B (right) for different impact points and projectiles (Ga and C_{60}). The insets show top-down views of the center of the samples with the considered aiming points. 76

4.15 Top view of the crater formation as a function of the energy transfer for 10 keV impacts of C_{60} (left) and Au_3 (right) on the interface. Insets: side view at time $t = 0$ ps showing the origin of sputtered PE. Color coding: the same as in Figures 4.9 and 4.12. 79

5.1 PE sputtered mass as a function of the maximum kinetic energy reached in the top 3 nm of the polymer surface for 10 keV initial bombardment. The colors relate to the impact points and the labels to the projectiles. 83

5.2 a) 10 keV C_{60} and b) Au_{400} projectile impacts over PE. The colored target layers are ∼1 nm each. Au-NPs are omitted for clarity. 84

5.3 Au_{555} cluster fragmentation upon direct impact of 10 keV C_{60}, Au_3 and Au_{555} projectiles (from left to right). Top frames: 1.5 ps; Bottom frames: 30 ps. Color coding: yellow, central Au-NP; green, gold ejected from the central Au-NP; grey, other gold NPs; orange, PE; red, projectile. 86

5.4 Amorphous PE with NPs on the surface (top) and NPs buried (bottom). Au_{400} impacts are on Au_{555} recycle from crystal structure. Frames taken from the master thesis of Van Hoecke. [136] 88

5.5 (a) 3D perspective view of the simulation cell after sample relaxation and before the bombardment. Configuration with the central Au_{555} NP (gray) and the Au_{400} projectile on top (red). The other Au atoms are in yellow and the PE coarse-grained units are in orange. (b) Top view of the same cell indicating the impact point. For impacts on PE, the gray NP is removed. 90

5.6 (a) Sputtered masses of PE fragments for impacts on PE and direct hits on the Au_{555} NP. (b) Sputtered masses of gold for the same conditions. Full symbols are for Au_n clusters with $n<10$ and open symbols represent the total sputtered gold mass, including entire NP desorbed at much later times. 90

5.7 Yield distribution of PE fragments (number of fragments per impact as a function of mass). Impact on PE at 40 keV is compared to impacts on the central Au_{555} NP at 20, 30 and 40 keV. 91

5.8 Average depth of origin of the sputtered PE fragments (Z_{av}) and Z coordinate of the deepest sputtered fragment (Z_{max}) as a function of the projectile energy for (a) impacts on PE and (b) impacts on the Au_{555} NP. The depths are calculated with respect to the Au-PE interface. 92

5.9 Cross-sections of the target at the time of maximum penetration for impacts at 40 keV, (a) on PE and (b) on the Au_{555} NP. The central insets show the origin of the PE fragments (purple) for each case. The left inset shows the effect of "peeling off" of the projectile (red outer shell and yellow core) at 1.5 ps. The vertical distances are calculated with respect to the Au-PE interface. 93

5.10 On top evolution of the vertical coordinates of the center of mass (CM) as a function of time for impacts (a) on PE and (b) on the Au_{555} NP. Bottom, pictures (c-d) show the maximum range reached by the projectile center of mass (represented by R_{CM}), and vertical positions of the deepest Au atoms of the projectiles (represented by R_{Max}), for these two types of impacts. The vertical distances are calculated with respect to the Au-PE interface. 94
5.11 Evolution of the kinetic energy per volume of layer KE/Vol in the sample for impacts at 5 keV (a-b) and 40 keV (c-d). The left column corresponds to impacts on PE and the right column to impacts on the Au_{555} NP. The KE/Vol in each horizontal slab of 3 Å is color-coded from blue to white (color scales on the right). The time resolution is 50 fs for the first 2000 fs and 500 fs afterwards. The vertical distances are calculated with respect to the Au-PE interface. 95
5.12 Fraction of the projectile energy (E_{3L}/E_0) transferred to the top 30 Å of the target as a function of the projectile energy. . 97
5.13 Time-evolution of the energy per atom for the projectile Au_{400} (E_P), the surface NP Au_{555} (K_T) and the combination of both Au_{555} + Au_{400} (K_{P+T}). The color coding indicates the projectile energy. Inset: microscopic view of the situation at the maximum of K_T for 40 keV bombardment. Atoms of the Au_{400} projectile are in red and atoms of the surface Au_{555} NP are in yellow. 100
5.14 Time-evolution of the potential energy per atom (E_p) for the projectile Au_{400} and the surface NP Au_{555} (40 keV impact). The green curve (K_{PE}) describes the kinetic energy in the cylinder of PE under the impact point (16 Å radius and 30 Å depth). 100
5.15 Comparison total PE sputtered mass of impacts on PE, and on Au-cluster on the surface. 103
5.16 PE sputtered mass as a function of number of atoms n (top) and radius R (bottom) of the projectile. 103
5.17 20 keV Ar_n projectiles. At the top of the Figure: impacts on Au_{555}-NP over PE. At the bottom: impacts over PE. Color code: pink is PE; cyan and yellow are the projectile and Au-NPs, respectively; the target NP is in dark blue. 106
5.18 Number of ejected Au fragments as a function of energy (a), and Au fragments per number of atoms in the projectile as a function of the energy per Ar atom (b). Impacts are on the Au-NP. 106

5.19 Ar_{2000} 10 keV impacts using different border conditions. Border effects on emission of large PE chains of 2.8 kDa. Color code: the same as in Figure 5.18 but here pink and brown are the vertical and top horizontal slides of PE, respectively. . . . 108

6.1 Sputtered mass and emission yield of PE fragments when impacts are over NP as a function the NP mass after 30 ps. The impact energy is 10 keV. Data are compared with the interval of emission of the C_{60} impacts over a bare area of the PE surface. 113

6.2 (a) Time evolution of the average kinetic energy (KE) of the NP when it is impacted by C_{60} and (b) when it is impacted by Ga. The inset shows the peak maximums in detail. 115

6.3 Comparison of the C_{60} and Au_{555}-NP collision, when the atomic mass the of NP is $m = 1$ amu (red), $m = 12$ amu (blue) and $m = 69$ amu (gray). Right, side view of the NP fragmentation and reflection of C_{60} at 500 fs, 10 keV. Left, top view of NP fragmentation. 116

6.4 Top: comparison of the total sputter PE mass (a) and its kinetic energy (KE) as a function of the C_{60} atomic mass (b) at times of 3 and 20 ps. Bottom: comparison of the KE transferred from C_{60} to the top 3 nm and 5 nm of the PE surface (c). Percentage of kinetic energy ($\%KE$) that the projectile looses as it changes its position in the space, for the first 1.5 ps (d). 117

6.5 Evolution of the kinetic energy per volume of layer (KE/Vol) in the sample for C_{60} impacts at 10 keV on PE as a function of projectile atomic masses: $C_{60} \rightarrow$ PE, $C_{60} \rightarrow Ga$ and $C_{60} \rightarrow Au$. The KE/Vol in each horizontal slab of 3 Å is color-coded from blue to white (color scales on the right). 118

6.6 Top a), b) and c): comparison of projectile fragmentation when the C_{60} atomic mass is equivalent to the mass of PE (blue), Ga (gray) and Au (red) at three different times. Only the damage by blue projectile is shown (coffee). Bottom d), e), and f): crater comparison as a function of the three masses at time of 1500 fs. 120

6.7 Ranges of the center of mass (R_{cm}) and deepest atom implanted (R_{max}) of 10 keV C_{60} clusters with modified atomic masses in a crystalline PE sample as a function of the projectile momentum. 120

B.1 Comparison of the kinetic energy distributions of the sputter fragments at 10 keV impacts for C_{60}, Au_3, Au and Ga, respectively. In table insets: KE_T is the percentage of kinetic energy of all sputtered fragments (total energy/10 keV×100%), N is the total number of fragments, and KE_{max}, is the maximum kinetic energy reached by any fragment in each case. 130
B.2 Percentage of KE reflected with C_{60} at 10 keV impacts. In left *sample A* and in right *sample B*, as it was defined in Section 3.3 on page 48. 130
B.3 Histograms of the total emission of PE fragments (top) and mass (bottom) per impact for each projectile as a function of the impact point. Impact points are shown in Figure 4.1 on page 57. Yellow points are impacts on NP. 131

List of Tables

2.1 Threshold energies above which the adiabatic approximation is no longer valid. They are calculated by using the simple kinetic energy definition $E_0 = 1/2mv^2$, where m is the mass of the projectile, and $v = 10^8$ m/s. 26

3.1 Relative error of mass of PE fragments $(m/14n) \times 100$ % in the CG approach ($C_nH_{2n\pm m} \approx C_nH_{2n}$). The error is calculated over the maximum number m of hydrogen atoms that can be ignored in the fragmentation process of one chain for each fragment (third column). Only the 4 H in the two ends of the fragment are considered. 46

4.1 Comparison of the results on gold coated amorphous PE and PE crystal. Mass of gold and PE (kDa) sputtered from sample upon 10 keV, Ga and C_{60} bombardment. The results from amorphous sample are taken from the master thesis of Van Hoecke. [136] 71

5.1 Mass of gold and PE (kDa) sputtered from sample upon 10 keV C_{60}, Au_3 and Au_{400} bombardment after 30 ps. 82

5.2 Comparison of the sputtered mass (kDa) on gold coated amorphous and crystal PE samples upon 10 keV, Au_{400} bombardment. Results of the amorphous PE are taken from the master thesis of Van Hoecke. [136] 87

5.3 Comparison of the total sputtered fragment numbers and mass for Ar_{60} and C_{60} projectiles at the same impact point, obtained by MD simulations. 105

5.4 Comparison of the total number of sputtered fragments and mass for Au_{400}, Ar_{400}, and Ar_{2000} projectiles, obtained by MD simulations. 107

Bibliography

[1] A. Delcorte, N. Médard, and P. Bertrand. Organic secondary ion mass spectrometry: sensitivity enhancement by gold deposition. *Analytical chemistry*, 74(19):4955–68, October 2002. ISSN 0003-2700. URL http://www.ncbi.nlm.nih.gov/pubmed/12380818. 2, 6, 81

[2] L. Adriaensen, F. Vangaever, and R. Gijbels. Metal-assisted secondary ion mass spectrometry: influence of Ag and Au deposition on molecular ion yields. *Analytical chemistry*, 76(22):6777–85, November 2004. ISSN 0003-2700. doi: 10.1021/ac049108d. URL http://www.ncbi.nlm.nih.gov/pubmed/15538803. 2, 81

[3] K. Keune and J. J. Boon. Enhancement of the static SIMS secondary ion yields of lipid moieties by ultrathin gold coating of aged oil paint surfaces. *Surface and Interface Analysis*, 36(13): 1620–1628, 2004. ISSN 0142-2421. doi: 10.1002/sia.1996. URL http://doi.wiley.com/10.1002/sia.1996. 2, 81

[4] Håkan Nygren, Bengt R. Johansson, and Per Malmberg. Bioimaging TOF-SIMS of tissues by gold ion bombardment of a silver-coated thin section. *Microscopy research and technique*, 65(6): 282–6, December 2004. ISSN 1059-910X. doi: 10.1002/jemt.20133. URL http://www.ncbi.nlm.nih.gov/pubmed/15662659. 2, 81

[5] A. Heile, D. Lipinsky, N. Wehbe, A. Delcorte, P. Bertrand, A. Felten, L. Houssiau, J.-J. Pireaux, R. De Mondt, P. Van Royen, L. Van Vaeck, and H. F. Arlinghaus. Investigation of methods to enhance the secondary ion yields in TOF-SIMS of organic samples. *Surface and Interface Analysis*, 40(3-4):538–542, March 2008. ISSN 01422421. doi: 10.1002/sia.2810. URL http://doi.wiley.com/10.1002/sia.2810. 2, 6, 60

[6] J. L. S. Lee, S. Ninomiya, J. Matsuo, I. S. Gilmore, M. P. Seah, and A. G. Shard. Organic depth profiling of a nanostructured delta

layer reference material using large argon cluster ions. *Analytical chemistry*, 82(1):98–105, January 2010. ISSN 1520-6882. doi: 10.1021/ac901045q. URL http://www.ncbi.nlm.nih.gov/pubmed/19957960. 2

[7] Roger P. Webb, Barbara J. Garrison, and John C. Vickerman. The effect of the H:C ratio on the sputtering of molecular solids by fullerenes. *Surface and Interface Analysis*, 43(1-2):116–119, January 2011. ISSN 01422421. doi: 10.1002/sia.3421. URL http://doi.wiley.com/10.1002/sia.3421. 2

[8] Alexander G. Shard, Felicia M. Green, Paul J. Brewer, Martin P. Seah, and Ian S. Gilmore. Quantitative molecular depth profiling of organic delta-layers by C_{60} ion sputtering and SIMS. *The journal of physical chemistry. B*, 112(9):2596–605, March 2008. ISSN 1520-6106. doi: 10.1021/jp077325n. URL http://www.ncbi.nlm.nih.gov/pubmed/18254619. 2

[9] Agnès Tempez, J. A. Schultz, S. Della-Negra, J. Depauw, D. Jacquet, A. Novikov, Y. Lebeyec, M. Pautrat, M. Caroff, M. Ugarov, H. Bensaoula, M. Gonin, K. Fuhrer, and Amina Woods. Orthogonal time-of-flight secondary ion mass spectrometric analysis of peptides using large gold clusters as primary ions. *Rapid communications in mass spectrometry : RCM*, 18(4):371–6, January 2004. ISSN 0951-4198. doi: 10.1002/rcm.1342. URL http://www.ncbi.nlm.nih.gov/pubmed/14966842. 2

[10] Alexey Novikov, Martine Caroff, Serge Della-Negra, Joël Depauw, Mireille Fallavier, Yvon Le Beyec, Michèle Pautrat, J. Albert Schultz, Agnès Tempez, and Amina S. Woods. The Au(n) cluster probe in secondary ion mass spectrometry: influence of the projectile size and energy on the desorption/ionization rate from biomolecular solids. *Rapid communications in mass spectrometry : RCM*, 19(13):1851–7, January 2005. ISSN 0951-4198. doi: 10.1002/rcm.1995. URL http://www.ncbi.nlm.nih.gov/pubmed/15945024. 2

[11] A. Delcorte, S. Yunus, N. Wehbe, N. Nieuwjaer, C. Poleunis, a Felten, L. Houssiau, J.-J. Pireaux, and P. Bertrand. Metal-assisted secondary ion mass spectrometry using atomic (Ga^+, In^+) and fullerene projectiles. *Analytical chemistry*, 79(10):3673–89, May 2007. ISSN 0003-2700. doi: 10.1021/ac062406l. URL http://www.ncbi.nlm.nih.gov/pubmed/17417819. 2, 5, 6, 8, 50, 60

[12] S. Rajagopalachary, S. V. Verkhoturov, and E. A. Schweikert. Examination of nanoparticles via single large cluster impacts. *Nano letters*, 8(4):1076–80, April 2008. ISSN 1530-6984. doi: 10.1021/nl0730716. URL http://www.ncbi.nlm.nih.gov/pubmed/18311935. 3

[13] S. Rajagopalachary, S. V. Verkhoturov, and E. A. Schweikert. Examination of individual nanoparticles with cluster SIMS. *Surface and Interface Analysis*, 43(1-2):547–550, January 2011. ISSN 01422421. doi: 10.1002/sia.3564. URL http://doi.wiley.com/10.1002/sia.3564. 3

[14] L. A. McDonnell and R. M. A. Heeren. Imaging mass spectrometry. *Mass spectrometry*, (October 2006):606– 643, 2007. doi: 10.1002/mas. URL http://igitur-archive.library.uu.nl/chem/2008-0229-201047/UUindex.html. 3

[15] A. Benninghoven, F. G. Rudenauer, and H. W. Werner. *Secondary Ion Mass Spectrometry: Basic Concepts, Instrumental Aspects, Applications and Trends (Chemical Analysis)*. John Wiley & Sons, 1987. ISBN 0471010561. URL http://www.amazon.com/Secondary-Ion-Mass-Spectrometry-Instrumental/dp/0471010561. 4

[16] John C. Vickerman and David Briggs. *ToF-SIMS : Surface Analysis by Mass Spectrometry*. IM Publications LLP, 2001. ISBN 1901019039. URL http://www.amazon.co.uk/ToF-SIMS-Surface-Analysis-Mass-Spectrometry/dp/1901019039. 4, 5, 16, 17, 66

[17] D. S. McPhail. Applications of Secondary Ion Mass Spectrometry (SIMS) in Materials Science. *Journal of Materials Science*, 41(3):873–903, February 2006. ISSN 0022-2461. doi: 10.1007/s10853-006-6568-x. URL http://www.springerlink.com/index/10.1007/s10853-006-6568-x. 4, 5

[18] A. F. Maarten Altelaar, Ivo Klinkert, Kees Jalink, Robert P. J. de Lange, Roger A. H. Adan, Ron M. A. Heeren, and Sander R. Piersma. Gold-enhanced biomolecular surface imaging of cells and tissue by SIMS and MALDI mass spectrometry. *Analytical chemistry*, 78(3):734–42, February 2006. ISSN 0003-2700. doi: 10.1021/ac0513111. URL http://www.ncbi.nlm.nih.gov/pubmed/16448046. 4

[19] R. Heeren, L. McDonnell, E. Amstalden, S. Luxembourg, A. Altelaar, and S Piersma. Why dont́ biologists use SIMS? A critical evaluation of imaging MS. *Applied Surface Science*, 252(19): 6827–6835, July 2006. ISSN 01694332. doi: 10.1016/j.apsusc.2006.02.134. URL http://linkinghub.elsevier.com/retrieve/pii/S0169433206004351. 4

[20] P. Bertrand. Molecular SIMS for organic layers: new insights. *Applied Surface Science*, 203-204:160–165, January 2003. ISSN 01694332. doi: 10.1016/S0169-4332(02)00722-5. URL http://linkinghub.elsevier.com/retrieve/pii/S0169433202007225. 5

[21] A. Delcorte. On the road to high-resolution 3D molecular imaging. *Applied Surface Science*, 255(4):954–958, December 2008. ISSN 01694332. doi: 10.1016/j.apsusc.2008.05.111. URL http://linkinghub.elsevier.com/retrieve/pii/S0169433208011392. 5

[22] Ylva Magnusson. Identification and imaging of lipids in tissues using TOF-SIMS. *Medicine*, 2008. URL http://gupea.ub.gu.se/handle/2077/17683. 5

[23] N. Wehbe, A. Arlinghaus H. Delcorte, A. Heile, and P. Bertrand. Molecular ion yield enhancement induced by gold deposition in static secondary ion mass spectrometry. *Applied Surface Science*, 255(4):824–827, December 2008. ISSN 01694332. doi: 10.1016/j.apsusc.2008.05.068. URL http://linkinghub.elsevier.com/retrieve/pii/S0169433208009884. 6, 58, 81

[24] Nimer Wehbe, Taoufiq Mouhib, Aneesh Prabhakaran, Patrick Bertrand, and Arnaud Delcorte. Influence of the organic layer thickness in (metal-assisted) secondary ion mass spectrometry using Ga^+ and C_{60}^+ projectiles. *Journal of the American Society for Mass Spectrometry*, 20(12):2294–303, December 2009. ISSN 1879-1123. doi: 10.1016/j.jasms.2009.08.022. URL http://www.ncbi.nlm.nih.gov/pubmed/19811931. 6

[25] O. Restrepo, A. Prabhakaran, K. Hamraoui, N. Wehbe, S. Yunus, P. Bertrand, and A. Delcorte. Mechanisms of metal-assisted secondary ion mass spectrometry: a mixed theoretical and experimental study. *Surface and Interface Analysis*, 42(6-7):1030–1034, February 2010. ISSN 01422421. doi: 10.1002/sia.3203. URL http://doi.wiley.com/10.1002/sia.3203. 6, 7, 133

[26] A. Prabhakaran, S. Yunus, N. Wehbe, P. Bertrand, and A. Delcorte. Secondary ion yield enhancement in organic samples due to Au/Pt nanoparticle condensation and their substrate effects. *Surface and Interface Analysis*, 43(1-2):74–77, January 2011. ISSN 01422421. doi: 10.1002/sia.3477. URL http://doi.wiley.com/10.1002/sia.3477. 6

[27] V. Kotál and P. Slepička. Gold coating of polyethylene modified by argon plasma discharge. *Polymer*, 2006. doi: 10.1002/pen. URL http://onlinelibrary.wiley.com/doi/10.1002/pen.20606/abstract. 6, 50

[28] Vladimír Kotál, Václav Švorčík, Petr Slepička, Petr Sajdl, Olga Bláhová, Pavol Šutta, and Vladimír Hnatowicz. Gold Coating of Poly(ethylene terephthalate) Modified by Argon Plasma. *Plasma Processes and Polymers*, 4(1):69–76, January 2007. ISSN 16128850. doi: 10.1002/ppap.200600069. URL http://doi.wiley.com/10.1002/ppap.200600069. 6

[29] Roberto Rozas and Thomas Kraska. Formation of metal nanoparticles on and in polymer films investigated by molecular dynamics simulation. *Nanotechnology*, 18(16):165706, April 2007. ISSN 0957-4484. doi: 10.1088/0957-4484/18/16/165706. URL http://stacks.iop.org/0957-4484/18/i=16/a=165706. 6

[30] F. M. Green, A. G. Shard, I. S. Gilmore, and M. P. Seah. Analysis of the interface and its position in C60(n+) secondary ion mass spectrometry depth profiling. *Analytical chemistry*, 81(1):75–9, January 2009. ISSN 1520-6882. doi: 10.1021/ac801352r. URL http://www.ncbi.nlm.nih.gov/pubmed/19117445. 8

[31] Paolo Mazzoldi. *Ion Beam Modifications of Insulators (Beam Modification of Materials)*, pages 1–56. Elsevier Science Ltd, 1987. ISBN 044442816X. URL http://www.amazon.com/Beam-Modifications-Insulators-Modification-Materials/dp/044442816X. 10

[32] A. Benninghoven, F. G. Rudenauer, and H. W. Werner. *Secondary Ion Mass Spectrometry: Basic Concepts, Instrumental Aspects, Applications and Trends (Chemical Analysis)*, pages 9–10. John Wiley & Sons, 1987. ISBN 0471010561. URL http://www.amazon.com/Secondary-Ion-Mass-Spectrometry-Instrumental/dp/0471010561. 10

[33] James Ziegler. Particle interactions with matter, April 2009. URL http://www.srim.org/. http://www.srim.org/. 10, 12, 17

[34] Peter Sigmund. *Particle Penetration and Radiation Effects*, volume 151 of *Springer Series in Solid-State Sciences*. Springer-Verlag, Berlin/Heidelberg, 2006. ISBN 3-540-31713-9. doi: 10.1007/3-540-31718-X. URL http://www.springerlink.com/index/10.1007/3-540-31718-X. 11

[35] A. Benninghoven, F. G. Rudenauer, and H. W. Werner. *Secondary Ion Mass Spectrometry: Basic Concepts, Instrumental Aspects, Applications and Trends (Chemical Analysis)*, pages 20–31. John Wiley & Sons, 1987. ISBN 0471010561. URL http://www.amazon.com/Secondary-Ion-Mass-Spectrometry-Instrumental/dp/0471010561. 11

[36] Paolo Mazzoldi. *Ion Beam Modifications of Insulators (Beam Modification of Materials)*, pages 651–740. Elsevier Science Ltd, 1987. ISBN 044442816X. URL http://www.amazon.com/Beam-Modifications-Insulators-Modification-Materials/dp/044442816X. 11

[37] John C. Vickerman and David Briggs. *ToF-SIMS : Surface Analysis by Mass Spectrometry*, pages 139–160. IM Publications LLP, 2001. ISBN 1901019039. URL http://www.amazon.co.uk/ToF-SIMS-Surface-Analysis-Mass-Spectrometry/dp/1901019039. 12

[38] Paolo Mazzoldi. *Ion Beam Modifications of Insulators (Beam Modification of Materials)*. Elsevier Science Ltd, 1987. ISBN 044442816X. URL http://www.amazon.com/Beam-Modifications-Insulators-Modification-Materials/dp/044442816X. 12

[39] V. Shulga, M. Vicanek, and P. Sigmund. Pronounced nonlinear behavior of atomic collision sequences induced by keV-energy heavy ions in solids and molecules, April 1989. ISSN 0556-2791. URL http://link.aps.org/doi/10.1103/PhysRevA.39.3360. 12, 92

[40] V. Shulga and P. Sigmund. Penetration of slow gold clusters through silicon. *Nuclear Instruments and Methods in Physics Research Section B: Beam Interactions with Materials and Atoms*, 47(3):236–242, May 1990. ISSN 0168583X. doi: 10.1016/0168-583X(90)90751-F. URL http://linkinghub.elsevier.com/retrieve/pii/0168583X9090751F. 12, 92

[41] C. Anders and H. Urbassek. Cluster-size dependence of ranges of 100eV/atom Au_n clusters. *Nuclear Instruments and Methods in Physics Research Section B: Beam Interactions with Materials and Atoms*, 228(1-4):57–63, January 2005. ISSN 0168583X. doi: 10.1016/j.nimb.2004.10.023. URL http://linkinghub.elsevier.com/retrieve/pii/S0168583X04010845. 13, 14, 93, 97, 111, 133

[42] S. J. Carroll, P. D. Nellist, R. E. Palmer, S. Hobday, and R. Smith. Shallow implantation of "Size-Selected" Ag clusters into graphite. *Physical review letters*, 84(12):2654–7, March 2000. ISSN 1079-7114. URL http://www.ncbi.nlm.nih.gov/pubmed/11017292. 13, 14, 133

[43] Christian Anders and Herbert M. Urbassek. Dependence of cluster ranges on target cohesive energy: Molecular-dynamics study of energetic Au402 cluster impacts. *Nuclear Instruments and Methods in Physics Research Section B: Beam Interactions with Materials and Atoms*, 266(1):44–48, January 2008. ISSN 0168583X. doi: 10.1016/j.nimb.2007.10.019. URL http://linkinghub.elsevier.com/retrieve/pii/S0168583X07015625. 13

[44] C. Anders, H. Kirihata, Y. Yamaguchi, and H. Urbassek. Ranges and fragmentation behavior of fullerene molecules: A molecular-dynamics study of the dependence on impact energy and target material. *Nuclear Instruments and Methods in Physics Research Section B: Beam Interactions with Materials and Atoms*, 255(1):247–252, February 2007. ISSN 0168583X. doi: 10.1016/j.nimb.2006.11.027. URL http://linkinghub.elsevier.com/retrieve/pii/S0168583X06011190. 14, 111, 112, 119, 127

[45] L. Seminara, P. Convers, R. Monot, and W. Harbich. Implantation of size-selected silver clusters into graphite. *The European Physical Journal D - Atomic, Molecular and Optical Physics*, 29(1):49–56, April 2004. ISSN 1434-6060. doi: 10.1140/epjd/e2004-00011-9. URL http://www.springerlink.com/openurl.asp?genre=article&id=doi:10.1140/epjd/e2004-00011-9. 15

[46] Vladimir N. Popok, Saša Vučković, and Eleanor E. B. Campbell. Stopping of energetic cobalt clusters and formation of radiation damage in graphite. *Physical Review B*, 80(20):1–12, November 2009. ISSN 1098-0121. doi: 10.1103/PhysRevB.80.205419. URL http://link.aps.org/doi/10.1103/PhysRevB.80.205419. 15, 85, 119, 133

[47] Y. Yamaguchi, J. Gspann, and T. Inaba. Large-scale molecular dynamics simulations of high energy cluster impact on a diamond surface. *The European Physical Journal D - Atomic, Molecular and Optical Physics*, 24(1-3):315–318, June 2003. ISSN 1434-6060. doi: 10.1140/epjd/e2003-00155-0. URL http://www.springerlink.com/openurl.asp?genre=article&id=doi:10.1140/epjd/e2003-00155-0. 15, 16, 133

[48] P. Sigmund. Mechanisms and theory of physical sputtering by particle impact. *Nuclear Instruments and Methods in Physics Research*, 27(5):1–20, 1987. URL http://www.sciencedirect.com/science/article/pii/0168583X87900048. 17

[49] Editor et al P. Sigmund, N.H. Tolk. *Inelastic Ion-Surface Collisions*. Academic Press, New York, 1977. 17

[50] Editor Top. Appl. Phys. 47, in: R. Behrisch. *Sputtering by Particle Bombardment I*. Springer, 1981. 17

[51] Editor Top. Appl. Phys. 42, in: R. Behrisch. *Sputtering by Particle Bombardment II*. Springer, 1983. 17

[52] P. Sigmund. Theory of sputtering. I. Sputtering yield of amorphous and polycrystalline targets. *Physical Review*, 184(2):383, 1969. URL http://prola.aps.org/abstract/PR/v184/i2/p383_1. 17

[53] B. J. Garrison and Zbigniew Postawa. Computational view of surface based organic mass spectrometry. *Mass spectrometry reviews*, 27(4):289–315, 2008. doi: 10.1002/mas. URL http://onlinelibrary.wiley.com/doi/10.1002/mas.20165/full. 17, 18, 58, 60, 112, 113, 125, 133

[54] A. Wucher and B. Garrison. Unimolecular decomposition in the sputtering of metal clusters, August 1992. ISSN 0163-1829. URL http://link.aps.org/doi/10.1103/PhysRevB.46.4855. 18, 33

[55] A. Duvenbeck. Computer Simulation of Electronic Excitation in Atomic Collision Cascades. *Naturwissenschaften*, 2007. URL http://duepublico.uni-duisburg-essen.de/servlets/DocumentServlet?id=15347. 18, 40

[56] A. Duvenbeck and B. Weidtmann. Predicting Kinetic Electron Emission in Molecular Dynamics Simulations of Sputtering. *The Journal of Physical*, (1):5715–5720, 2010. URL http://pubs.acs.org/doi/abs/10.1021/jp905923w. 19, 40, 134

[57] R. Webb. What do we want from computer simulation of SIMS using clusters? *Applied Surface Science*, 255(4):1223–1228, December 2008. ISSN 01694332. doi: 10.1016/j.apsusc.2008.05.138. URL http://linkinghub.elsevier.com/retrieve/pii/S0169433208010027. 19, 21

[58] John C. Vickerman and David Briggs. *ToF-SIMS : Surface Analysis by Mass Spectrometry*, pages 223–260. IM Publications LLP, 2001. ISBN 1901019039. URL http://www.amazon.co.uk/ToF-SIMS-Surface-Analysis-Mass-Spectrometry/dp/1901019039. 20, 27

[59] L Verlet. Computer "experiments" on classical fluids. i. thermodynamical properties of lennard-jones molecules. *Physical Review*, 159(1):98–103, 1967. URL http://link.aps.org/doi/10.1103/PhysRev.159.98. 22

[60] Andrew E. DePristo and Horia Metiu. Molecular dynamics simulations of energy flow at a solid surface. New methods using a small number of atoms. *The Journal of Chemical Physics*, 90 (2):1229, 1989. ISSN 00219606. doi: 10.1063/1.456128. URL http://link.aip.org/link/doi/10.1063/1.456128/html. 25

[61] C. L. Brooks and Martin Karplus. Deformable stochastic boundaries in molecular dynamics. *The Journal of Chemical Physics*, 79(12):6312, 1983. ISSN 00219606. doi: 10.1063/1.445724. URL http://link.aip.org/link/doi/10.1063/1.445724/html. 25

[62] R. R. Lucchese and John C. Tully. Trajectory studies of vibrational energy transfer in gas-surface collisions. *The Journal of Chemical Physics*, 80(7):3451, 1984. ISSN 00219606. doi: 10.1063/1.447101. URL http://link.aip.org/link/doi/10.1063/1.447101/html. 25

[63] Max Berkowitz and J. Andrew McCammon. Molecular dynamics with stochastic boundary conditions. *Chemical Physics Letters*, 90(3):215–217, 1982. URL http://www.sciencedirect.com/science/article/pii/0009261482800286. 25

[64] Charles Kittel. *Introduction to Solid State Physics*. Wiley, 2004. ISBN 047141526X. URL http://www.amazon.com/Introduction-Solid-Physics-Charles-Kittel/dp/047141526X. 26, 27, 29

[65] Neil W. Ashcroft. *Solid State Physics*, pages 425–426. Thomson Press Ltd, 2003. ISBN 8131500527. URL http://www.amazon.com/Solid-State-Physics-Neil-Ashcroft/dp/8131500527. 26, 27

[66] A. K. Rappe, C. J. Casewit, K. S. Colwell, W. A. Goddard, and W. M. Skiff. UFF, a full periodic table force field for molecular mechanics and molecular dynamics simulations. *Journal of the American Chemical Society*, 114(25):10024–10035, December 1992. ISSN 0002-7863. doi: 10.1021/ja00051a040. URL http://pubs.acs.org/doi/abs/10.1021/ja00051a040. 30, 35, 45, 50, 102

[67] Philip Morse. Diatomic Molecules According to the Wave Mechanics. II. Vibrational Levels. *Physical Review*, 34(1):57–64, July 1929. ISSN 0031-899X. doi: 10.1103/PhysRev.34.57. URL http://prola.aps.org/abstract/PR/v34/i1/p57_1. 30

[68] R. Lincoln, K. Koliwad, and P. Ghate. Morse-Potential Evaluation of Second- and Third-Order Elastic Constants of Some Cubic Metals, May 1967. ISSN 0031-899X. URL http://link.aps.org/doi/10.1103/PhysRev.157.463. 30

[69] Murray S. Daw and M. I. Baskes. Semiempirical, quantum mechanical calculation of hydrogen embrittlement in metals. *Phys. Rev. Lett.*, 50(17):1285–1288, Apr 1983. doi: 10.1103/PhysRevLett.50.1285. URL http://link.aps.org/doi/10.1103/PhysRevLett.50.1285. 31

[70] Murray S. Daw and M. I. Baskes. Embedded-atom method: Derivation and application to impurities, surfaces, and other defects in metals. *Phys. Rev. B*, 29(12):6443–6453, Jun 1984. doi: 10.1103/PhysRevB.29.6443. URL http://link.aps.org/doi/10.1103/PhysRevB.29.6443. 31

[71] S. M. Foiles, M. I. Baskes, and M. S. Daw. Embedded-atom-method functions for the fcc metals cu, ag, au, ni, pd, pt, and their alloys. *Phys. Rev. B*, 33(12):7983–7991, Jun 1986. doi: 10.1103/PhysRevB.33.7983. URL http://link.aps.org/doi/10.1103/PhysRevB.33.7983. 31

[72] S. M. Foiles, M. I. Baskes, and M. S. Daw. Erratum: Embedded-atom-method functions for the fcc metals cu, ag, au, ni, pd, pt, and their alloys. *Phys. Rev. B*, 37(17):10378, Jun 1988. doi: 10.1103/PhysRevB.37.10378. URL http://link.aps.org/doi/10.1103/PhysRevB.37.10378. 31, 32

[73] M. J. Stott and E. Zaremba. Quasiatoms: An approach to atoms in nonuniform electronic systems. *Phys. Rev. B*, 22(4):1564–1583, Aug 1980. doi: 10.1103/PhysRevB.22.1564. URL http://link.aps.org/doi/10.1103/PhysRevB.22.1564. 31

[74] J. K. Norskov. Covalent effects in the effective-medium theory of chemical binding: Hydrogen heats of solution in the 3d metals. *Phys. Rev. B*, 26(6):2875–2885, Sep 1982. doi: 10.1103/PhysRevB.26.2875. URL http://link.aps.org/doi/10.1103/PhysRevB.26.2875. 31

[75] D. Sanders. SCT89: a computer code for atomic and molecular scattering from clean and adsorbate covered surfaces. *Computer Physics Communications*, 70(3):579–608, July 1992. ISSN 00104655. doi: 10.1016/0010-4655(92)90118-I. URL http://linkinghub.elsevier.com/retrieve/pii/001046559290118I. 32, 33

[76] M. S. Stave, D. E. Sanders, T. J. Raeker, and A. E. DePristo. Corrected effective medium method. V. Simplifications for molecular dynamics and Monte Carlo simulations. *The Journal of Chemical Physics*, 93(6):4413, 1990. ISSN 00219606. doi: 10.1063/1.458724. URL http://link.aip.org/link/?JCPSA6/93/4413/1. 32, 33

[77] A. Wucher and B. J. Garrison. Cluster formation in sputtering: A molecular dynamics study using the MD/MC-corrected effective medium potential, 1996. ISSN 00219606. URL http://link.aip.org/link/JCPSA6/v105/i14/p5999/s1&Agg=doi. 32, 33

[78] Susan Sinnott, Mark Stave, Todd Raeker, and Andrew DePristo. Corrected effective-medium study of metal-surface relaxation. *Physical Review B*, 44(16):8927–8941, October 1991. ISSN 0163-1829. doi: 10.1103/PhysRevB.44.8927. URL http://link.aps.org/doi/10.1103/PhysRevB.44.8927. 33

[79] C.L. Kelchner, D.M. Halstead, L.S. Perkins, N.M. Wallace, and A.E. DePristo. Construction and evaluation of embedding functions. *Surface science*, 310(1-3):425–435, 1994. URL http://www.sciencedirect.com/science/article/pii/0039602894914052. 33

[80] J. Tersoff. New empirical model for the structural properties of silicon. *Physical Review Letters*, 56(6):632–635, February 1986. ISSN 0031-9007. doi: 10.1103/PhysRevLett.56.632. URL http://link.aps.org/doi/10.1103/PhysRevLett.56.632. 33

[81] J. Tersoff. New empirical approach for the structure and energy of covalent systems. *Physical Review B*, 37(12):6991–7000, April 1988. ISSN 0163-1829. doi: 10.1103/PhysRevB.37.6991. URL http://link.aps.org/doi/10.1103/PhysRevB.37.6991. 33

[82] J. Tersoff. Empirical interatomic potential for silicon with improved elastic properties. *Physical Review B*, 38(14):9902–9905, November 1988. ISSN 0163-1829. doi: 10.1103/PhysRevB.38.9902. URL http://link.aps.org/doi/10.1103/PhysRevB.38.9902. 33

[83] J. Tersoff. Modeling solid-state chemistry: Interatomic potentials for multicomponent systems. *Physical Review B*, 39(8):5566–5568, March 1989. ISSN 0163-1829. doi: 10.1103/PhysRevB.39.5566. URL http://link.aps.org/doi/10.1103/PhysRevB.39.5566. 33

[84] G. Abell. Empirical chemical pseudopotential theory of molecular and metallic bonding. *Physical Review B*, 31(10):6184–6196, May 1985. ISSN 0163-1829. doi: 10.1103/PhysRevB.31.6184. URL http://link.aps.org/doi/10.1103/PhysRevB.31.6184. 33

[85] D. W. Brenner. The Art and Science of an Analytic Potential. *Physica Status Solidi (B)*, 217(1):23–40, January 2000. ISSN 03701972. doi: 10.1002/(SICI)1521-3951(200001)217:1<23::AID-PSSB23>3.3.CO;2-E. URL http://doi.wiley.com/10.1002/%28SICI%291521-3951%28200001%29217%3A1%3C23%3A%3AAID-PSSB23%3E3.3.CO%3B2-E. 33, 34

[86] Donald Brenner. Empirical potential for hydrocarbons for use in simulating the chemical vapor deposition of diamond films, November 1990. ISSN 0163-1829. URL http://link.aps.org/doi/10.1103/PhysRevB.42.9458. 34

[87] D. Brenner, J. Harrison, C. White, and R. Colton. Molecular dynamics simulations of the nanometer-scale mechanical properties of compressed Buckminsterfullerene. *Thin Solid Films*, 206(1-2):220–223, December 1991. ISSN 00406090. doi: 10.1016/0040-6090(91)90425-W. URL http://dx.doi.org/10.1016/0040-6090(91)90425-W. 34

[88] Donald W. Brenner. Erratum: Empirical potential for hydrocarbons for use in simulating the chemical vapor deposition of diamond films. *Phys. Rev. B*, 46(3):1948, Jul 1992. doi: 10.1103/

PhysRevB.46.1948.2. URL http://link.aps.org/doi/10.1103/PhysRevB.46.1948.2. 34

[89] H. Rafii-Tabar and G. A. Mansoori. Interatomic potential models for nanostructures. *Encylopedia of Nanoscience and Nanotechnology*, 4:231–248, 2004. URL http://tigger.uic.edu/labs/trl/1.OnlineMaterials/nano.publications/03.Nanostructures.InterMoleForce.pdf. 34

[90] Donald W. Brenner, Olga A. Shenderova, Judith A. Harrison, Steven J. Stuart, Boris Ni, and Susan B. Sinnott. A second-generation reactive empirical bond order (REBO) potential energy expression for hydrocarbons. *Journal of Physics: Condensed Matter*, 14(4):783–802, February 2002. ISSN 0953-8984. doi: 10.1088/0953-8984/14/4/312. URL http://stacks.iop.org/0953-8984/14/i=4/a=312. 34

[91] Donald Brenner. Relationship between the embedded-atom method and Tersoff potentials. *Physical Review Letters*, 63 (9):1022–1022, August 1989. ISSN 0031-9007. doi: 10.1103/PhysRevLett.63.1022. URL http://link.aps.org/doi/10.1103/PhysRevLett.63.1022. 34

[92] Steven J. Stuart, Alan B. Tutein, and Judith A. Harrison. A reactive potential for hydrocarbons with intermolecular interactions. *The Journal of Chemical Physics*, 112(14):6472, 2000. ISSN 00219606. doi: 10.1063/1.481208. URL http://link.aip.org/link/JCPSA6/v112/i14/p6472/s1&Agg=doi. 35

[93] Stephen L. Mayo, Barry D. Olafson, and William A. Goddard. DREIDING: a generic force field for molecular simulations. *The Journal of Physical Chemistry*, 94(26):8897–8909, December 1990. ISSN 0022-3654. doi: 10.1021/j100389a010. URL http://dx.doi.org/10.1021/j100389a010. 35, 102

[94] Adri C. T. van Duin, Siddharth Dasgupta, Francois Lorant, and William A. Goddard. ReaxFF: A Reactive Force Field for Hydrocarbons. *The Journal of Physical Chemistry A*, 105(41):9396–9409, October 2001. ISSN 1089-5639. doi: 10.1021/jp004368u. URL http://pubs.acs.org/doi/abs/10.1021/jp004368u. 35

[95] D. J. O'Connor and J. P. Biersack. Comparison of theoretical and empirical interatomic potentials. *Nuclear Instruments and Methods in Physics Research Section B: Beam Interactions with Materials*

and Atoms, 15(1-6):14–19, April 1986. ISSN 0168583X. doi: 10.1016/0168-583X(86)90243-0. URL http://dx.doi.org/10.1016/0168-583X(86)90243-0. 36, 102

[96] D. J. O'Connor and R. J. MacDonald. A correction factor to the interatomic potential screening function for use in computer simulations. *Radiation Effects*, 34(4):247–250, 1977. doi: 10.1080/00337577708233154. URL http://tandfprod.literatumonline.com/doi/abs/10.1080/00337577708233154. 36

[97] Barbara J. Garrison. Notes to SPUT2006 / SPUT2000 / Sput93. *Cell*, (February 2000):1–68, 2008. 39

[98] M. C. Payne, T. A. Arias, and J. D. Joannopoulos. Iterative minimization techniques for ab initio total-energy calculations: molecular dynamics and conjugate gradients. *Reviews of Modern Physics*, 64(4):1045–1097, October 1992. ISSN 0034-6861. doi: 10.1103/RevModPhys.64.1045. URL http://link.aps.org/doi/10.1103/RevModPhys.64.1045. 39

[99] Dominik Marx and J. Hutter. Ab initio molecular dynamics: theory and implementation. *Modern methods and algorithms of quantum chemistry*, 3:301–449, 2000. URL http://134.94.100.198/nic-series/Volume3/marx.pdf. 39

[100] R. Car and M. Parrinello. Unified approach for molecular dynamics and density-functional theory. *Physical review letters*, 55 (22):2471–2474, 1985. URL http://link.aps.org/doi/10.1103/PhysRevLett.55.2471. 39

[101] I. Wojciechowski, A. Delcorte, and X. Gonze. Mechanism of metal cationization in organic SIMS. *Chemical physics letters*, 203-204:102–105, January 2001. ISSN 01694332. doi: 10.1016/S0169-4332(02)00708-0. URL http://linkinghub.elsevier.com/retrieve/pii/S0169433202007080http://www.sciencedirect.com/science/article/pii/S0009261401009319. 39

[102] J. Pruneda, D. Sánchez-Portal, A. Arnau, J. Juaristi, and Emilio Artacho. Electronic Stopping Power in LiF from First Principles. *Physical Review Letters*, 99(23):1–4, December 2007. ISSN 0031-9007. doi: 10.1103/PhysRevLett.99.235501. URL http://link.aps.org/doi/10.1103/PhysRevLett.99.235501. 39

[103] J.M. Pruneda, D. Sánchez-Portal, A. Arnau, J.I. Juaristi, and E. Artacho. Heating electrons with ion irradiation: A first-principles approach. *Nuclear Instruments and Methods in Physics Research Section B: Beam Interactions with Materials and Atoms*, 267(4):590–593, February 2009. ISSN 0168583X. doi: 10.1016/j.nimb.2008.11.012. URL http://linkinghub.elsevier.com/retrieve/pii/S0168583X08012779. 39

[104] M. Keim, A. Achenbach, H.J. Lüdde, and T. Kirchner. Time-dependent density functional theory calculations for collisions of bare ions with helium. *Nuclear Instruments and Methods in Physics Research Section B: Beam Interactions with Materials and Atoms*, 233(1-4):240–243, May 2005. ISSN 0168583X. doi: 10.1016/j.nimb.2005.03.114. URL http://linkinghub.elsevier.com/retrieve/pii/S0168583X05003381. 39

[105] Guillermo Avendaño Franco, Bernard Piraux, Myrta Grüning, and Xavier Gonze. Time-Dependent Density Functional Theory study of charge transfer in collisions. *To be submitted*. 39

[106] B. Weidtmann, A. Duvenbeck, S. Hanke, and A. Wucher. Crystallographic effects in the kinetic excitation of metal surfaces: A computational study. *Nuclear Instruments and Methods in Physics Research Section B: Beam Interactions with Materials and Atoms*, 267(4):598–600, February 2009. ISSN 0168583X. doi: 10.1016/j.nimb.2008.11.047. URL http://linkinghub.elsevier.com/retrieve/pii/S0168583X08013219. 39

[107] M. Lindenblatt, E. Pehlke, A. Duvenbeck, B. Rethfeld, and A. Wucher. Kinetic excitation of solids: The concept of electronic friction. *Nuclear Instruments and Methods in Physics Research Section B: Beam Interactions with Materials and Atoms*, 246(2):333–339, May 2006. ISSN 0168583X. doi: 10.1016/j.nimb.2006.01.006. URL http://linkinghub.elsevier.com/retrieve/pii/S0168583X06000279. 39

[108] M. Lindenblatt, E. Pehlke, A. Duvenbeck, B. Rethfeld, and A. Wucher. Kinetic excitation of solids: The concept of electronic friction. *Nuclear Instruments and Methods in Physics Research Section B: Beam Interactions with Materials and Atoms*, 246(2):333–339, May 2006. ISSN 0168583X. doi: 10.1016/j.nimb.2006.01.006. URL http://linkinghub.elsevier.com/retrieve/pii/S0168583X06000279. 39

[109] T. Peters, C. Haake, D. Diesing, D. A. Kovacs, A. Golczewski, G. Kowarik, F. Aumayr, A. Wucher, and M. Schleberger. Hot electrons induced by slow multiply charged ions. *New Journal of Physics*, 10(7):073019, July 2008. ISSN 1367-2630. doi: 10.1088/1367-2630/10/7/073019. URL http://stacks.iop.org/1367-2630/10/i=7/a=073019?key=crossref.98832d99f8b6abf9972d154d571bf688. 39

[110] A. Duvenbeck, F. Sroubek, Z. Sroubek, and A. Wucher. Computer simulation of low-energy electronic excitations in atomic collision cascades. *Nuclear Instruments and Methods in Physics Research Section B: Beam Interactions with Materials and Atoms*, 225(4): 464–477, October 2004. ISSN 0168583X. doi: 10.1016/j.nimb.2004.05.021. URL http://linkinghub.elsevier.com/retrieve/pii/S0168583X04007918. 40

[111] A. Duvenbeck and A. Wucher. Low-energy electronic excitation in atomic collision cascades: A nonlinear transport model. *Physical Review B*, 72(16):1–9, October 2005. ISSN 1098-0121. doi: 10.1103/PhysRevB.72.165408. URL http://link.aps.org/doi/10.1103/PhysRevB.72.165408. 40

[112] A. Duvenbeck, O. Weingart, V. Buss, and A. Wucher. On the role of electronic friction and electron promotion in kinetic excitation of solids. *Nuclear Instruments and Methods in Physics Research Section B: Beam Interactions with Materials and Atoms*, 255(1): 281–285, February 2007. ISSN 0168583X. doi: 10.1016/j.nimb.2006.11.030. URL http://linkinghub.elsevier.com/retrieve/pii/S0168583X06011256. 40

[113] Andreas Duvenbeck, Boris Weidtmann, Oliver Weingart, and Andreas Wucher. Modeling hot-electron generation induced by electron promotion in atomic collision cascades in metals. *Physical Review B*, 77(24):35–37, June 2008. ISSN 1098-0121. doi: 10.1103/PhysRevB.77.245444. URL http://link.aps.org/doi/10.1103/PhysRevB.77.245444. 40

[114] J. Lindhard and M. Scharff. Energy Dissipation by Ions in the kev Region. *Physical Review*, 124(1):128–130, October 1961. ISSN 0031-899X. doi: 10.1103/PhysRev.124.128. URL http://prola.aps.org/abstract/PR/v124/i1/p128_1. 40

[115] Bradley D. Fahlman. *Materials Chemistry*. Springer,

2008. ISBN 1402061196. URL http://www.amazon.com/Materials-Chemistry-Bradley-D-Fahlman/dp/1402061196. 41

[116] P. Bertrand, H. Bu, and J. W. Rabalais. Orientation of single crystalline paraffin thin films from time-of-flight direct recoil spectrometry. *The Journal of Physical Chemistry*, 97(51):13788–13791, December 1993. ISSN 0022-3654. doi: 10.1021/j100153a057. URL http://dx.doi.org/10.1021/j100153a057. 41, 42, 51, 85

[117] Stepan Kashtanov, Guorong V. Zhuang, Andreas Augustsson, Joseph Nordgren, Y. Luo, Philip N. Ross, and Jinghua Guo. Structural conformation in a poly(ethylene oxide) film determined by X-ray emission spectroscopy. *The journal of physical chemistry. B*, 111(40):11658–61, October 2007. ISSN 1520-6106. doi: 10.1021/jp072141u. URL http://dx.doi.org/10.1021/jp072141u. 41

[118] Hiroyuki Tadokoro. *Structure of Crystalline Polymers*. Krieger Pub Co, 1990. ISBN 0894643495. URL http://www.amazon.com/Structure-Crystalline-Polymers-Hiroyuki-Tadokoro/dp/0894643495. 42

[119] J. Bruno, N. Allan, T. Barron, and A. Turner. Thermal expansion of polymers: Mechanisms in orthorhombic polyethylene. *Physical Review B*, 58(13):8416–8427, October 1998. ISSN 0163-1829. doi: 10.1103/PhysRevB.58.8416. URL http://link.aps.org/doi/10.1103/PhysRevB.58.8416. 43, 51

[120] Markus Hütter, Pieter J. in 't Veld, and Gregory C. Rutledge. Polyethylene {201} crystal surface: interface stresses and thermodynamics. *Polymer*, 47(15):5494–5504, July 2006. ISSN 00323861. doi: 10.1016/j.polymer.2005.05.160. URL http://linkinghub.elsevier.com/retrieve/pii/S0032386106004940. 45

[121] Joseph Hautman and Michael L. Klein. Simulation of a monolayer of alkyl thiol chains. *The Journal of Chemical Physics*, 91(8):4994, 1989. ISSN 00219606. doi: 10.1063/1.457621. URL http://link.aip.org/link/doi/10.1063/1.457621/html. 45

[122] E. Smiley, Z. Postawa, I. Wojciechowski, N. Winograd, and B. Garrison. Coarse-grained molecular dynamics studies of cluster-bombarded benzene crystals. *Applied Surface Science*, 252(19):6436–6439, July 2006. ISSN 01694332. doi: 10.1016/j.apsusc.2006.02.095. URL http://linkinghub.elsevier.com/retrieve/pii/S016943320600362X. 46, 47, 134

[123] Rubin H. Landau, Manuel J. Páez, and Cristian C. Bordeianu. *Computational physics: problem solving with computers*, pages 301–302. John Wiley & Sons, Inc., New York, NY, USA, 2007. 49

[124] F. Kollmer. Cluster primary ion bombardment of organic materials. *Applied Surface Science*, 231-232:153–158, June 2004. ISSN 01694332. doi: 10.1016/j.apsusc.2004.03.101. URL http://linkinghub.elsevier.com/retrieve/pii/S0169433204003393. 55

[125] Christopher Szakal, Joseph Kozole, Michael Russo, Barbara Garrison, and Nicholas Winograd. Surface Sensitivity in Cluster-Ion-Induced Sputtering. *Physical Review Letters*, 96(21):3–6, June 2006. ISSN 0031-9007. doi: 10.1103/PhysRevLett.96.216104. URL http://link.aps.org/doi/10.1103/PhysRevLett.96.216104. 55, 56

[126] John C. Vickerman and David Briggs. *ToF-SIMS : Surface Analysis by Mass Spectrometry*, page 163. IM Publications LLP, 2001. ISBN 1901019039. URL http://www.amazon.co.uk/ToF-SIMS-Surface-Analysis-Mass-Spectrometry/dp/1901019039. 56, 66

[127] Y. Travaly and P. Bertrand. Static SIMS investigation of metal/polymer interfaces. *Surface and Interface Analysis*, 23(5):328–334, May 1995. ISSN 0142-2421. doi: 10.1002/sia.740230509. URL http://doi.wiley.com/10.1002/sia.740230509. 56

[128] A. Delcorte, C. Poleunis, and P. Bertrand. Stretching the limits of static SIMS with C_{60}^{+}. *Applied Surface Science*, 252(19):6494–6497, July 2006. ISSN 01694332. doi: 10.1016/j.apsusc.2006.02.259. URL http://linkinghub.elsevier.com/retrieve/pii/S016943320600331X. 58, 60

[129] David Touboul, Fréderic Halgand, Alain Brunelle, Reinhard Kersting, Elke Tallarek, Birgit Hagenhoff, and Olivier Laprévote. Tissue molecular ion imaging by gold cluster ion bombardment. *Analytical chemistry*, 76(6):1550–9, March 2004. ISSN 0003-2700. doi: 10.1021/ac035243z. URL http://www.ncbi.nlm.nih.gov/pubmed/15018551. 60

[130] K. Boussofianebaudin, G. Bolbach, A Brunelle, S. Dellanegra, P. Hakansson, and Y. Lebeyec. Secondary ion emission under

cluster impact at low energies (5-60 keV); influence of the number of atoms in the projectile. *Nuclear Instruments and Methods in Physics Research Section B: Beam Interactions with Materials and Atoms*, 88(1-2):160–163, April 1994. ISSN 0168583X. doi: 10.1016/0168-583X(94)96097-6. URL http://linkinghub.elsevier.com/retrieve/pii/0168583X94960976. 60

[131] Michael F. Russo and Barbara J. Garrison. Mesoscale energy deposition footprint model for kiloelectronvolt cluster bombardment of solids. *Analytical chemistry*, 78(20):7206–10, October 2006. ISSN 0003-2700. doi: 10.1021/ac061180j. URL http://www.ncbi.nlm.nih.gov/pubmed/17037922. 60, 83

[132] M Russo Jr., I. Wojciechowski, and B. Garrison. Sputtering of amorphous ice induced by C_{60} and Au_3 clusters. *Applied Surface Science*, 252(19):6423–6425, July 2006. ISSN 01694332. doi: 10.1016/j.apsusc.2006.02.243. URL http://linkinghub.elsevier.com/retrieve/pii/S0169433206003242. 60

[133] Michael F. Russo, Christopher Szakal, Joseph Kozole, Nicholas Winograd, and Barbara J. Garrison. Sputtering yields for C_{60} and Au3 bombardment of water ice as a function of incident kinetic energy. *Analytical chemistry*, 79(12):4493–8, June 2007. ISSN 0003-2700. doi: 10.1021/ac070105l. URL http://www.pubmedcentral.nih.gov/articlerender.fcgi?artid=2553706&tool=pmcentrez&rendertype=abstract. 60

[134] K. Ryan, M. Russojr, E. Smiley, Z. Postawa, and B. Garrison. Friction model to describe cluster bombardment. *Applied Surface Science*, 255(4):893–896, December 2008. ISSN 01694332. doi: 10.1016/j.apsusc.2008.05.113. URL http://linkinghub.elsevier.com/retrieve/pii/S0169433208011410. 60

[135] John C. Vickerman and David Briggs. *ToF-SIMS : Surface Analysis by Mass Spectrometry*, page 168. IM Publications LLP, 2001. ISBN 1901019039. URL http://www.amazon.co.uk/ToF-SIMS-Surface-Analysis-Mass-Spectrometry/dp/1901019039. 66

[136] Emilien Van Hoecke. Thèse de Master: Simulation numérique de l'effet de nanoparticules métalliques sur l'émission moléculaire lors de l'analyse de surfaces organiques par faisceaux d'ions . *UCL thesis, Université Catholique de Louvain - Ecole Polytechnique de Louvain*, 2011. 70, 71, 87, 88, 137, 141

[137] Karim Hamraoui and Arnaud Delcorte. Effects of Molecular Orientation and Size in Sputtering of Model Organic Crystals. *The Journal of Physical Chemistry C*, 114(12):5458–5467, April 2010. ISSN 1932-7447. doi: 10.1021/jp906004v. URL http://pubs.acs.org/doi/abs/10.1021/jp906004v. 78

[138] Nimer Wehbe, Andreas Heile, H. F. Arlinghaus, Patrick Bertrand, and Arnaud Delcorte. Effects of metal nanoparticles on the secondary ion yields of a model alkane molecule upon atomic and polyatomic projectiles in secondary ion mass spectrometry. *Analytical chemistry*, 80(16):6235–6244, 2008. doi: 10.1016/j.apsusc.2008.05.068.(44). URL http://pubs.acs.org/doi/abs/10.1021/ac800568y. 81

[139] A. Delcorte and B. J. Garrison. Sputtering Polymers with Buckminsterfullerene Projectiles: A Coarse-Grain Molecular Dynamics Study. *Journal of Physical Chemistry C*, 111(42):15312–15324, October 2007. ISSN 1932-7447. doi: 10.1021/jp074536j. URL http://pubs.acs.org/cgi-bin/doilookup/?10.1021/jp074536j. 83, 89, 97, 111

[140] Christian Anders, Herbert Urbassek, and Robert Johnson. Linearity and additivity in cluster-induced sputtering: A molecular-dynamics study of van der Waals bonded systems. *Physical Review B*, 70(15):1–6, October 2004. ISSN 1098-0121. doi: 10.1103/PhysRevB.70.155404. URL http://link.aps.org/doi/10.1103/PhysRevB.70.155404. 89

[141] S. Zimmermann and H. Urbassek. Sputtering of nanoparticles: Molecular dynamics study of Au impact on 20nm sized Au nanoparticles. *International Journal of Mass Spectrometry*, 272 (1):91–97, April 2008. ISSN 13873806. doi: 10.1016/j.ijms.2008.01.004. URL http://linkinghub.elsevier.com/retrieve/pii/S1387380608000195. 98, 111

[142] L. Rzeznik, B. Czerwinski, R. Paruch, B. J. Garrison, and Z. Postawa. Sputtering of thin benzene films by large noble gas clusters. *Nuclear Instruments and Methods in Physics Research Section B: Beam Interactions with Materials and Atoms*, 267(8-9):1436–1439, May 2009. ISSN 0168583X. doi: 10.1016/j.nimb.2009.01.057. URL http://linkinghub.elsevier.com/retrieve/pii/S0168583X09001050. 101

[143] Bartlomiej Czerwinski, Lukasz Rzeznik, Robert Paruch, Barbara J. Garrison, and Zbigniew Postawa. Effect of impact angle and projectile size on sputtering efficiency of solid benzene investigated by molecular dynamics simulations. *Nuclear Instruments and Methods in Physics Research Section B: Beam Interactions with Materials and Atoms*, 269(14):1578–1581, July 2011. ISSN 0168583X. doi: 10.1016/j.nimb.2010.12.026. URL http://linkinghub.elsevier.com/retrieve/pii/S0168583X10009596. 101

[144] L. Rzeznik, B. Czerwinski, B. J. Garrison, N. Winograd, and Z. Postawa. Microscopic Insight into the Sputtering of Thin Polystyrene Films on Ag{111} Induced by Large and Slow Ar Clusters. *Journal of Physical Chemistry C*, 112(2):521–531, January 2008. ISSN 1932-7447. doi: 10.1021/jp076667q. URL http://pubs.acs.org/cgi-bin/doilookup/?10.1021/jp076667q. 101

[145] Z. Postawa, L. Rzeznik, R. Paruch, M. F. Russo, N. Winograd, and B. J. Garrison. Depth profiling by cluster projectiles as seen by computer simulations. *Surface and Interface Analysis*, 43(1-2):12–15, January 2011. ISSN 01422421. doi: 10.1002/sia.3417. URL http://doi.wiley.com/10.1002/sia.3417. 101

[146] Lukasz Rzeznik, Robert Paruch, Barbara J. Garrison, and Zbigniew Postawa. Erosion of Ag surface by continuous irradiation with slow, large Ar clusters. *Nuclear Instruments and Methods in Physics Research Section B: Beam Interactions with Materials and Atoms*, 269(14):1586–1590, July 2011. ISSN 0168583X. doi: 10.1016/j.nimb.2010.11.098. URL http://linkinghub.elsevier.com/retrieve/pii/S0168583X10009390. 101

[147] T. Aoki and J. Matsuo. Molecular dynamics simulations of surface modification and damage formation by gas cluster ion impacts. *Nuclear Instruments and Methods in Physics Research Section B: Beam Interactions with Materials and Atoms*, 242(1-2):517–519, January 2006. ISSN 0168583X. doi: 10.1016/j.nimb.2005.09.011. URL http://linkinghub.elsevier.com/retrieve/pii/S0168583X0501760X. 101

[148] Y. Y. Cheng and C. C. Lee. Molecular dynamics simulations of argon cluster impacts on a nickel film surface. *Nuclear Instruments and Methods in Physics Research Section B: Beam Interactions with Materials and Atoms*, 267(8-9):1428–1431, May 2009. ISSN 0168583X. doi: 10.1016/j.nimb.2009.

01.056. URL http://linkinghub.elsevier.com/retrieve/pii/S0168583X09001037. 101

[149] Juha Samela and Kai Nordlund. Classical molecular dynamics simulations of hypervelocity nanoparticle impacts on amorphous silica. *Physical Review B*, 81(5):1–5, February 2010. ISSN 1098-0121. doi: 10.1103/PhysRevB.81.054108. URL http://link.aps.org/doi/10.1103/PhysRevB.81.054108. 101

[150] J. Samela, K. Nordlund, J. Keinonen, V. N. Popok, and E. E.B. Campbell. Argon cluster impacts on layered silicon, silica, and graphite surfaces. *The European Physical Journal D*, 43(1-3): 181–184, May 2007. ISSN 1434-6060. doi: 10.1140/epjd/e2007-00104-y. URL http://www.springerlink.com/index/10.1140/epjd/e2007-00104-y. 101

[151] S. Oshima, I. Kashihara, K. Moritani, N. Inui, and K. Mochiji. Soft-sputtering of insulin films in argon-cluster secondary ion mass spectrometry. *Rapid Communications in Mass Spectrometry*, 25 (8):1070–1074, 2011. URL http://onlinelibrary.wiley.com/doi/10.1002/rcm.4959/full. 101, 107

[152] Kousuke Moritani, Gen Mukai, Michihiro Hashinokuchi, and Kozo Mochiji. Site-Specific Fragmentation of Polystyrene Molecule Using Size-Selected Ar Gas Cluster Ion Beam. *Applied Physics Express*, 2:046001, April 2009. ISSN 1882-0778. doi: 10.1143/APEX.2.046001. URL http://apex.ipap.jp/link?APEX/2/046001/. 102, 107

[153] Y. Yamamoto, K. Ichiki, S. Ninomiya, T. Seki, T. Aoki, and J. Matsuo. Evaluation of surface damage on organic materials irradiated with Ar cluster ion beam. In *AIP Conference Proceedings*, volume 1321, page 298, 2011. ISBN 9780735408760. URL http://link.aip.org/link/?APCPCS/1321/298/1. 102, 107

[154] Sadia Rabbani, Andrew M. Barber, John S. Fletcher, Nicholas P. Lockyer, and John C. Vickerman. TOF-SIMS with Argon Gas Cluster Ion Beams: A Comparison with C(60)(+). *Analytical chemistry*, 83(10):3793–800, May 2011. ISSN 1520-6882. doi: 10.1021/ac200288v. URL http://www.ncbi.nlm.nih.gov/pubmed/21462969. 102, 107

[155] A. Heile, D. Lipinsky, N. Wehbe, A. Delcorte, P. Bertrand, A. Felten, L. Houssiau, J. Pireaux, R. Demondt, and L. Vanvaeck. Metal-assisted SIMS and cluster ion bombardment for

ion yield enhancement. *Applied Surface Science*, 255(4):941–943, December 2008. ISSN 01694332. doi: 10.1016/j.apsusc.2008.05.007. URL http://linkinghub.elsevier.com/retrieve/pii/S016943320800994X. 102

[156] A. Heile, C. Muhmann, D. Lipinsky, and H. F. Arlinghaus. Investigations of secondary ion yield-enhancing methods in combination. *Surface and Interface Analysis*, 43(1-2):20–23, January 2011. ISSN 01422421. doi: 10.1002/sia.3556. URL http://doi.wiley.com/10.1002/sia.3556. 102

[157] A. Delcorte, B. J. Garrison, and K. Hamraoui. Dynamics of molecular impacts on soft materials: from fullerenes to organic nanodrops. *Analytical chemistry*, 81(16):6676–86, August 2009. ISSN 1520-6882. doi: 10.1021/ac900746x. URL http://www.ncbi.nlm.nih.gov/pubmed/20337378. 104, 107

[158] Christian Anders, Gerolf Ziegenhain, Steffen Zimmermann, and Herbert M. Urbassek. Cluster-induced crater formation. *Nuclear Instruments and Methods in Physics Research Section B: Beam Interactions with Materials and Atoms*, 267(18):3122–3125, September 2009. ISSN 0168583X. doi: 10.1016/j.nimb.2009.07.002. URL http://linkinghub.elsevier.com/retrieve/pii/S0168583X09008258. 104, 111

[159] Christian Anders and Herbert M. Urbassek. Cluster-induced sputtering of molecular targets. *Nuclear Instruments and Methods in Physics Research Section B: Beam Interactions with Materials and Atoms*, 267(18):3227–3231, September 2009. ISSN 0168583X. doi: 10.1016/j.nimb.2009.06.034. URL http://linkinghub.elsevier.com/retrieve/pii/S0168583X09007356. 104, 111

[160] Christian Anders and H. M. Urbassek. Effect of Molecular Dissociation Energy on the Sputtering of Molecular Targets. *The Journal of Physical Chemistry C*, 114(12):5499–5505, 2010. URL http://pubs.acs.org/doi/abs/10.1021/jp9061384. 112

List of publications

1. Restrepo, O.; Delcorte, A. "Molecular dynamics study of metal-organic samples bombarded by kiloelectronvolt projectiles". *Surf. Interface Anal.* 2011, 43, 70-73.

2. Restrepo, O.; Delcorte, A. "Au_{400} Sputtering of a Polymer with Adsorbed Metal Nanoparticles: A Molecular Dynamics Study". *J. Phys. Chem. C* 2011, 115, 12751-12759.

3. Restrepo, O.; Prabhakaran, A.; Delcorte, A. "Interaction of energetic clusters (Au_3, Au_{400} and C_{60}) with organic material and adsorbed gold nanoparticles". *Nucl. Instr. Meth. Phys. Res. B* 2011, 269, 1595-1599.

4. Restrepo, O.; Prabhakaran, A.; Hamraoui, K.; Wehbe, N.; Yunus, S.; Bertrand P.; Delcorte, A. "Mechanisms of metal-assisted secondary ion mass spectrometry: a mixed theoretical and experimental study". *Surf. Interface Anal.* 2010 42, 1030-1034.

5. Delcorte A.; Bertrand, P.; Garrison, B. J.; Hamraoui, K.; Mouhib, T.; Restrepo, O. A. Santos, C. N.; Yunus, S. "Probing soft materials with energetic ions and molecules: from microscopic models to the real world" *Surf. Interface Anal.* 2010, 42, 1380-1386.

6. Delcorte, A.; Restrepo O. A.; Czerwinski, B.; Garrison B. J. "Surface sputtering with nanoclusters: The relevant parameters." *Surf. Interface Anal.* (Accepted)